Summer trainee project 2018, Department of Applied Physics

Research group:	Quantum Computing and Devices (QCD)
Contact person:	Dr. Mikko Möttönen (mikko.mottonen@aalto.fi)
Field of research:	Nanoelectronics and Quantum Computing
Project title:	Superconducting quantum computers: control of dissipation
Project instructor:	Dr. Jan Goetz, M.Sc. Matti Partanen, Dr. Vasilii Sevriuk, Dr. Jani Tuorila, Dr. Matti Silveri
Site of research:	Aalto University, QCD group, Otaniemi
Website	Click here!
Level of student:	applications from all students are welcome (also for people applying for a Mater's or PhD thesis project)

Introduction

Quantum computer is an emerging computational device that can potentially solve some problems of practical interest that are impossible for the classical computer due to the required computational resources. Quantum bits, qubits, are the key ingredient of the quantum computer. Qubits can be employed to store and process quantum information, and they can be measured to extract classical information out of the quantum world.

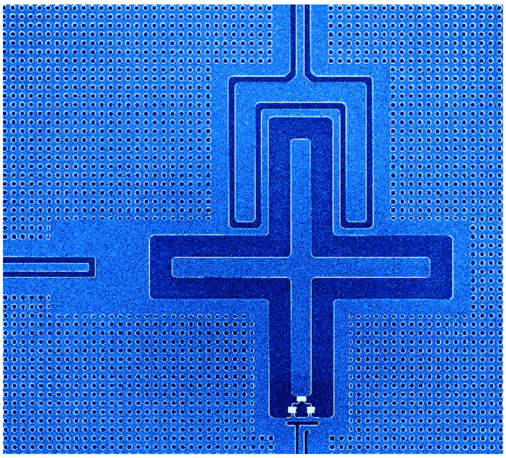

Figure 1. Scanning electron microscope image of a superconducting qubit (the cross-shaped bright region in the middle) fabricated by the QCD group. Figure credit: Jan Goetz/QCD.

One of the greatest developments of quantum technologies in the recent years has been the rise of circuit quantum electrodynamics (cQED). Here, superconducting qubits are coupled to microwave cavities and waveguides working at microwave frequencies. This allows not only to reproduce quantum optics experiments carried out with optical photons but also for a spectrum new physics and applications. For the quantum computer, one of the outstanding problems is the precise and fast initialization of the qubit register. Some of our ideas is to employ tunable dissipative environments to carry out the initialization process. These environments could be then decoupled from the qubits to allow for their coherent operation. The attached two recent papers provide two different approaches to implement tunable environments: using a tunnel junction controlled by a voltage source (first attachment) or a superconducting quantum interference device (second attachment).

Project goals

Your aim in this project is to employ artificial quantum-mechanical environments and their control protocols for cooling quantum microwave circuits such as resonators and superconducting quantum bits.

Research site

Your site of research will be the premises of Quantum Computing and Devices, the so-called QCD Labs, on the Otaniemi campus of Aalto University. There are both theorists and experimentalists working in the group. See the group website (http://physics.aalto.fi/en/groups/qcd/) for more information.

Instructors

Your instructors will be Dr. Jan Goetz (experiments), M.Sc. Matti Partanen (experiments), Dr. Jani Tuorila (theory), and/or Dr. Matti Silveri (theory).

Working methods

The main focus of the project can be adjusted according to your level and interests.

The work may be adjusted to either more theoretical or more experimental direction. Theoretical work involves modeling of microwaves in superconducting waveguides and analytical calculations. In experimental work, you design and implement measurements, and analyze the data.

Thesis possibilities

Depending on your level, this project can be adjusted for a BSc thesis, special assignment, MSc thesis, or a PhD thesis project. Some knowledge of quantum mechanics and an excellent study record is preferred.

nature COMMUNICATIONS

ARTICLE

Received 4 Oct 2016 | Accepted 8 Mar 2017 | Published 8 May 2017

DOI: 10.1038/ncomms15189

OPEN

Quantum-circuit refrigerator

Kuan Yen Tan[1], Matti Partanen[1], Russell E. Lake[1,†], Joonas Govenius[1,†], Shumpei Masuda[1] & Mikko Möttönen[1]

Quantum technology promises revolutionizing applications in information processing, communications, sensing and modelling. However, efficient on-demand cooling of the functional quantum degrees of freedom remains challenging in many solid-state implementations, such as superconducting circuits. Here we demonstrate direct cooling of a superconducting resonator mode using voltage-controllable electron tunnelling in a nanoscale refrigerator. This result is revealed by a decreased electron temperature at a resonator-coupled probe resistor, even for an elevated electron temperature at the refrigerator. Our conclusions are verified by control experiments and by a good quantitative agreement between theory and experimental observations at various operation voltages and bath temperatures. In the future, we aim to remove spurious dissipation introduced by our refrigerator and to decrease the operational temperature. Such an ideal quantum-circuit refrigerator has potential applications in the initialization of quantum electric devices. In the superconducting quantum computer, for example, fast and accurate reset of the quantum memory is needed.

---

[1] QCD Labs, COMP Centre of Excellence, Department of Applied Physics, Aalto University, PO Box 13500, FI-00076 Aalto, Finland. † Present addresses: National Institute of Standards and Technology, Boulder, Colorado 80305, USA (R.E.L); Department of Physics, Stockholm University, AlbaNova University Center, SE-10691 Stockholm, Sweden (J.G). Correspondence and requests for materials should be addressed to K.Y.T. (email: kuan.tan@aalto.fi) or to M.M. (email: mikko.mottonen@aalto.fi).

Engineered quantum systems show great potential in providing a spectrum of devices superior to the present state of the art in information technological applications. Since quantum technological devices operate at the level of single energy quanta, they exhibit very low tolerance against external perturbations. Consequently, they need to be extremely well isolated from all sources of dissipation during their quantum coherent operation. These properties typically lead to an elevated steady-state temperature and long natural initialization times. Thus, finding a versatile active refrigerator for quantum devices is of great importance.

One of the greatest challenges of this century is to build a working large-scale quantum computer[1,2]. To date, a superconducting quantum computer[3] has reached the required gate and measurement accuracy thresholds for fault-tolerant quantum error correction[4,5] (see also ref. 6). This device builds on the decade-long development of circuit quantum electrodynamics[7–10], that is, the study of superconducting quantum bits, qubits, coupled to on-chip microwave resonators[11–13]. Although several methods have been demonstrated to initialize superconducting qubits[14–20] and resonators[21], they are typically suited only for a very specific type of a system and the achieved fidelities fall below the demanding requirements of efficient fault-tolerant quantum computing. Thus, circuit quantum electrodynamics provides an ideal context for the demonstration of a quantum refrigerator.

Electronic microcoolers based on normal metal–insulator–superconductor (NIS) tunnel junctions[22,23] offer opportunities[24] to cool electron systems well below the temperature of the phonon bath even at macroscopic sizes[25]. Due to the ideally exponential tunability of the NIS cooling and input powers using an applied bias voltage, these tunnel junctions are attractive candidates for quantum refrigerators. Although single-charge tunnelling has previously been demonstrated to emit and absorb energy quanta[26–29] even in applications such as the quantum cascade laser[30], and artificial-atom masers[31–33], it has not been experimentally utilized to directly cool engineered quantum circuits. Even the recently demonstrated autonomous Maxwell's demon has only been used to refrigerate dissipative electron systems[34].

In this work, we utilize photon-assisted electron tunnelling to cool a prototype superconducting quantum circuit, namely a transmission line resonator. The tunnelling takes place in NIS junctions. Since an electron tunnelling event changes the voltage across the resonator, it may simultaneously induce quantum transitions in the resonator modes[35]. Owing to the energy gap in the superconductor density of states, only the most energetic electrons can escape the normal metal in analogy with evaporative cooling. Thus, a tunnelling process where the electron absorbs a photon from the resonator, simultaneously increasing its energy, is favoured against photon emission. This is the key phenomenon leading to the refrigeration of the resonator. We refer to the NIS tunnel junctions and their coupling circuitry as the quantum-circuit refrigerator (QCR), which is a stand-alone component for cooling the operational quantum degrees of freedom in different types of under-damped quantum electric devices.

The photon-assisted cooling of the resonator mode is suggested by our qualitative observation that a distant probe resistor electrically coupled to the resonator cools down even if the temperature of the QCR, and of the other heat baths, is elevated. This claim is reinforced by the absence of cooling in a control sample, in which the coupling between the probe and the microwave resonator is suppressed. Furthermore, we obtain a good quantitative agreement between our theoretical model and the experimental results over a broad range of QCR operation voltages and bath temperatures, providing firm evidence of our conclusion that we directly refrigerate the resonator mode. We also verify that the resonator has a well-defined resonance.

Results

Experimental samples. Figure 1a–d shows the active sample where a QCR and a probe resistor are embedded near the opposite ends of a superconducting coplanar-waveguide resonator. The refrigerator involves a pair of NIS junctions biased using an operation voltage V_{QCR}. The probe resistor and the QCR are both equipped with an additional pair of current-biased NIS junctions. Using a calibration against the bath temperature (Supplementary Note 1 and Supplementary Fig. 1), the observed voltage excursions across these thermometer junctions provide us independent measures of the electron temperatures of the QCR, T_{QCR}, and of the probe resistor, T_{probe}. Figure 1e shows a control sample, which has additional superconducting wires in parallel with the QCR and probe resistors. The wires decouple the resistors from the electric currents associated with the resonator modes with no other significant effects. Thus, the difference between the behaviour of the active sample and that of the control sample can be attributed to microwave photons in the resonator.

The most important device parameters extracted from the experiments are listed in Table 1, including the length L and the resonance frequency f of the resonator. The probe resistance R and its distance x from the resonator edge determine the strength of the ohmic coupling between the probe electrons and the resonator mode. See Supplementary Note 2 for the relevance of these parameters in the thermal model used to describe the QCR.

Principle of quantum-circuit refrigeration. Let us consider sequential single-electron tunnelling through the NIS junctions of the QCR as described by Fermi's golden rule. Since the tunnelling process changes the electric charge in the resonator, the initial and final states of the resonator before and after an electron tunnelling event may be different[35]. As we discuss in Supplementary Note 3, the probability of this type of photon-assisted tunnelling is essentially proportional to an environmental parameter $\rho = \pi/(CR_{\mathrm{K}}\omega_0)$, where C is the effective capacitance of the resonator, R_{K} is the von Klitzing constant and $\omega_0 = 2\pi f_0$.

In addition to a finite environmental parameter, the tunnelling events need to be energetically possible. Owing to the energy cost of Δ for an unpaired electron to enter a superconductor, there is essentially no tunnelling at vanishing operation voltages and low-electron temperatures. Thus, when the QCR is in this off state $V_{\mathrm{QCR}} = 0$, the effect on the resonator is minimal.

Figure 2a shows an energy diagram for different tunnelling processes at the QCR with a finite operation voltage. Here electrons at various energy levels can overcome the energy cost Δ if they obtain an energy packet of $\hbar\omega_0$ from the resonator photon and of $eV_{\mathrm{QCR}}/2$ from the bias voltage source. However, elastic tunnelling and photon emission are still exponentially suppressed by the lack of high-energy thermal excitations. Thus, this bias voltage regime, $\Delta - \hbar\omega_0 \lesssim eV_{\mathrm{QCR}}/2 \lesssim \Delta$, is suitable for refrigerating the resonator.

In addition, the electron tunnelling current corresponding to photon-assisted tunnelling depends heavily on the state of the resonator. However, suppressed cooling power owing to low-resonator temperature does not imply that the QCR fails to carry its purpose—a ground-state system does not need to be initialized. Thus, instead of the cooling power, the important quantities describing the performance of the QCR are the relaxation and excitation rates that it introduces between the quantum levels of the resonator. See Supplementary Notes 5–8 for further discussion.

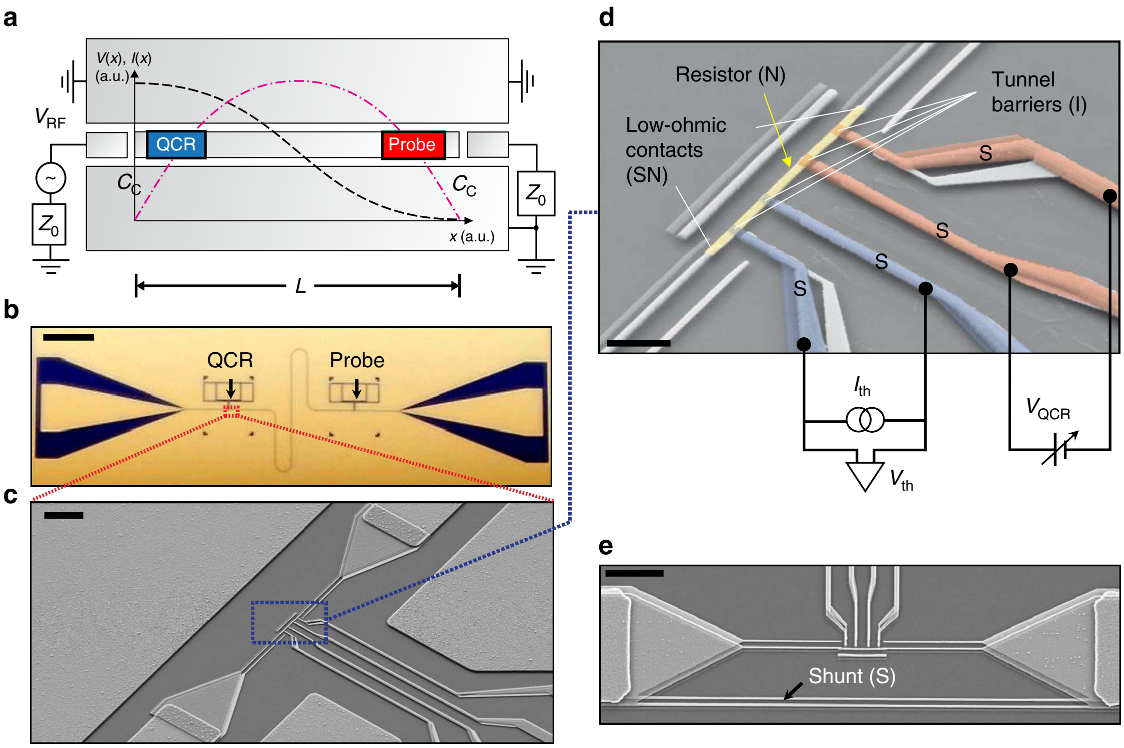

Figure 1 | Experimental sample and measurement scheme. (**a**) Schematic illustration of the active sample (not to scale) composed of a coplanar-waveguide resonator of length L with an embedded QCR and probe resistor. The voltage (V, black dashed line) and current (I, red dashed dotted line) profiles of the fundamental resonator mode are shown together with the possibility to apply an external microwave drive, V_{RF}, to the resonator through a coupling capacitor C_{c}. The characteristic impedance of the microwave line is $Z_0 = 50\,\Omega$. (**b**) Optical micrograph of an active sample corresponding to **a**. The QCR and the probe resistor are indicated by the arrows. The large triangle-like features near the left and right ends of the chip are bonding pads for the microwave drive. The thin meandering feature connecting the QCR and the probe is the resonator. (**c**) Scanning electron microscope (SEM) image in the vicinity of the QCR. The centre conductor of the resonator is galvanically connected to aluminium leads, which are again connected to the normal metal of the QCR (centre of figure). (**d**) Coloured SEM image of the QCR with normal-metal (N), insulator (I) and superconductor (S) materials indicated. The refrigerator is operated in voltage bias, V_{QCR}, while the electron temperature of the normal metal is obtained from the voltage V_{th} across a pair of NIS junctions biased with current I_{th}. (**e**) SEM image of the shunted control sample in the vicinity of the QCR. Scale bars, 1 mm (**b**), 5 μm (**c**), 1 μm (**d**) and 5 μm (**e**).

Table 1 | Key device parameters.

Parameter	Symbol	Value	Unit
Resonator length	L	6.833	mm
Fundamental resonance frequency	f_0	9.32	GHz
Resistance of QCR and probe resistors	R	46	Ω
Distance of the resistors from resonator edge	x	100	μm

These most important device parameters are extracted from the discussed experiments. The full list of parameters used in the thermal model can be found in Supplementary Table 1.

Using the parameters realized in our experiments, Fig. 2b and Supplementary Fig. 3 show theoretically obtained (Supplementary Note 3) rates for exciting the ground state of the fundamental resonator mode, $\Gamma^{\mathrm{T}}_{0\to1}$, and for the relaxation of the first excited state, $\Gamma^{\mathrm{T}}_{1\to0}$, as functions of the operation voltage. These rates are proportional to the environmental parameter and to the normal-state conductance of the tunnel junction, which are fixed in fabrication to obtain a desirable overall level for the rates. Importantly, the above-discussed energy constraints determine the behaviour of the rates as functions of the operation voltage.

We observe in Fig. 2b that both rates achieve their minima at low-operation voltages as expected for the off state of the QCR. Here the rates are roughly $10^4\,\mathrm{s}^{-1}$ and below which implies that they do not dominate the relaxation dynamics of a quantum device with a natural lifetime below 100 μs. Slightly below the gap voltage, we have $1/\Gamma^{\mathrm{T}}_{1\to0} < 10\,\mathrm{ns}$, which allows for quick initialization when desired. Here the excited-state population of the resonator solely corresponding to these rates is $\Gamma^{\mathrm{T}}_{0\to1}/\left(\Gamma^{\mathrm{T}}_{1\to0} + \Gamma^{\mathrm{T}}_{0\to1}\right) < 10^{-3}$. If demonstrated in a superconducting qubit, these numbers would represent a clear improvement in the present state-of-the-art initialization schemes[14–20]. Interestingly, Fig. 2b also shows that somewhat below the gap voltage, photon-assisted tunnelling tends to drive the resonator to much smaller excited-state populations than the QCR electron system.

As discussed below, the experimentally achieved photon number of the resonator also depends on other heat conduction channels. However, note that the experimental parameters used to obtain the results from Fig. 2b onwards are chosen to conveniently reveal the QCR operation and are not optimal for high-finesse or low-temperature cooling. Optimization of the parameters is discussed in Supplementary Note 4.

Observation of quantum-circuit refrigeration. Figure 3a shows the measured changes in the electron temperatures of the QCR and of the probe resistor as functions of the QCR operation voltage. Slightly below the gap voltage $2\Delta/e$, both electron temperatures are significantly decreased. Here the high-energy electrons at the QCR overcome the superconductor energy gap

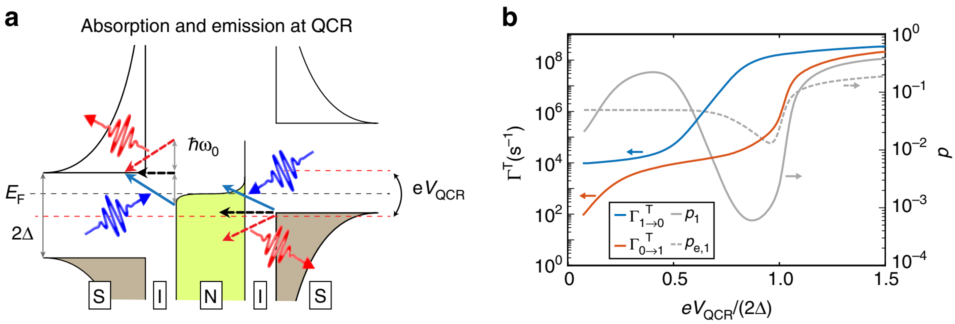

Figure 2 | Electron tunnelling events and the resulting resonator transition rates. (**a**) Schematic energy diagram illustrating sequential single-electron tunnelling events in the QCR: elastic tunnelling (black arrows), photon absorption from the resonator (blue arrows) and photon emission to the resonator (red arrows). The beginning of a straight arrow denotes the initial energy (vertical axis) and location (S or N) of the electron that tunnels, and the head of the arrow points to the final energy and location. The wavy arrows illustrate the photons absorbed (blue) and emitted (red) by the electrons. The coloured regions denote the occupied states and the white regions correspond to empty or absent states. The absence of states occurs at the insulators (I) and in the energy gap of size 2Δ at the superconductor. The dashed arrows indicate tunnelling processes which are forbidden owing to no occupancy at the initial energy level or no vacancy at the final level. Although tunnelling takes place at a multitude of different energy levels, we only show the most likely events of each kind which either initiate or terminate at the edge of the superconductor energy gap where the density of states (black solid line at S) ideally diverges. The dashed lines show the Fermi levels of the normal metal (black, E_F) and of the superconductors (red). The work done by the voltage source in the course of an electron tunnelling event through the whole structure, eV_{QCR}, is depicted as corresponding shifts of the Fermi levels. (**b**) Relaxation ($\Gamma^T_{1\to0}$, blue line) and excitation ($\Gamma^T_{0\to1}$, red line) rates of the fundamental mode of the resonator and the corresponding steady-state excitation probability $p_1 = \Gamma^T_{0\to1}/\left(\Gamma^T_{0\to1} + \Gamma^T_{1\to0}\right)$ (grey line) as functions of the QCR operation voltage, V_{QCR}. The rates are calculated from the $P(E)$ theory (Supplementary Note 3) using the experimentally realized parameter values for the active sample and the two-state approximation. Supplementary Fig. 3 shows corresponding results for optimized parameters. The grey dashed line shows the excited-state population assuming that the resonator temperature equals that of the normal-metal electrons of the QCR.

and tunnel out of the normal metal, thus evaporatively cooling it. Typically, the observed temperature drop at the probe resistor would be simply explained by conduction of heat from it to the QCR electrons. However, this explanation is excluded by our observation that at operation voltages slightly above the gap voltage, the electron temperature in the QCR is elevated but the probe resistor remains cooled.

To explain the cooling of the probe resistor in Fig. 3a, we show a schematic energy diagram for the different types of tunnelling processes in Fig. 3b. In contrast to Fig. 2a, the operation voltage is above $2\Delta/e$, and hence elastic tunnelling is energetically favourable. In fact, elastic tunnelling is dominating here since photon-assisted tunnelling is suppressed by the small environmental parameter $\rho = 4.7 \times 10^{-3}$. At this operation voltage, elastic tunnelling mostly removes electrons below the Fermi energy of the normal metal and adds electrons above it, leading to the heating of the QCR electrons. However, elastic tunnelling has no direct effect on the resonator mode, which is predominantly cooled owing to photon absorption by the tunnelling electrons. Note that the emission of photons from the tunnelling electrons is suppressed by the relatively low-thermal population of the high-energy excitations in the normal metal.

In the highlighted region of Fig. 3a, the refrigeration of the resonator by photon-assisted tunnelling is competing with the power flowing into the resonator from the increasing electron temperature at the QCR. Since the QCR is located very close to the edge of the resonator where the mode current vanishes (Fig. 1a), the QCR electron system is rather weakly coupled to the resonator mode through ohmic losses. Thus, the dramatic rise of the electron temperature in the QCR at voltage $V_{QCR} \approx 2\Delta/e$ does not induce major changes in the temperature of the resonator or of the probe resistor. In an optimized design, the QCR can be placed at the very end of the resonator rendering the ohmic coupling negligibly weak. See Supplementary Note 4, Supplementary Fig. 2 and Supplementary Table 2 for details of the optimized design.

Thermal model. To analyse quantitatively the observed temperature changes in Fig. 3a, we introduce a thermal model shown in Fig. 3c. We theoretically model the photon-assisted tunnelling using the so-called $P(E)$ theory[35] for NIS tunnel junctions[36]. The dominating energy flows into the conduction electrons of the probe resistor are obtained from their coupling to the substrate phonons and to the resonator. The coupling to the resonator arises from ohmic losses in the resistor due to the electric current associated with the resonator photons[37]. Similar weak ohmic losses take place at the QCR. In addition, we take into account a weak residual heating of the probe resistor due to the power dissipation at the QCR, a constant thermal conductance to an excess bath and a constant heating of the resonator attributed to photon leakage from the high-temperature stages of the cryostat. Further details of the thermal model including the employed parameter values are given in Supplementary Note 2.

Quantum-circuit refrigeration explained by thermal model. For a given operation voltage and measured electron temperature at the QCR, we solve the temperatures of the probe resistor and the resonator from the thermal model (Supplementary Note 2) such that the different power flows in Fig. 3c balance each other. The theoretical prediction for the probe temperature is in very good quantitative agreement with our experimental observations as demonstrated in Fig. 3a. Thus, we may estimate the resonator temperature using that obtained from the thermal model as shown in Fig. 3d together with the average photon number (see also Supplementary Fig. 4). We observe that the resonator mode can be efficiently cooled down using the QCR operation voltage.

Figure 3a also shows that a theoretical prediction lacking the contribution from photon-assisted tunnelling is in clear disagreement with the measurements. This is a strong indication that the cooling power of the QCR originates from the direct absorption of resonator photons in the course of electron tunnelling.

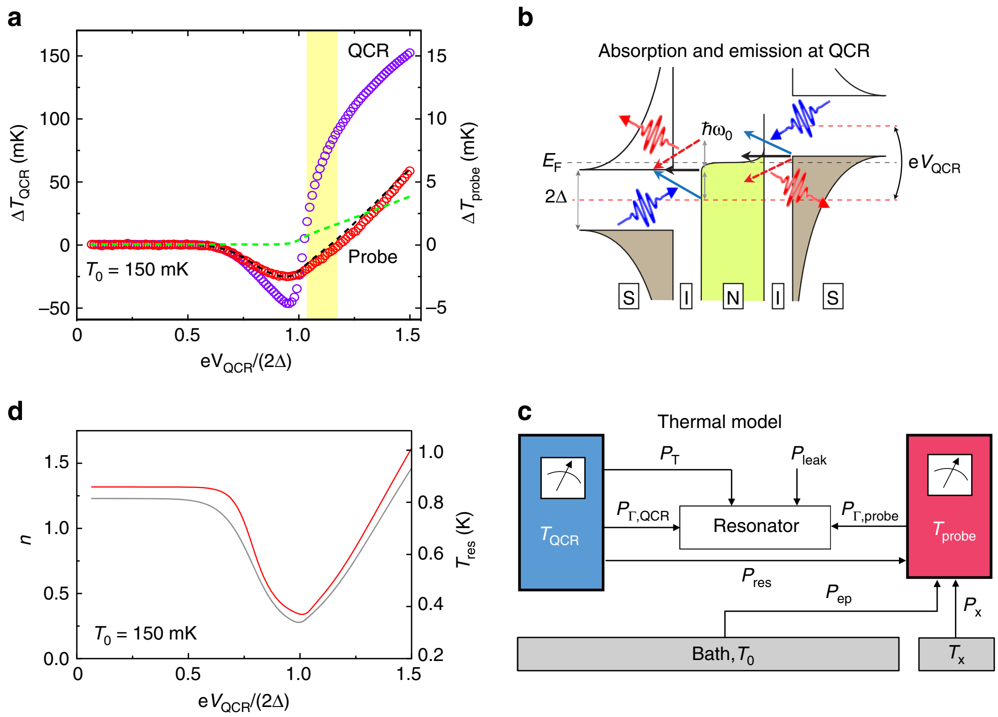

Figure 3 | Quantum-circuit refrigeration and thermal model. (**a**) Experimentally measured changes in the electron temperatures of the QCR, ΔT_{QCR} (purple circles) and of the probe resistor, ΔT_{probe} (red circles), as functions of the refrigerator operation voltage V_{QCR}. The dashed lines show the theoretical ΔT_{probe} with (black) and without (green) photon-assisted tunnelling. (**b**) Tunnelling diagram similar to that in Fig. 2a, but for a higher operation voltage corresponding to the region highlighted in yellow in **a**. Here only photon emission to the resonator is suppressed by the lack of thermal excitations. (**c**) Thermal model used for the experiment. Blue colour denotes the electron system of the QCR and red colour that of the probe resistor. Only the fundamental mode of the resonator is considered. The power P_T arises from photon-assisted tunnelling; $P_{\Gamma,QCR}$ and $P_{\Gamma,probe}$ correspond to ohmic losses; P_{ep} accounts for coupling between the probe electrons and the phonon bath at temperature T_0; P_{res} denotes the residual heating power of the probe due to V_{QCR}; P_{leak} accounts for leakage of photons to the resonator from high-temperature stages of the cryostat; and P_x denotes excess power due to a constant thermal conductance G_x to a reservoir at temperature T_x. Negative power implies the opposite direction of the energy flow with respect to the shown arrows. See Supplementary Note 2 for a detailed description of the model. (**d**) Resonator temperature (T_{res}, grey line) and average photon number (n, red line) solved from a thermal model corresponding to the measurements in **a**. See Supplementary Note 6 and Supplementary Fig. 4 for more information and for data at different bath temperatures.

Effect of bath temperature on the refrigeration. Figure 4a shows the temperature change of the probe resistor in a broad range of cryostat bath temperatures, T_0, and QCR operation voltages. A good quantitative agreement with the experimental data and the thermal model is obtained. For bath temperatures above 200 mK, the QCR operation voltage has a very weak effect on the probe resistor. This loss of probe sensitivity is explained by the quartic temperature dependence of the thermal conductance between the probe electrons and phonons given by supplementary equation (9) in Supplementary Note 1. The greater this thermal conductance is, the less sensitive the probe is to the changes of the resonator temperature.

Comparison with a control sample. Figure 4b shows results similar to those in Fig. 4a but obtained with the control sample, in which the ohmic losses at the QCR and at the probe due to the resonator modes are suppressed (Fig. 1e). Although residual heating is observed at high-operation voltages, there is no evidence of refrigeration at the probe. Thus, the cooling of the probe in the active sample must arise from the QCR acting on the resonator. This conclusion is also supported by Fig. 4c, where we show the maximum temperature drop of the probe for the two samples at various bath temperatures. Here the control sample exhibits no cooling and the theoretical prediction is in very good agreement with the experimental observations.

Microwave response of the resonator. To verify that the refrigerated resonator has a well-defined mode at the designed frequency, we introduce rf excitation to one of the input ports of the resonator as described in Fig. 1a. Although not necessary for the operation of the QCR, these ports are deliberately very weakly coupled to the mode, and hence there is essentially no transmission through the resonator. However, we study the resonance in Fig. 5 by measuring the electron temperatures of the QCR and of the probe resistor as functions of the frequency and power of the excitation. We observe a well-resolved resonance peak centred at $f_0 = \omega_0/(2\pi) = 9.32$ GHz in agreement with the design parameters (Supplementary Table 1). At the lowest probe powers, the electron temperature and the absorbed power are linearly dependent. Therefore, we can accurately extract the full-width at half-maximum, $\Delta f_0 = 70.8$ MHz, using a Lorentzian fit to the electron temperature. The obtained quality factor of the resonance, $Q = f_0/\Delta f_0 = 132$, indicates that the resonator supports a well-defined mode. Similar experiments on the control sample (Supplementary Fig. 5) yield a quality factor of 572 indicating that as expected, ohmic losses dominate in the active sample. We attribute the observed losses in the control sample to residual ohmic coupling owing to the finite impedance of the shunt.

Discussion

The main result of this work is the demonstrated principle that single-electron tunnelling between a normal metal and a

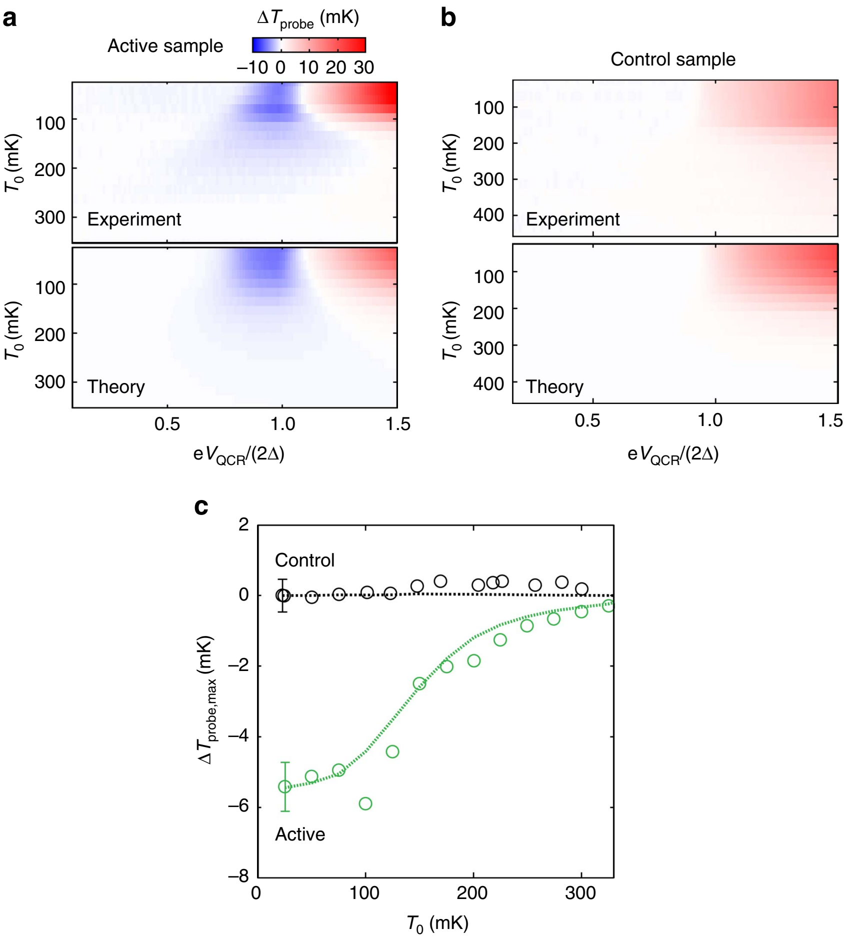

Figure 4 | Comparison between the active sample and the control sample. (**a**,**b**) Temperature change of the probe, $\Delta T_{\mathrm{probe}}$, as a function of the QCR operation voltage and the bath temperature for experimental and simulated data in the case of the active sample (**a**) and the control sample (**b**). (**c**) Temperature changes of the probe from the active sample (green circles, extracted from **a**) and from the control sample (black circles, extracted from **b**) as functions of the bath temperature at the operation voltage corresponding to the maximum cooling point of the probe and the QCR, respectively. Dashed lines show the corresponding data obtained from the thermal model. The error bars indicate the maximum s.d. for each data set.

superconductor can be used to refrigerate a microwave resonator on demand. In the future, we aim to optimize the set-up for minimal ohmic and other spurious losses (Supplementary Notes 4 and 9) and for low-resonator temperatures by improving the design, nanofabrication, shielding and filtering. An ideally working QCR can potentially refrigerate a multitude of high-quality quantum circuits with many conceivable applications such as precise qubit initialization for large-scale, gate-based quantum computing, quantum-state engineering driven by dissipation[38] and active enhancement of ground-state population in quantum annealing[39,40]. When inactive, such an ideal refrigerator does not degrade the quantum coherence as desired. To decrease the base temperature achieved with our device, multiple refrigerators may be cascaded with each other[41] or with distant ohmic reservoirs at very low temperatures[42].

In our experiments, the relatively low-quality factor of the resonator is a result of the chosen measurement scheme: rather strong dissipative coupling between the resonator photons and the probe resistor is needed to achieve conveniently measurable temperature changes at the probe resistor when the resonator is being refrigerated. In the future, different probe schemes may be employed where such limitation is absent. These include amplification and analysis of the resonator output signal[43,44] and measurement of the resonator occupation using a superconducting qubit[8,45]. Furthermore, the ohmic losses due to the QCR may be overcome by minimizing its resistance and by moving it to the end of the resonator where the current profile of the resonator mode ideally vanishes. Importantly, this does not reduce the cooling power of the QCR, which utilizes the voltage profile. As discussed in more detail in Supplementary Note 4, this type of straightforward improvements of the QCR are expected to allow for resonator quality factors[46] in the range of 10^6 when the QCR is inactive. Such a level of dissipation is low enough for the undisturbed operation of quantum devices in their known applications.

Methods

Sample fabrication. The samples are fabricated on four-inch prime-grade intrinsic silicon wafers with 300-nm thick thermally grown silicon dioxide. The resonator is defined with optical lithography and deposited using an electron beam evaporator, followed by a lift-off process. The evaporated metal film consists three layers from bottom to top: 200 nm of Al, 3 nm of Ti and 5 nm of Au. Here gold is used to prevent oxidation and titanium is introduced to avoid the diffusion of gold into the aluminium layer.

The nanostructures are defined by electron beam lithography. Here we employ a bilayer resist mask consisting of poly(methyl methacrylate) and poly[(methyl methacrylate)-co-(methacrylic acid)] to enable three-angle shadow evaporation. The trilayer nanostructures are deposited in an electron beam evaporator, with *in situ* oxidation in between the first layer (Al) and the second layer (Cu) to form the NIS tunnel junctions. The third layer (Al) forms a low-ohmic contact with the second layer, which functions as the normal metal in our low-temperature experiments. A lift-off process is performed to remove excess metal. See Table 1 for the resulting parameter values.

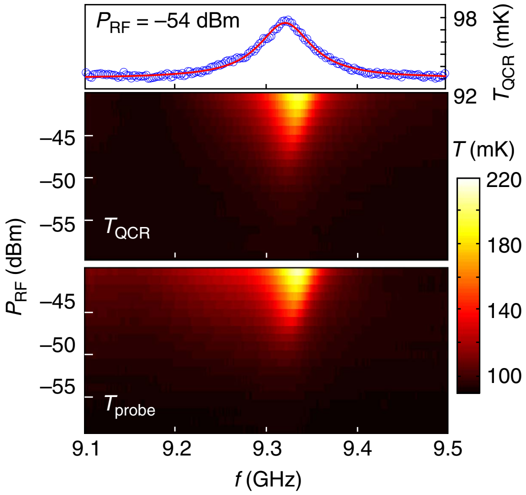

Figure 5 | Observation of the fundamental resonance. Experimentally observed electron temperatures of the QCR and of the probe resistor as functions of the frequency and power of the external microwave drive. The measurement scheme is illustrated in Fig. 1a. We also show a trace of the refrigerator temperature at −54-dBm room temperature power (markers) together with a Lorentzian fit (solid line). The indicated room temperature power levels decrease according to Supplementary Fig. 1c before reaching the sample.

Improvements to the fabrication process towards lowering the amount of electric losses in the resonator are discussed in Supplementary Note 4.

Measurements. For cryogenic electrical measurements, the sample holders are mounted to a cryogen-free dilution refrigerator with a base temperature of 10 mK. The silicon chip supporting the sample is attached with vacuum grease to the sample holder and wedge bonded to the electrical leads of the printed circuit board using aluminium wires. For each dc line, we employ an individual resistive Thermocoax cable that runs without interruption from the mixing chamber plate of the dilution refrigerator to room temperature.

The NIS thermometers are biased with floating battery-powered current sources and the voltage drops across these junctions are amplified with high-impedance battery-powered voltage preamplifiers before optoisolation and digitalization with an oscilloscope. In the experiments studying different QCR operation voltages, we sweep V_{QCR} at a rate of $\sim 20\,\mu\mathrm{V\,s}^{-1}$ using an output of an arbitrary function generator that is connected to the cryostat through an optoisolator. The sweep is repeated 10 times at each bath temperature.

In the rf measurements, the sinusoidal drive signal is generated by a variable-frequency microwave source and guided to the sample through low-loss coaxial cables, which are attenuated at different temperature stages of the cryostat as shown in Supplementary Fig. 1c.

See Supplementary Note 1 for the details of the NIS thermometry including calibration data.

Modelling. All numerical computations are carried out using regular desktop computers. See Supplementary Note 2 for a detailed description of the theoretical model used in this work.

Data availability. The data and codes that support the findings of this study are available from the corresponding authors on request.

References

1. Ladd, T. D. *et al.* Quantum computers. *Nature* **464,** 45–53 (2010).
2. Morton, J. J. L., McCamey, D. R., Eriksson, M. A. & Lyon, S. A. Embracing the quantum limit in silicon computing. *Nature* **479,** 345–353 (2011).
3. Devoret, M. H. & Schoelkopf, R. J. Superconducting circuits for quantum information: an outlook. *Science* **339,** 1169–1174 (2013).
4. Barends, R. *et al.* Superconducting quantum circuits at the surface code threshold for fault tolerance. *Nature* **508,** 500–503 (2014).
5. Kelly, J. *et al.* State preservation by repetitive error detection in a superconducting quantum circuit. *Nature* **519,** 66–69 (2015).
6. Veldhorst, M. *et al.* An addressable quantum dot qubit with fault-tolerant control-fidelity. *Nat. Nanotechnol.* **9,** 981–985 (2014).
7. Blais, A., Huang, R.-S., Wallraff, A., Girvin, S. M. & Schoelkopf, R. J. Cavity quantum electrodynamics for superconducting electrical circuits: an architecture for quantum computation. *Phys. Rev. A* **69,** 062320 (2004).
8. Wallraff, A. *et al.* Strong coupling of a single photon to a superconducting qubit using circuit quantum electrodynamics. *Nature* **431,** 162–167 (2004).
9. DiCarlo, L. *et al.* Demonstration of two-qubit algorithms with a superconducting quantum processor. *Nature* **460,** 240–244 (2009).
10. Clarke, J. & Wilhelm, F. K. Superconducting quantum bits. *Nature* **453,** 1031–1042 (2008).
11. Koch, J. *et al.* Charge-insensitive qubit design derived from the cooper pair box. *Phys. Rev. A* **76,** 042319 (2007).
12. Manucharyan, V. E., Koch, J., Glazman, L. I. & Devoret, M. H. Fluxonium: single cooper-pair circuit free of charge offsets. *Science* **326,** 113–116 (2009).
13. Nataf, P. & Ciuti, C. Protected quantum computation with multiple resonators in ultrastrong coupling circuit QED. *Phys. Rev. Lett.* **107,** 190402 (2011).
14. Valenzuela, S. O. *et al.* Microwave-induced cooling of a superconducting qubit. *Science* **314,** 1589–1592 (2006).
15. Reed, M. D. *et al.* Fast reset and suppressing spontaneous emission of a superconducting qubit. *Appl. Phys. Lett.* **96,** 203110 (2010).
16. Mariantoni, M. *et al.* Implementing the quantum von neumann architecture with superconducting circuits. *Science* **334,** 61–65 (2011).
17. Ristè, D., Bultink, C. C., Lehnert, K. W. & DiCarlo, L. Feedback control of a solid-state qubit using high-fidelity projective measurement. *Phys. Rev. Lett.* **109,** 240502 (2012).
18. Geerlings, K. *et al.* Demonstrating a driven reset protocol for a superconducting qubit. *Phys. Rev. Lett.* **110,** 120501 (2013).
19. Campagne-Ibarcq, P. *et al.* Persistent control of a superconducting qubit by stroboscopic measurement feedback. *Phys. Rev. X* **3,** 021008 (2013).
20. Bultink, C. C. *et al.* Active resonator reset in the nonlinear dispersive regime of circuit QED. *Phys. Rev. Appl.* **6,** 034008 (2016).
21. Schliesser, A., Riviere, R., Anetsberger, G., Arcizet, O. & Kippenberg, T. J. Resolved-sideband cooling of a micromechanical oscillator. *Nat. Phys.* **4,** 415–419 (2008).
22. Giazotto, F., Heikkilä, T. T., Luukanen, A., Savin, A. M. & Pekola, J. P. Opportunities for mesoscopics in thermometry and refrigeration: physics and applications. *Rev. Mod. Phys.* **78,** 217–274 (2006).
23. Courtois, H., Hekking, F., Nguyen, H. & Winkelmann, C. Electronic coolers based on superconducting tunnel junctions: fundamentals and applications. *J. Low Temp. Phys.* **175,** 799–812 (2014).
24. Giazotto, F. & Martínez-Pérez, M. J. The Josephson heat interferometer. *Nature* **492,** 401–405 (2012).
25. Lowell, P. J., Neil, G. C., Underwood, J. M. & Ullom, J. N. Macroscale refrigeration by nanoscale electron transport. *Appl. Phys. Lett.* **102,** 082601 (2013).
26. Hofheinz, M. *et al.* Bright side of the coulomb blockade. *Phys. Rev. Lett.* **106,** 217005 (2011).
27. Liu, Y.-Y., Petersson, K. D., Stehlik, J., Taylor, J. M. & Petta, J. R. Photon emission from a cavity-coupled double quantum dot. *Phys. Rev. Lett.* **113,** 036801 (2014).
28. Stockklauser, A. *et al.* Microwave emission from hybridized states in a semiconductor charge qubit. *Phys. Rev. Lett.* **115,** 046802 (2015).
29. Bruhat, L. E. *et al.* Cavity photons as a probe for charge relaxation resistance and photon emission in a quantum dot coupled to normal and superconducting continua. *Phys. Rev. X* **6,** 021014 (2016).
30. Faist, J. *et al.* Quantum cascade laser. *Science* **264,** 553–556 (1994).
31. Astafiev, O. *et al.* Single artificial-atom lasing. *Nature* **449,** 588–590 (2007).
32. Liu, Y.-Y. *et al.* Semiconductor double quantum dot micromaser. *Science* **347,** 285–287 (2015).
33. Mendes, U. C. & Mora, C. Electron-photon interaction in a quantum point contact coupled to a microwave resonator. *Phys. Rev. B* **93,** 235450 (2016).
34. Koski, J. V., Kutvonen, A., Khaymovich, I. M., Ala-Nissila, T. & Pekola, J. P. On-chip maxwell's demon as an information-powered refrigerator. *Phys. Rev. Lett.* **115,** 260602 (2015).
35. Ingold, G.-L. & Nazarov, Y. in *Single Charge Tunneling* vol 294 (eds Grabert, H. & Devoret, M.) 21–107 (Springer, 1992).
36. Pekola, J. P. *et al.* Environment-assisted tunnelling as an origin of the dynes density of states. *Phys. Rev. Lett.* **105,** 026803 (2010).
37. Jones, P. J., Huhtamäki, J. A. M., Tan, K. Y. & Möttönen, M. Single-photon heat conduction in electrical circuits. *Phys. Rev. B* **85,** 075413 (2012).
38. Verstraete, F., Wolf, M. M. & Ignacio Cirac, J. Quantum computation and quantum-state engineering driven by dissipation. *Nat. Phys.* **5,** 633–636 (2009).
39. Johnson, M. W. *et al.* Quantum annealing with manufactured spins. *Nature* **473,** 194–198 (2011).
40. Dickson, N. G. *et al.* Thermally assisted quantum annealing of a 16-qubit problem. *Nat. Commun.* **4,** 1903 (2013).

41. Camarasa-Gömez, M. *et al.* Superconducting cascade electron refrigerator. *Appl. Phys. Lett.* **104,** 192601 (2014).
42. Partanen, M. *et al.* Quantum-limited heat conduction over macroscopic distances. *Nat. Phys.* **12,** 460–464 (2016).
43. Bozyigit, D. *et al.* Antibunching of microwave-frequency photons observed in correlation measurements using linear detectors. *Nat. Phys.* **7,** 154–158 (2011).
44. Masuda, S. *et al.* Cryogenic microwave source based on nanoscale tunnel junctions. Preprint at http://arxiv.org/abs/1612.06822 (2016).
45. Suri, B. *et al.* Nonlinear microwave photon occupancy of a driven resonator strongly coupled to a transmon qubit. *Phys. Rev. A* **92,** 063801 (2015).
46. Lindström, T. *et al.* Properties of high-quality coplanar waveguide resonators for QIP and detector applications. *J. Phys.* **150,** 052140 (2009).

Acknowledgements

The authors thank M. Meschke, J.P. Pekola, M. Silveri and H. Grabert for insightful discussions. This work is supported by the European Research Council under Starting Independent Researcher Grant No. 278117 (SINGLEOUT) and under Consolidator Grant No. 681311 (QUESS), by the Academy of Finland through its Centres of Excellence Program (Grant Nos 251748 and 284621) and Grants (Nos 135794, 272806, 265675, 276528, 286215 and 305306), the Emil Altonen Foundation, the Jenny and Antti Wihuri Foundation and the Finnish Cultural Foundation. We also acknowledge the provision of facilities and technical support by Aalto University at Micronova Nanofabrication Centre.

Author contributions

K.Y.T. fabricated the samples, developed and conducted the experiments, and analysed the data. M.P. contributed to the sample fabrication, measurements and data analysis. R.E.L. and J.G. contributed to the measurements. S.M. contributed to the theoretical analysis of the system. M.M. provided the initial ideas and suggestions for the experiment, and supervised the work in all respects. All authors discussed both experimental and theoretical results and commented on the manuscript, which was written by K.Y.T. and M.M.

Additional information

Supplementary Information accompanies this paper at http://www.nature.com/naturecommunications

Competing interests: The authors declare no competing financial interests.

How to cite this article: Tan, K. Y. *et al.* Quantum-circuit refrigerator. *Nat. Commun.* **8,** 15189 doi: 10.1038/ncomms15189 (2017).

arXiv:1712.10256v1 [cond-mat.mes-hall] 29 Dec 2017

Flux-tunable heat sink for quantum electric circuits

M. Partanen,[1] K. Y. Tan,[1] S. Masuda,[1] J. Govenius,[1] R. E. Lake,[1,2] M. Jenei,[1] L. Grönberg,[3] J. Hassel,[3] S. Simbierowicz,[3] V. Vesterinen,[1,3] J. Tuorila,[1,4,5] T. Ala-Nissila,[4,6,7] and M. Möttönen[1]

[1] *QCD Labs, COMP Centre of Excellence, Department of Applied Physics, Aalto University, P.O. Box 13500, FI-00076 Aalto, Finland*
[2] *National Institute of Standards and Technology, Boulder, Colorado, 80305, USA*
[3] *VTT Technical Research Centre of Finland, P.O. Box 1000, FI-02044 VTT, Finland*
[4] *MSP group, COMP Centre of Excellence, Department of Applied Physics, Aalto University, P.O. Box 13500, FI-00076 Aalto, Finland*
[5] *Nano and Molecular Systems Research Unit, University of Oulu, P.O. Box 3000, FI-90014 Oulu, Finland*
[6] *Departments of Mathematical Sciences and Physics, Loughborough University, Loughborough, Leicestershire LE11 3TU, United Kingdom*
[7] *Department of Physics, Brown University, Box 1843, Providence, Rhode Island 02912-1843, USA*

(Dated: January 1, 2018)

Superconducting microwave circuits show great potential for practical quantum technological applications such as quantum information processing. However, fast and on-demand initialization of the quantum degrees of freedom in these devices remains a challenge. Here, we experimentally implement a tunable heat sink that is potentially suitable for the initialization of superconducting qubits. Our device consists of two coupled resonators. The first resonator has a high quality factor and a fixed frequency whereas the second resonator is designed to have a low quality factor and a tunable resonance frequency. We engineer the low quality factor using an on-chip resistor and the frequency tunability using a superconducting quantum interference device. When the two resonators are in resonance, the photons in the high-quality resonator can be efficiently dissipated. We show that the corresponding loaded quality factor can be tuned from above 10^5 down to a few thousand at 10 GHz in good quantitative agreement with our theoretical model.

INTRODUCTION

One of the most promising approaches to building a quantum computer is based on superconducting qubits in the framework of circuit quantum electrodynamics[1–6]. However, not all of the criteria for a functional quantum computer[7] have been achieved simultaneously at the desired level. In particular, computational errors need to be mitigated with quantum error correction[8,9]. Many quantum error correction codes require frequent initialization of ancillary qubits during the computation. Thus, fast and accurate qubit reset is a typical requirement in the efficient implementation of quantum algorithms. To date, several approaches for qubit initialization have been studied[10–14]. Initialization to the ground state by waiting is a straightforward method but it becomes impractical in repeated measurements of qubits with long lifetimes. Therefore, active initialization is advantageous. Furthermore, it may be beneficial to design individual circuits for qubit control, readout, and initialization in order to avoid performance-limiting compromises in the optimization of the circuit parameters. In this work we focus on a specialized initialization circuit, which remains to be implemented in superconducting quantum processors.

Recently, a promising qubit initialization protocol based on dissipative environments was proposed in Refs. 15 and 16. In this proposal, a resistor coupled to a frequency-tunable resonator quickly absorbs the excitation from the qubit when tuned in resonance. In this paper, we experimentally realize such a tunable dissipative environment and study its effect on a superconducting resonator. Tunable superconducting resonators have been demonstrated previously[17–22] but without engineered dissipation arising from on-chip normal-metal components. In addition to quantum computing, very sensitive cryogenic detectors[23–25] may benefit from tunable dissipation for calibration purposes. Furthermore, tunable transmission lines are also useful in studying fundamental quantum phenomena[26].

Although dissipation is in some cases beneficial for quantum computing[27], lossy materials are typically harmful for qubit lifetimes during computation. Therefore, one needs to be able to switch the dissipation on and off deterministically. In state-of-the-art experiments, quality factors, Q, above 10^6 indicating very low dissipation have been achieved with coplanar-waveguide resonators[28]. Various materials and methods have been studied for fabricating high-Q resonators[29–32]. Here we fabricate high-Q resonators based on niobium on a silicon wafer. In addition, we tune the Q factor from above 10^5 down to a few thousand by coupling the resonator relatively strongly to a dissipative element. Importantly, the integrated resistive element we introduce does not inherently degrade the Q factor when it is weakly coupled to the resonator compared with similarly fabricated resonators without any engineered resistive elements.

RESULTS

Experimental samples

The structure of our device is presented in Fig. 1 together

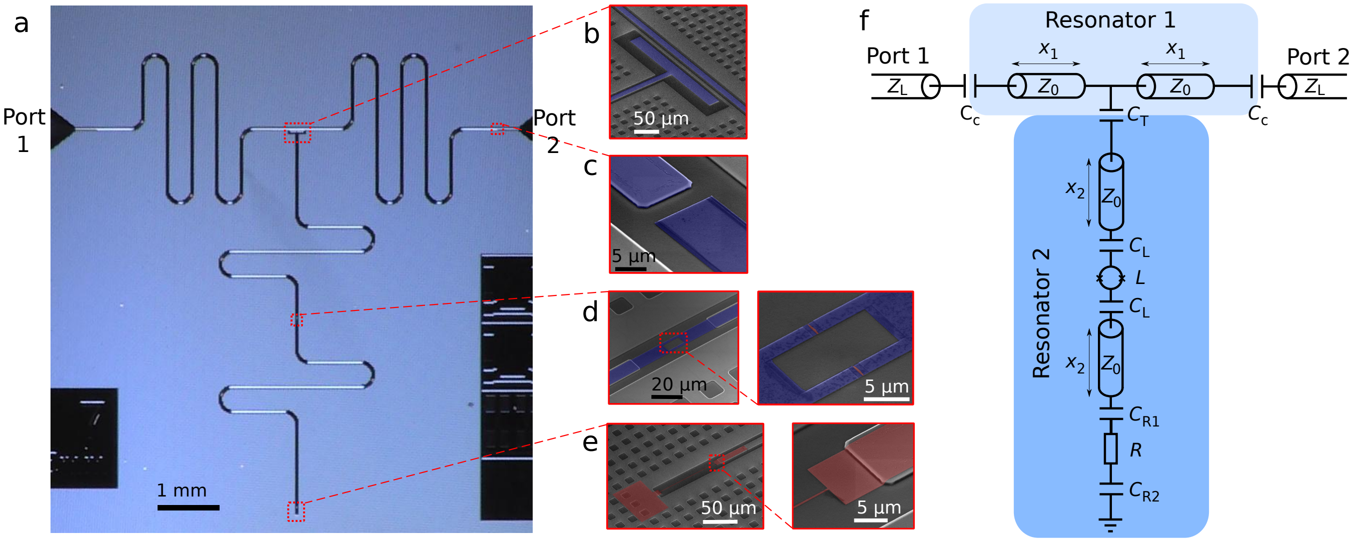

Figure 1. Sample structure. (a) Optical top image of the measured sample. (b) False-colour scanning electron microscope image of the coupling capacitor between the two resonators, and (c) between Resonator 1 (light blue) and the port to the external transmission line (dark blue). (d) Two micrographs of the SQUID loop highlighted in blue and the junctions highlighted in red. (e) Two micrographs of the termination Cu resistor (red). (f) Electrical circuit diagram of the sample. Resonators 1 and 2 with characteristic impedances Z_0 are coupled to each other by a coupling capacitance C_{T} and to external transmission lines with characteristic impedance Z_{L} by capacitances C_{C}. The inductance of the SQUID is denoted by L, and the termination resistance by R. The SQUID is connected to the centre conductor of Resonator 2 line with capacitances C_{L}, and the resistor to centre conductor and ground with C_{R1} and C_{R2}, respectively. The lengths of the resonator sections are denoted by $x_{1/2}$. The image in panel (a) is from Sample A, and those in panels (b)–(e) from Sample B.

Table I. Simulation parameters. See Fig. 1f and text for the definition of the symbols. Samples A and B have the same parameter values except for the length x_2, where the value for Sample B is given in parenthesis.

Parameter	C_{C} (fF)	C_{T} (fF)	C_{L} (pF)	C_{R1} (pF)	C_{R2} (pF)	C_{l} (pF/m)	R (Ω)	Z_0 (Ω)	Z_{L} (Ω)	$\varepsilon_{\mathrm{eff}}$	x_1 (mm)	x_2 (mm)	$Q_{\mathrm{int,1}}$	I_0 (nA)
Value	1	5	2.8	4.0	28	180	375	50	50	6.35	12	7.5 (8.0)	1×10^5	255

with the corresponding electrical circuit diagram which defines the symbols used below. The device consists of two coupled resonators, Resonator 1 with a fundamental frequency of 2.5 GHz, and Resonator 2 with a tunable frequency. Both ends of Resonator 1 couple capacitively (C_{C}) to external circuitry for scattering parameter measurements. The even harmonics of Resonator 1 interact with Resonator 2 since there is a voltage antinode at the center of the half-wave Resonator 1, and hence, the capacitive (C_{T}) coupling to Resonator 2 is significant.

The resonators are fabricated out of niobium in a coplanar-waveguide geometry. The modes of Resonator 2 are tunable owing to a superconducting quantum interference device (SQUID) acting as a flux-tunable inductance, placed in the middle of the resonator. The SQUID is integrated into the center pin of the waveguide and consists of two aluminium layers separated by an insulating aluminium oxide layer. When the resonance frequencies of the two resonators meet, we expect a degradation of the Resonator 1 quality factor because Resonator 2 is terminated with a dissipative on-chip resistor made of copper. Importantly, the device is designed to retain a high quality factor of Resonator 1 whenever Resonator 2 is far detuned.

We study two samples, Sample A and B, which are nominally identical, except for the length of Resonator 2. We mostly focus on Sample A which has a wider tuning range of the quality factor of Resonator 1. The samples are measured at a cryostat temperature of approximately 10 mK. The theoretical model described in Methods reveals all the essential features of the two samples with a single set of parameters given in Table I. See Methods for the details of the sample fabrication.

Flux dependence of the resonance frequencies

The first four resonances of Resonator 1 in Sample A are shown in Fig. 2 as a function of the magnetic flux through the SQUID. The first and the third mode at approximately 2.5 and 7.5 GHz, respectively, do not depend on the flux due to a voltage node in the middle of Resonator 1, i.e., at the coupling capacitor C_{T}. Thus, these

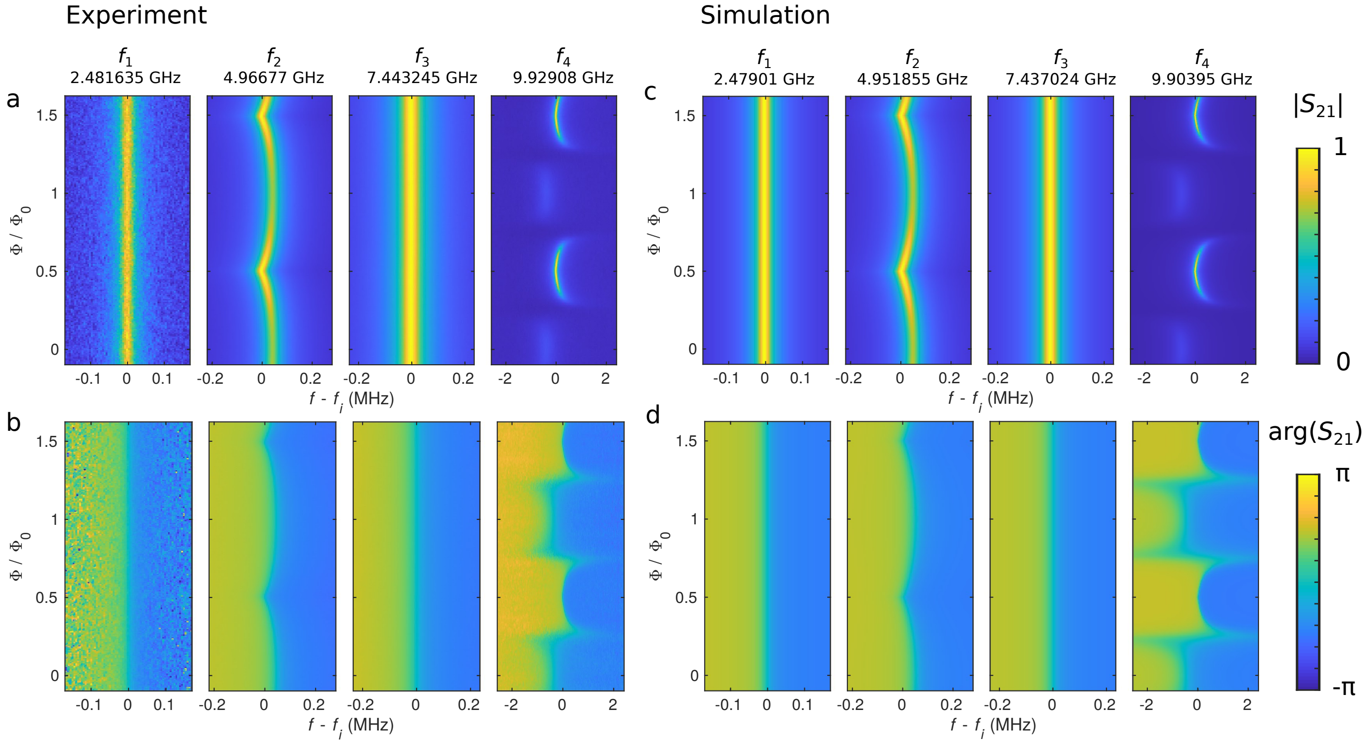

Figure 2. Resonances of Sample A. (a,b) Experimental and (c,d) computational (a,c) amplitude and (b,d) phase of the scattering parameter S_{21} for the first four modes of Resonator 1 as functions of frequency and magnetic flux. The amplitude of S_{21} in each subpanel is normalized independently by dividing with the corresponding maximum amplitude. The power in the measurements is approximately -90 dBm at Port 1. The resonance frequencies at half flux quantum are given above the panels, and the simulation parameters are given in Table I.

modes are decoupled from those of Resonator 2. In contrast, the second and the fourth mode at 5 and 10 GHz, respectively, show clear flux dependence owing to the changing SQUID inductance, which in turn changes the frequencies of the modes in Resonator 2. If a dissipative mode in Resonator 2 approaches the frequency of a mode in Resonator 1, we observe two distinctive features: the resonance in Resonator 1 shifts and broadens owing to the coupling to the dissipative mode. The experimental scattering parameter S_{21} is normalized as explained in Methods. The simulation based on the theoretical model (see Methods) shows excellent agreement with experimental data. The slight discrepancy between the experiment and the simulation mainly arises from the uncertainty in the exact values of the parameters given in Table I.

The distinctively different flux dependence of modes 2 and 4 in Sample A is clarified by Fig. 3b, which shows simulated $|S_{21}|$ with only Resonator 2, i.e., in the limit $C_{\mathrm{C}} \to \infty$. Resonator 2 has a flux dependent resonance near 4 GHz, which does not cross the second mode of Resonator 1 at 5 GHz. Nevertheless, it comes sufficiently near 5 GHz, which explains the frequency shift of mode 2 of Resonator 1. In contrast, Resonator 2 has a flux dependent resonance near 10 GHz, very close to mode 4 of Resonator 1. The resonances intersect which results in dramatic changes in the fourth mode of Resonator 1. The second mode of Resonator 2 near 8 GHz has a current node at the center of the resonator, where the SQUID is located; thus, it is only very weakly dependent on the flux.

Supplementary Fig. 1 shows results similar to those in Fig. 2 for Sample A but for modes 2, 3, and 4 of Sample B. The simulations and experiments are also here in good agreement. However, the simulated mode 2 is substantially narrower than the experimental one. This broadening may arise from an unaccounted mode of the sample holder at a nearby frequency. Furthermore, there is some discrepancy in the phase of mode 4 near integer flux quanta. This discrepancy can be explained by uncertainty in the normalization procedure with very small amplitudes. The first mode is outside the frequency range of the used microwave components, and hence we do not show data for it. For a quantitative comparison of the measured and the simulated resonance frequencies in Samples A and B, Supplementary Fig. 2 shows the frequency shifts of modes 2 and 4 extracted from Fig. 2 and Supplementary Fig. 1. The flux dependence of the modes of Resonator 2 is similar in Sample B to that of Sample A as shown in Supplementary Fig. 3b. However, the resonances do not intersect at 10 GHz although they are very close to each other.

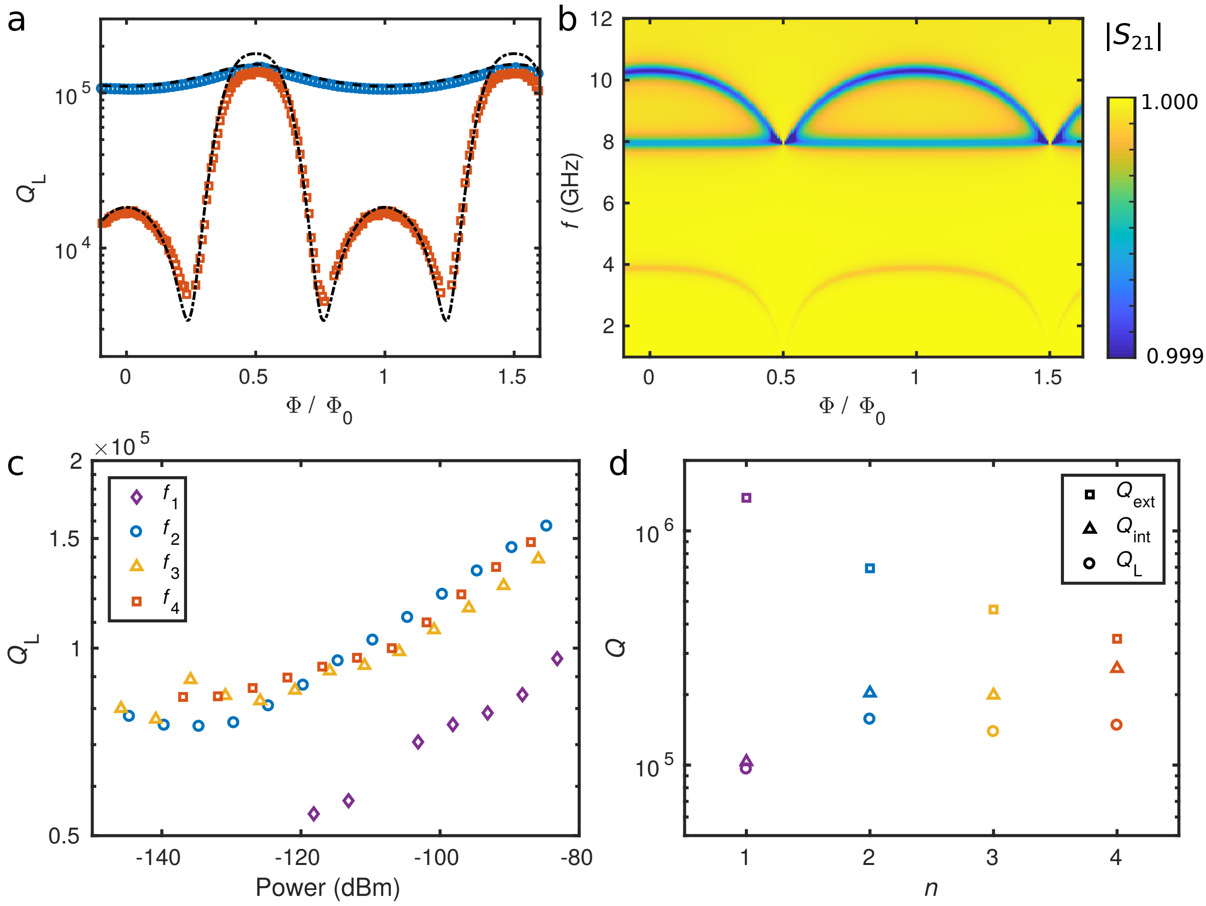

Figure 3. Quality factors of Resonator 1 and resonances of Resonator 2 for Sample A. (a) Measured loaded quality factor, Q_L, for mode 2 (blue circles) and for mode 4 (red squares) as functions of the magnetic flux through the SQUID together with the simulated values (dashed line and dash-dotted line, respectively). (b) Absolute value of the simulated scattering parameter S_{21} of Sample A with only Resonator 2, i.e., at the limit $C_\mathrm{C} \to \infty$. The colour bar is truncated at 0.999 for clarity. (c) Measured loaded quality factor, Q_L, of Sample A (markers) for the first four modes as functions of power at Port 1. (d) Measured Q_L of Sample A (circles), predicted external quality factor, Q_ext, (squares) and calculated internal quality factor, Q_int, (triangles) as functions of the mode number. The simulation parameters are given in Table I. In (a), the power at Port 1 is approximately -90 dBm, and in (d) -85 dBm. In (c) and (d), the magnetic flux through the SQUID is $\Phi/\Phi_0 = 0.5$.

Quality factors

We also analyze the quality factors as functions of flux, as shown for Sample A in Fig. 3a, and for Sample B in Supplementary Fig. 3a. The Q factors of the second and fourth mode are tunable unlike in the case of the first and third mode. The second mode of Sample A shows only relatively small variation near 10^5 whereas the fourth mode can be tuned from above 10^5 down to a few thousand. For Sample B, the flux dependence of the Q factor is similar. However, the second mode has a substantially lower experimental loaded quality factor, Q_L, than the simulated value, i.e., a broader resonance peak as discussed above. A better agreement between the simulation and the experiment can be obtained by introducing an additional loss mechanism as described in the caption of Supplementary Fig. 3.

The power dependence of the quality factors is analyzed in Fig. 3c for the four lowest modes in Sample A. The Q factors decrease with decreasing power as expected[32]. Nevertheless, they remain rather close to 10^5 even at the single-photon level, around -140 dBm. However, relatively high powers enable more accurate measurements of the losses caused by the resistor when the resonators are tuned into the weak coupling regime. Figure 3d shows the experimentally obtained loaded quality factor, Q_L, and the theoretically predicted external quality factor, Q_ext, corresponding to the losses through the coupling capacitors C_C as functions of the mode number n. Furthermore, the internal quality factor, Q_int, corresponding to the internal losses in the system is calculated from the equation $Q_\mathrm{int}^{-1} = Q_\mathrm{L}^{-1} - Q_\mathrm{ext}^{-1}$. The internal quality factor slightly increases with the mode number and obtains values near 2.5×10^5. The minimum value of $Q_\mathrm{L} \lesssim 5 \times 10^3$ in Fig. 3a gives also the minimum value for Q_int since the internal losses of the system dominate when the resistor is strongly coupled to the fourth mode

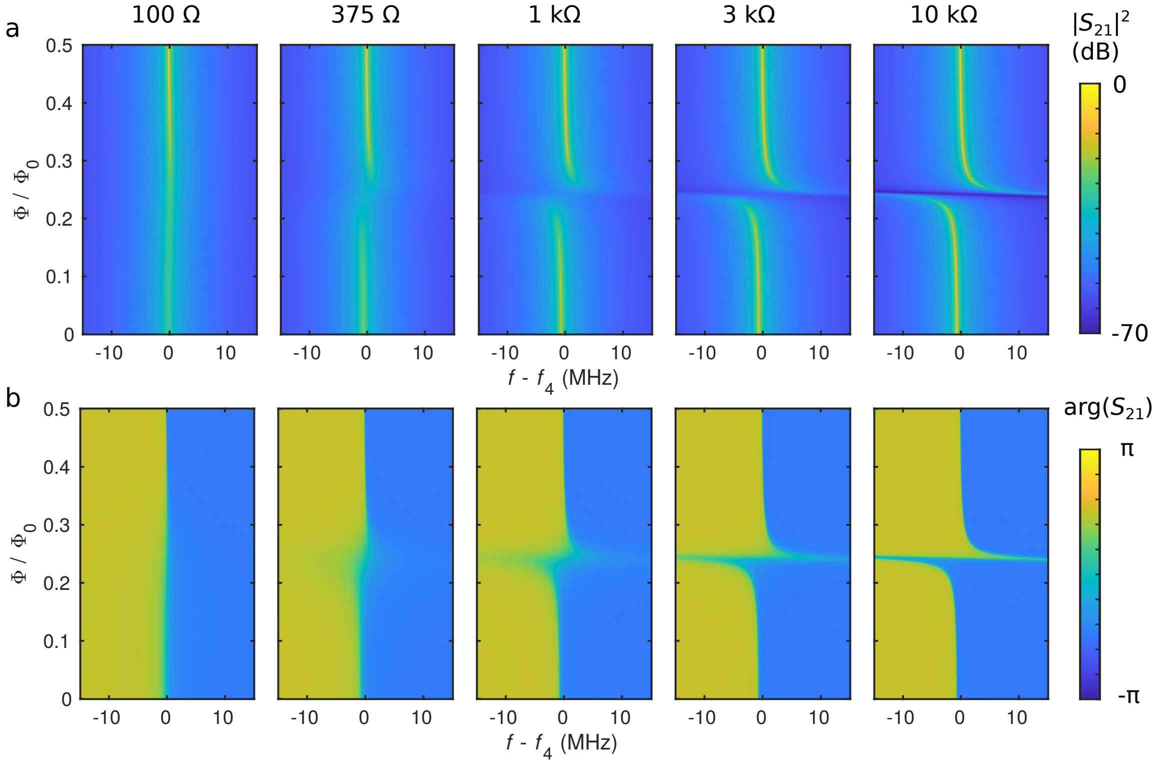

Figure 4. Effect of the termination resistance. Simulated (a) amplitude, and (b) phase of the mode 4 in Sample A as functions of frequency and magnetic flux with different resistance values, R, as indicated above the panels. The resonance frequency is $f_4 = 9.90395$ GHz, and the other parameters are given in Table I.

of Resonator 1.

The minimum and maximum Q_{int} correspond to photon lifetimes $\tau_{\text{int}} = Q_{\text{int}}/\omega_0$ of 80 ns and 4 μs, respectively, at $\omega_0 = 2\pi \times 10$ GHz when other losses are neglected. Furthermore, Q_{ext} corresponds to a photon lifetime of 6 μs. These photon lifetimes are long compared to the period of the coherent oscillations between the two resonators at resonance, $\tau_{\text{T}} = 30$ ns (see Methods). Thus, the internal or external losses of Resonator 1 are not dominating over the coupling strength between the resonators. However, the simulated Q factors of the lowest modes of Resonator 2 in Fig. 3b are well below 40 at the zero flux bias and also at $\Phi/\Phi_0 \approx 0.2$ which corresponds to the crossing of the modes at 10 GHz. They obtain values above 100 only in the range $0.48 < \Phi/\Phi_0 < 0.52$ due to the ideally diverging SQUID inductance. Thus, the photon lifetime in Resonator 2 is below 0.6 ns at 10 GHz and at the relevant flux point. Consequently, the photons in Resonator 2 are dissipated quickly compared to the period of the coherent oscillations between the resonators, which prevents the formation of well-separated modes hybridized between the resonators. Importantly, Resonator 2 mostly functions as a tunable dissipative environment for Resonator 1, the dissipation of which is limited by the coupling strength between the resonators.

Simulations with different resistances

We also simulate the effect of changing the termination resistance as shown in Fig. 4. The other parameters in the simulations are from Sample A. Note the different frequency range and colour scale compared to Fig. 2. In the case of a 100-Ω termination resistance, there is very little shift in the resonance frequency as a function of the magnetic flux. Nevertheless, the width of the peak varies since the ideal SQUID inductance diverges, $L \to \infty$ for $\Phi/\Phi_0 \to 0.5$, and therefore, it decouples the resistor from Resonator 1. At even lower resistances near 50 Ω (not shown), the termination is well matched to the characteristic impedance, and hence the description of Resonator 2 as a resonator becomes obscure. Instead, it appears as a broad-band dissipative environment for Resonator 1. With increasing resistance, Resonator 2 obtains well-defined resonances, with zero-flux Q factors becoming of the order of 10^3 at $R = 10$ kΩ. However, the maximum Q_{L} in Resonator 1 of 1.8×10^5 does not vary due to the ideally infinite impedance of the SQUID at $\Phi/\Phi_0 \to 0.5$. In contrast at zero flux, Q_{L} increases from 1.0×10^4 to 1.3×10^5 as the resistance increases from 100 Ω to 10 kΩ. At $R = 10$ kΩ, the two resonators show a clear avoided-crossing feature. There is a continuous crossover from a single modulating resonance at low resistance values to two resonances with an avoided crossing at high resistances. In the experiments, we have $R = 375$ Ω, which results in a single modulating resonance with some avoided-crossing-like features.

DISCUSSION

We have experimentally demonstrated tunable dissipation in a device consisting of two resonators in very good agreement with our theoretical model. We have studied two samples with slightly different parameters. Both of them allow us to substantially tune the loaded quality factors of the relevant resonances. In addition, the internal quality factor of one of the modes can be tuned from approximately a quarter of a million down to a few thousand. Importantly, we have designed the circuit such that the coupling strength between the resonators is somewhat weaker than the dissipation in Resonator 1 and stronger than the dissipation in Resonator 2. Therefore, Resonator 2 operates as an efficient dissipative environment for Resonator 1. Note that the spurious internal losses in the system are low as indicated by the high maximum quality factor. Thus, the fabrication of the on-chip resistors is compatible with obtaining high quality factors using our fabrication process. To our knowledge, these are the highest demonstrated quality factors in superconducting resonators with integrated on-chip resistors. In the future, the remaining unwanted losses can be reduced by further improving the process.

Here, we have demonstrated a tunable dissipative environment with a rather specific sample type. Nevertheless, the geometry and parameters can be relatively freely chosen to optimize the heat sink for different applications. For instance, it is possible to modify the losses by changing the resistance and capacitance values. Furthermore, the geometry of the system can be changed in order to obtain different coupling strengths for different modes. In addition, the resistor does not necessarily have to be directly coupled to Resonator 2. Instead, it can be outside the resonator and coupled with a small capacitance and a section of a transmission line. Furthermore, in case the resistance equals to the characteristic impedance of the transmission line resonator, the environment is effectively similar to a transmission line[19].

Although we consider the resistors only as sources of dissipation here, they may also be engineered to simultaneously function in photon-absorbing normal-metal–insulator–superconductor tunnel junctions[33], or quasiparticle traps in superconducting circuits[34–38]. Fast tuning of the quality factors can be obtained by introducing microwave flux bias lines. A lower bound for the time scale of the flux tuning is given by the plasma frequency of the SQUID, which is of the order of 30 GHz in our samples. In the future, qubits can be integrated into this system enabling the demonstration the protocol for fast and accurate initialization[16].

METHODS

Theoretical model and simulations

We analyze the electrical circuit shown in Fig 1f, which also defines the symbols employed below. The input impedance of Resonator 2 can be obtained from standard microwave circuit analysis[39], and it is given by

$$Z_{\mathrm{r2}} = \frac{1}{i\omega C_{\mathrm{T}}} + \frac{Z_0\left\{Z_{\mathrm{S}} + Z_0\tanh(\gamma x_2) + \frac{Z_0[Z_{\mathrm{term}} + Z_0\tanh(\gamma x_2)]}{Z_0 + Z_{\mathrm{term}}\tanh(\gamma x_2)}\right\}}{Z_0 + \tanh(\gamma x_2)\left\{Z_{\mathrm{S}} + \frac{Z_0[Z_{\mathrm{term}} + Z_0\tanh(\gamma x_2)]}{Z_0 + Z_{\mathrm{term}}\tanh(\gamma x_2)}\right\}}, \tag{1}$$

where $Z_{\mathrm{S}} = i\omega L + 2/(i\omega C_{\mathrm{L}})$ is the impedance of the SQUID and the parallel plate capacitors connecting the SQUID to the center conductor, and $Z_{\mathrm{term}} = R + 1/(i\omega C_{\mathrm{R1}}) + 1/(i\omega C_{\mathrm{R2}})$ is the impedance of the terminating resistor and the capacitances connecting it to the center conductor and the ground plane. Here, $\omega = 2\pi f$ is the angular frequency of the measurement tone, and γ is the wave propagation coefficient detailed below. We consider the SQUID as a tunable classical inductor. The inductance of the SQUID as a function of the magnetic flux Φ is ideally given by $L(\Phi) = \Phi_0/[2\pi I_0|\cos(\pi\Phi/\Phi_0)|]$, where I_0 is the maximum supercurrent through the SQUID, and $\Phi_0 = h/(2e)$ is the magnetic flux quantum. The losses in the SQUID are assumed to be substantially smaller than those induced by the resistor; thus, they are neglected. One could also include a capacitance in parallel with the inductance in the model but it would have only a minor effect as discussed below.

We can calculate the scattering parameter from Port 1 to Port 2 using the ABCD matrix method[39]

$$S_{21} = \frac{2}{A + B/Z_L + CZ_L + D}, \tag{2}$$

where the coefficients are obtained from

$$\begin{pmatrix} A & B \\ C & D \end{pmatrix} = \begin{pmatrix} 1 & \frac{1}{i\omega C_{\mathrm{C}}} \\ 0 & 1 \end{pmatrix} \begin{pmatrix} \cosh(\gamma x_1) & Z_0\sinh(\gamma x_1) \\ \frac{1}{Z_0}\sinh(\gamma x_1) & \cosh(\gamma x_1) \end{pmatrix} \begin{pmatrix} 1 & 0 \\ \frac{1}{Z_{\mathrm{r2}}} & 1 \end{pmatrix} \begin{pmatrix} \cosh(\gamma x_1) & Z_0\sinh(\gamma x_1) \\ \frac{1}{Z_0}\sinh(\gamma x_1) & \cosh(\gamma x_1) \end{pmatrix} \begin{pmatrix} 1 & \frac{1}{i\omega C_{\mathrm{C}}} \\ 0 & 1 \end{pmatrix}. \tag{3}$$

These equations are solved numerically with Matlab.

The simulation parameters are given in Table I. We use identical parameters in the simulations for both samples except that the length x_2 is different. The capacitances C_{C} and C_{T} are based on finite-element-method (FEM) calculations with design geometry and without native oxides, whereas C_{L}, C_{R1}, and C_{R2} are calculated using parallel-plate-capacitor model by deducing the areas from scanning electron microscope images, and assuming the niobium oxide to have a typical thickness[40] of 5 nm and relative permittivity[41] of 6.5. The capacitance per unit length of the coplanar waveguide $C_{\rm l}$ is also based on a FEM simulation. The resistance R is measured with a dc control sample in a four-probe setup at 10 mK. The test resistor is fabricated in the same process with the actual samples. The effective permittivity of the waveguide $\epsilon_{\rm eff}$ is obtained from the nominal widths of the centre conductor and the gap, 10 μm and 5 μm respectively, using an analytical formula[42]. The lengths x_1 and x_2 are design values. The internal quality factor of the first mode of Resonator 1 alone, $Q_{\rm int,1}$, is based on measurements of control samples consisting of a single resonator, and it agrees well with the measured first mode of Sample A. The characteristic impedance of the external lines $Z_{\rm L}$ has a nominal value, and the characteristic impedance of the resonators Z_0 has a design value in good agreement with the experimental results. The maximum supercurrent through the SQUID I_0 is used as the only fitting parameter since it cannot be directly measured in the actual sample. Nevertheless, the critical current in the actual samples is relatively close to a switching current of approximately 180 nA measured with a dc setup in an essentially similar but separately fabricated control SQUID. Due to noise from a high-temperature environment via the dc lines, the temperature of the control SQUID may be higher than in the actual sample, thus providing an explanation to the difference in the critical current and the switching current. In addition, the difference may well be explained by unintentional differences in the fabrication. We can write the wave propagation coefficient as $\gamma = \omega_1/(2Q_{\rm int,1}v_{\rm ph}) + i\omega/v_{\rm ph}$, where $v_{\rm ph} = c/\sqrt{\varepsilon_{\rm eff}}$ is the phase velocity, $\omega_1/(2\pi) = c/(4x_1\sqrt{\varepsilon_{\rm eff}})$ is the fundamental frequency, and c is the speed of light in vacuum.

The loaded quality factor can be defined as $Q_{\rm L} = \omega_0 E/P_{\rm loss}$, where $\omega_0 = 2\pi f_0$ is the angular frequency of the resonance, E the energy stored in the resonator, and $P_{\rm loss} = -{\rm d}E/{\rm d}t$ the power loss. Without input power, the energy in the resonator evolves as a function of time t as $E(t) = E_0\exp(-\omega_0 t/Q_{\rm L})$, where E_0 is the initial energy. Thus, the photon lifetime is given by $\tau_{\rm L} = Q_{\rm L}/\omega_0$, which corresponds to the total losses described by $Q_{\rm L}$. Since the number of photons in a resonator n depends on the energy as $E = n\hbar\omega_0$, where $\hbar$ is the reduced Planck constant, and the power loss is bounded from above by the input power $P_{\rm in}$ in the steady state, one obtains an upper bound for the photon number as $n < Q_{\rm L}P_{\rm in}/(\omega_0^2\hbar)$. Therefore, the average photon number in a 10-GHz resonator is near unity or below if the Q factor is 10^5 and the input power is -140 dBm (c.f. Fig. 3). The external quality factor corresponding to the leakage through the coupling capacitors can be calculated as[5] $Q_{\rm ext} = 2x_1C_{\rm l}/(4Z_{\rm L}\omega_0C_{\rm C}^2)$. Although $Q_{\rm ext}$ calculated with this formula is quite sensitive to errors especially in $C_{\rm C}$, it can be considered at least as an order-of-magnitude estimate. The external quality factor is related to the coupling strength describing the external ports, $\kappa_{\rm ext} = \omega_0/Q_{\rm ext} = 2\pi\times 30$ kHz at $\omega_0 = 2\pi\times 10$ GHz. In addition, one can write the photon lifetime without other loss mechanisms as $\tau_{\rm ext} = Q_{\rm ext}/\omega_0 = 1/\kappa_{\rm ext} = 6$ μs. The coupling to the external ports can be compared with the coupling strength between the resonators at resonance calculated as[43] $g_{\rm T} = C_{\rm T}V_1V_2/\hbar = 2\pi\times 10$ MHz, where $V_i = \sqrt{\hbar\omega_0/(2x_iC_{\rm l})}$, $i = 1, 2$, and $\omega_0 = 2\pi\times 10$ GHz. Furthermore, the period for coherent oscillations between the resonators can be written as[3] $\tau_{\rm T} = \pi/g_{\rm T} = 30$ ns, where we have neglected dissipation.

The junction capacitance can be estimated using a parallel-plate model with an approximate aluminium oxide thickness of 2 nm, a junction area of 0.25 μm estimated from micrographs, and a typical relative permittivity[44] of 8.2, which yield 10 fF per junction. At zero flux and 5 GHz (10 GHz), the inductive reactance of the SQUID is 40 Ω (80 Ω) whereas the capacitor consisting of two junctions in parallel has a reactance of 2 kΩ (0.9 kΩ). If included in the model, the capacitive shunt of the inductance could result in a very small change of the scattering parameter S_{21} at $\Phi/\Phi_0 \approx 0.5$ where the inductance ideally diverges. The change is small owing to the weak coupling of the resonators. Consequently, we do not include it in the model. Thus, the effect of the capacitance is effectively included in that of the inductance, which depends on the fitting parameter I_0. The plasma frequency of the SQUID can be obtained as $\omega_{\rm p}/(2\pi) = 1/(2\pi\sqrt{LC})$, where L is the inductance and C the capacitance of the junctions.

Sample fabrication

Samples A and B are fabricated in the same process. The actual samples as well as the control samples are fabricated on 100-mm Si wafers. First, native SiO_2 is removed with ion beam etching, and 200 nm of Nb is sputtered onto the waver without breaking the vacuum.

Second, the large patterns are defined using standard optical lithography. The optical lithography begins with hexamethyldisilazane priming, followed by spin coating the resist AZ5214E at 4000 rpm. The resist is exposed using a mask aligner in a hard-contact mode, and the exposed resist is removed with the developer AZ351B. In order to obtain a positive profile for the Nb edges, we apply a reflow bake at 140°C before reactive ion etching. Once the large patterns are ready, we pre-dice the wafer half way from the back side.

In the third step, the nanostructures are defined using electron beam lithography (EBL). After thorough cleaning of the wafer with a plasma stripper, a resist for EBL is spin-coated to the wafer. The EBL resist consists of two layers: poly(methyl methacrylate) with 4% of anisole, and poly[(methyl methacrylate)-co-(methacrylic acid)] with 11% of ethyl lactate. We fabricate all the nanostructures in a single EBL write. For the development, we use a 1:3 solution of methyl isobutyl ketone and isopropanol. The metallization for the nanostructures is carried out with an electron beam evaporator in two steps. First, the Cu resistor is evaporated followed by the evaporation of the SQUID. We evaporate Cu only on the area in the vicinity of the resistor on the chip and keep the rest of the chip covered by a metal mask. Subsequently, we cover the resistor and evaporate the Al structures. The SQUID consists of two Al layers evaporated at two angles ($\pm 15°$). The oxide layer for the Josephson junctions is obtained by oxidizing Al in situ in the evaporation chamber at 1 mbar of O_2 for 5 min. The lift-off process is carried out in acetone followed by cleaning with isopropanol. The Cu resistor has a width of 250 nm, thickness of 30 nm, and length of 90 μm. The SQUID consists of two layers of Al with thicknesses of 40 nm each, and it has a loop area of approximately 50 μm^2.

Measurement setup

The measurement setup is shown in Supplementary Fig. 4. The measurements are carried out in a dry dilution refrigerator with a base temperature of approximately 10 mK, and the scattering parameters are measured with a vector network analyzer (VNA). We control the magnetic flux through the SQUID using an external coil attached to the sample holder, and the current through the coil is generated with a source-measure unit (SMU). The sample is wire-bonded to a printed circuit board shielded by a sample holder that is fabricated out of Au-plated Cu. The sample holder is placed inside a magnetic shield to mitigate magnetic-field noise.

Normalization of scattering parameters

All raw experimental scattering parameters are normalized. First, the winding of the phase as a function of frequency is cancelled for convenience by multiplying S_{21} with $\exp(i2\pi f\tau)$ where $\tau \approx 50$ ns. Second, the circle in the complex plane drawn by S_{21} when the frequency is swept through the resonance is shifted and rotated to its canonical position, where the circle intersects the origin and the maximum amplitude lies on the positive x axis[45]. Any uncertainty in this shift causes relatively large errors near origin; hence, we use linear scale for experimental data as it emphasizes the large amplitudes with smaller relative error. Consequently, one can extract the Q factor using the phase–frequency fitting method discussed in Ref. 45. In addition to the experimental Q factors, we use the same method for obtaining the Q factor also from the simulations, except that the very low Q factor of Resonator 2 is obtained from the width of the dip. In order to exclude uncertainty related to the cable losses, we normalize S_{21} by dividing it with $\max_{f,\Phi}|S_{21}|$ separately for each mode. The magnetic flux is extracted from the periodicity of the of modes 2 and 4, and there can be an irrelevant offset of an integer number of flux quanta. One flux quantum corresponds to an electric current of approximately 2 mA in the coil used.

---

[1] Ladd, T. D. *et al.* Quantum computers. *Nature* **464**, 45–53 (2010). URL `http://dx.doi.org/10.1038/nature08812`.

[2] Clarke, J. & Wilhelm, F. K. Superconducting quantum bits. *Nature* **453**, 1031–1042 (2008). URL `http://dx.doi.org/10.1038/nature07128`.

[3] Blais, A., Huang, R.-S., Wallraff, A., Girvin, S. M. & Schoelkopf, R. J. Cavity quantum electrodynamics for superconducting electrical circuits: An architecture for quantum computation. *Phys. Rev. A* **69**, 062320 (2004). URL `http://link.aps.org/doi/10.1103/PhysRevA.69.062320`.

[4] Wallraff, A. *et al.* Strong coupling of a single photon to a superconducting qubit using circuit quantum electrodynamics. *Nature* **431**, 162–167 (2004). URL `http://dx.doi.org/10.1038/nature02851`.

[5] Göppl, M. *et al.* Coplanar waveguide resonators for circuit quantum electrodynamics. *J. Appl. Phys.* **104**, 113904 (2008). URL `https://doi.org/10.1063/1.3010859`.

[6] Kelly, J. *et al.* State preservation by repetitive error detection in a superconducting quantum circuit. *Nature* **519**, 66–69 (2015). URL `http://dx.doi.org/10.1038/nature14270`.

[7] DiVincenzo, D. P. The physical implementation of quantum computation. *Fortschr. Phys.* **48**, 771–783 (2000). URL `http://dx.doi.org/10.1002/1521-3978(200009)48:9/11<771::AID-PROP771>3.0.CO;2-E`.

[8] Lidar, D. & Brun, T. (eds.) *Quantum Error Correction* (Cambridge University Press, 2013).

[9] Terhal, B. M. Quantum error correction for quantum memories. *Rev. Mod. Phys.* **87**, 307–346 (2015). URL `https://link.aps.org/doi/10.1103/RevModPhys.87.307`.

[10] Valenzuela, S. O. *et al.* Microwave-induced cooling of a superconducting qubit. *Science* **314**, 1589–1592 (2006). URL `http://science.sciencemag.org/content/314/5805/1589`.

[11] Johnson, J. E. *et al.* Heralded state preparation in a superconducting qubit. *Phys. Rev. Lett.* **109**, 050506 (2012). URL `https://link.aps.org/doi/10.1103/PhysRevLett.109.050506`.

[12] Ristè, D., van Leeuwen, J. G., Ku, H.-S., Lehnert, K. W. & DiCarlo, L. Initialization by measurement of a superconducting quantum bit circuit. *Phys. Rev. Lett.* **109**, 050507 (2012). URL `https://link.aps.org/doi/10.1103/PhysRevLett.109.050507`.

[13] Geerlings, K. *et al.* Demonstrating a driven reset protocol for a superconducting qubit. *Phys. Rev. Lett.* **110**, 120501 (2013). URL `https://link.aps.org/doi/10.1103/PhysRevLett.110.120501`.

[14] Bultink, C. C. *et al.* Active resonator reset in the nonlinear dispersive regime of circuit QED. *Phys. Rev. Applied* **6**, 034008 (2016). URL `https://link.aps.org/doi/10.1103/PhysRevApplied.6.034008`.

[15] Jones, P. J., Huhtamäki, J. A. M., Salmilehto, J., Tan, K. Y. & Möttönen, M. Tunable electromagnetic environment for superconducting quantum bits. *Sci. Rep.* **3**, 1987 (2013). URL `http://dx.doi.org/10.1038/srep01987`.

[16] Tuorila, J., Partanen, M., Ala-Nissila, T. & Möttönen, M. Efficient protocol for qubit initialization with a tunable environment. *npj Quantum Inf.* **3**, 27 (2017). URL `https://doi.org/10.1038/s41534-017-0027-1`.

[17] Palacios-Laloy, A. *et al.* Tunable resonators for quantum circuits. *J. Low Temp. Phys.* **151**, 1034–1042 (2008). URL

https://doi.org/10.1007/s10909-008-9774-x.

[18] Healey, J. E., Lindström, T., Colclough, M. S., Muirhead, C. M. & Tzalenchuk, A. Y. Magnetic field tuning of coplanar waveguide resonators. *Appl. Phys. Lett.* **93**, 043513 (2008). URL https://doi.org/10.1063/1.2959824.

[19] Pierre, M., Svensson, I.-M., Sathyamoorthy, S. R., Johansson, G. & Delsing, P. Storage and on-demand release of microwaves using superconducting resonators with tunable coupling. *Appl. Phys. Lett.* **104**, 232604 (2014). URL https://doi.org/10.1063/1.4882646.

[20] Wang, Z. L. *et al.* Quantum state characterization of a fast tunable superconducting resonator. *Appl. Phys. Lett.* **102**, 163503 (2013). URL https://doi.org/10.1063/1.4802893.

[21] Vissers, M. R. *et al.* Frequency-tunable superconducting resonators via nonlinear kinetic inductance. *Appl. Phys. Lett.* **107**, 062601 (2015). URL https://doi.org/10.1063/1.4927444.

[22] Adamyan, A. A., Kubatkin, S. E. & Danilov, A. V. Tunable superconducting microstrip resonators. *Appl. Phys. Lett.* **108**, 172601 (2016). URL https://doi.org/10.1063/1.4947579.

[23] Inomata, K. *et al.* Single microwave-photon detector using an artificial λ-type three-level system. *Nat. Commun.* **7**, 12303 (2016). URL http://dx.doi.org/10.1038/ncomms12303.

[24] Govenius, J., Lake, R. E., Tan, K. Y. & Möttönen, M. Detection of zeptojoule microwave pulses using electrothermal feedback in proximity-induced Josephson junctions. *Phys. Rev. Lett.* **117**, 030802 (2016). URL https://link.aps.org/doi/10.1103/PhysRevLett.117.030802.

[25] Narla, A. *et al.* Robust concurrent remote entanglement between two superconducting qubits. *Phys. Rev. X* **6**, 031036 (2016). URL https://link.aps.org/doi/10.1103/PhysRevX.6.031036.

[26] Wilson, C. M. *et al.* Observation of the dynamical Casimir effect in a superconducting circuit. *Nature* **479**, 376–379 (2011). URL http://dx.doi.org/10.1038/nature10561.

[27] Verstraete, F., Wolf, M. M. & Ignacio Cirac, J. Quantum computation and quantum-state engineering driven by dissipation. *Nat. Phys.* **5**, 633 (2009). URL http://dx.doi.org/10.1038/nphys1342.

[28] Megrant, A. *et al.* Planar superconducting resonators with internal quality factors above one million. *Appl. Phys. Lett.* **100**, 113510 (2012). URL https://doi.org/10.1063/1.3693409.

[29] Vissers, M. R. *et al.* Low loss superconducting titanium nitride coplanar waveguide resonators. *Appl. Phys. Lett.* **97**, 232509 (2010). URL https://doi.org/10.1063/1.3517252.

[30] Sandberg, M. *et al.* Etch induced microwave losses in titanium nitride superconducting resonators. *Appl. Phys. Lett.* **100**, 262605 (2012). URL http://dx.doi.org/10.1063/1.4729623.

[31] Bruno, A. *et al.* Reducing intrinsic loss in superconducting resonators by surface treatment and deep etching of silicon substrates. *Appl. Phys. Lett.* **106**, 182601 (2015). URL https://doi.org/10.1063/1.4919761.

[32] Zmuidzinas, J. Superconducting microresonators: Physics and applications. *Annu. Rev. Condens. Matter Phys.* **3**, 169–214 (2012). URL https://doi.org/10.1146/annurev-conmatphys-020911-125022.

[33] Tan, K. Y. *et al.* Quantum-circuit refrigerator. *Nat. Commun.* **8**, 15189 (2017). URL http://dx.doi.org/10.1038/ncomms15189.

[34] Goldie, D. J., Booth, N. E., Patel, C. & Salmon, G. L. Quasiparticle trapping from a single-crystal superconductor into a normal-metal film via the proximity effect. *Phys. Rev. Lett.* **64**, 954–957 (1990). URL https://link.aps.org/doi/10.1103/PhysRevLett.64.954.

[35] Ullom, J. N., Fisher, P. A. & Nahum, M. Measurements of quasiparticle thermalization in a normal metal. *Phys. Rev. B* **61**, 14839–14843 (2000). URL https://link.aps.org/doi/10.1103/PhysRevB.61.14839.

[36] Rajauria, S. *et al.* Efficiency of quasiparticle evacuation in superconducting devices. *Phys. Rev. B* **85**, 020505 (2012). URL https://link.aps.org/doi/10.1103/PhysRevB.85.020505.

[37] Riwar, R.-P. *et al.* Normal-metal quasiparticle traps for superconducting qubits. *Phys. Rev. B* **94**, 104516 (2016). URL https://link.aps.org/doi/10.1103/PhysRevB.94.104516.

[38] Patel, U., Pechenezhskiy, I. V., Plourde, B. L. T., Vavilov, M. G. & McDermott, R. Phonon-mediated quasiparticle poisoning of superconducting microwave resonators. *Phys. Rev. B* **96**, 220501 (2017). URL https://link.aps.org/doi/10.1103/PhysRevB.96.220501.

[39] Pozar, D. *Microwave Engineering* (John Wiley & Sons, Hoboken, 2011), 4th edn.

[40] Bach, D. *EELS investigations of stoichiometric niobium oxides and niobium-based capacitors.* Ph.D. thesis, Universität Karlsruhe (TH) (2009).

[41] Graça, M., Saraiva, M., Freire, F., Valente, M. & Costa, L. Electrical analysis of niobium oxide thin films. *Thin Solid Films* **585**, 95–99 (2015). URL http://www.sciencedirect.com/science/article/pii/S0040609015001650.

[42] Gevorgian, S., Linner, L. & Kollberg, E. CAD models for shielded multilayered CPW. *IEEE Trans. Microw. Theory Techn.* **43**, 772–779 (1995). URL https://doi.org/10.1109/22.375223.

[43] Jones, P. J., Salmilehto, J. & Möttönen, M. Highly controllable qubit-bath coupling based on a sequence of resonators. *J. Low Temp. Phys.* **173**, 152–169 (2013). URL http://dx.doi.org/10.1007/s10909-013-0889-3.

[44] Landry, G., Dong, Y., Du, J., Xiang, X. & Xiao, J. Q. Interfacial capacitance effects in magnetic tunneling junctions. *Appl. Phys. Lett.* **78**, 501–503 (2001). URL https://doi.org/10.1063/1.1336816.

[45] Petersan, P. J. & Anlage, S. M. Measurement of resonant frequency and quality factor of microwave resonators: Comparison of methods. *J. Appl. Phys.* **84**, 3392–3402 (1998). URL http://dx.doi.org/10.1063/1.368498.

Acknowledgements We acknowledge the provision of facilities and technical support by Aalto University at OtaNano - Micronova Nanofabrication Centre. We thank H. Grabert, M. Silveri, A. Wallraff, J. Kelly, J. Goetz and D. Hazra for discussions, and R. Kokkoniemi and S. Patomäki for technical assistance. We have received funding from the European Research Council under Starting Independent Researcher Grant No. 278117 (SINGLEOUT) and under Consolidator Grant No. 681311 (QUESS), the Academy of Finland through its Centres of Excellence Program (project nos 251748 and 284621) and grants (Nos. 265675, 286215, 276528, 305237, 305306, 308161 and 314302), the Vilho, Yrjö and

Kalle Väisälä Foundation, the Technology Industries of Finland Centennial Foundation, and the Jane and Aatos Erkko Foundation.

Author Contributions M.P. was responsible for sample design, fabrication, measurements, data analysis, and for the writing of the initial version of the manuscript. K.Y.T and J.G. contributed to the sample design, fabrication, measurements, and analysis. S.M. contributed to the analysis, and M.J. to the measurements and analysis. L.G. deposited the Nb layer. M.P., K.Y.T, J.G, R.E.L., L.G., J.H., S.S., V.V., and M.M. developed the fabrication process. J.T. and T.A.-N. contributed to the theoretical understanding of the system. M.M. provided initial ideas and supervised the project. All authors commented on the manuscript.

Competing financial interests The authors declare no competing financial interests.

Data availability The data is available upon request from the authors.

Supplementary material Supplementary Figures 1, 2, 3, 4.

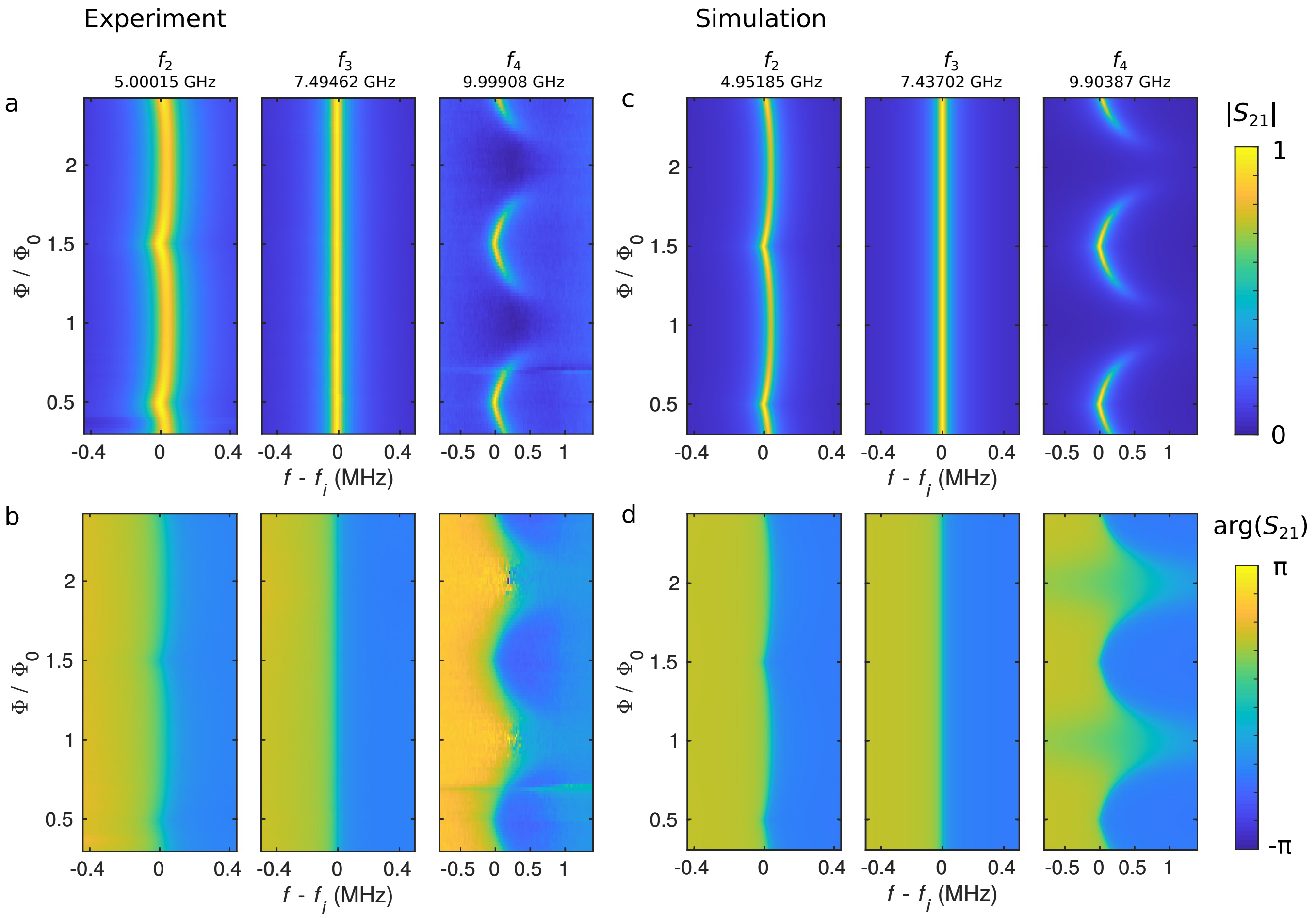

Supplementary Figure 1. Resonances of Sample B. (a,b) Experimental and (c,d) computational scattering parameter S_{21} for the modes 2,3, and 4 of Resonator 1 as functions of frequency and magnetic flux. (a,c) Normalized amplitude of S_{21}. Each panel is normalized separately by dividing with the corresponding maximum amplitude. (b,d) Phase of S_{21}. The resonance frequencies are given above the panels, and the simulation parameters are given in Table I. The power in the experiments is approximately -90 dBm at Port 1.

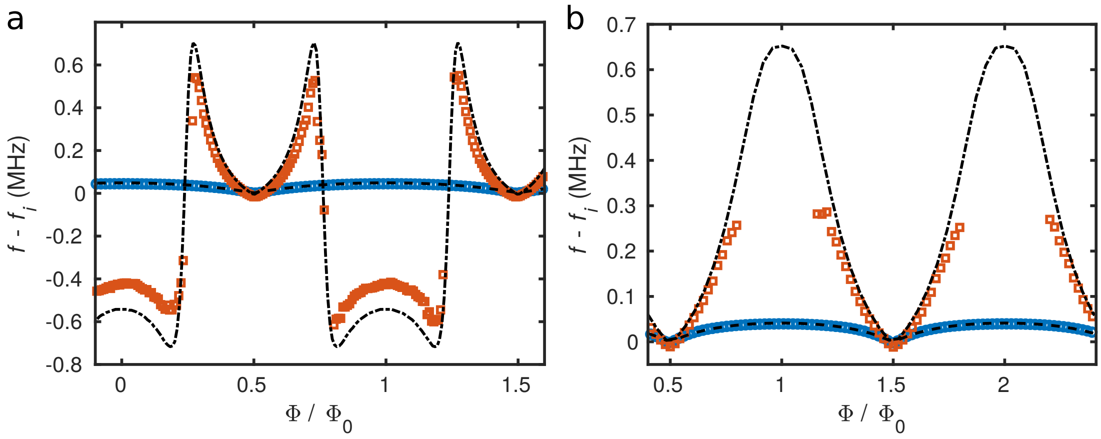

Supplementary Figure 2. Resonance frequency shifts from the magnetic flux point $\Phi/\Phi_0 = 0.5$. (a) Measured frequency shifts of modes 2 (blue circles) and 4 (red squares) together with the corresponding simulations for modes 2 (dashed line) and 4 (dash-dotted line) of Sample A as functions of the magnetic flux. (b) As (a) but for Sample B. The simulation parameters are given in Table I. For the frequencies $f_{2/4}$ in Samples A and B, see Fig. 2 and Supplementary Fig. 1, respectively.

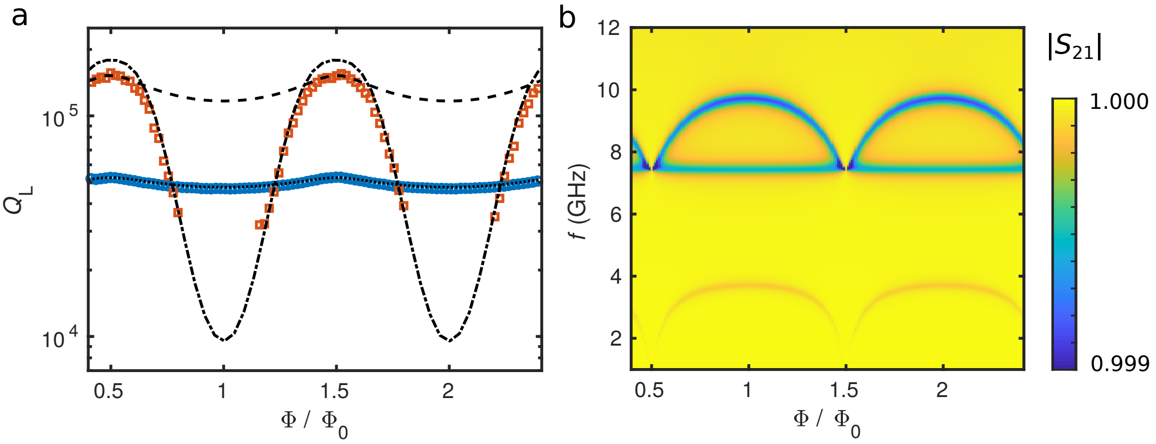

Supplementary Figure 3. Quality factors of Resonator 1 and resonances of Resonator 2 for Sample B. (a) Measured loaded quality factor, Q_{L}, for mode 2 (blue circles), and for mode 4 (red squares) as functions of the magnetic flux through the SQUID together with the simulated values (dashed line and dash-dotted line, respectively). The dotted line on top of the blue circles shows the simulation for the mode 2 with an additional spurious loss mechanism with a flux-independent quality factor of $Q_{\mathrm{sp}} = 8 \times 10^4$ in addition to the simulated quality factor, $Q_{\mathrm{L,si}}$, yielding $Q_{\mathrm{L}}^{-1} = Q_{\mathrm{L,si}}^{-1} + Q_{\mathrm{sp}}^{-1}$ with a better match with the experimental data. The applied power is approximately -90 dBm at Port 1. (b) Absolute value of the simulated scattering parameter S_{21} with only Resonator 2, i.e., at the limit $C_{\mathrm{C}} \to \infty$. The colour bar is truncated at 0.999 for clarity. The simulation parameters are given in Table I.

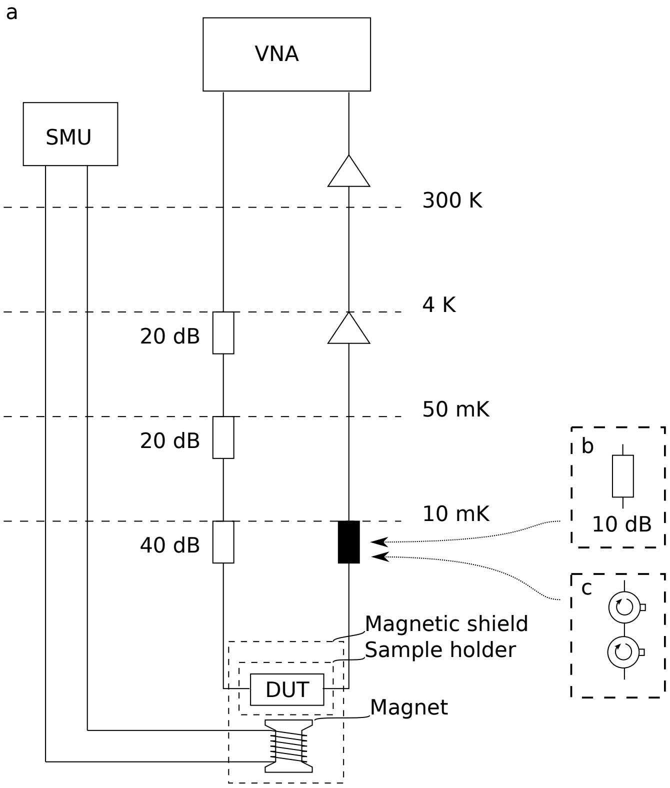

Supplementary Figure 4. Measurement setup. (a) Overview of the measurement setup with different temperature stages of the cryostat indicated. The scattering parameters of the device under test (DUT) are measured with a vector network analyzer (VNA), and the magnetic flux through the SQUID is produced with a bias current generated by a source measure unit (SMU). (b) For Sample A, a 10-dB attenuator is employed after the sample in the position of the black box to prevent amplifier noise from entering the sample. (c) For Sample B, two isolators are used instead.

Summer trainee project 2018, Department of Applied Physics

Research group:	Quantum Computing and Devices (QCD)
Contact person:	Dr. Mikko Möttönen (mikko.mottonen@aalto.fi)
Field of research:	Nanoelectronics and Quantum Computing
Project title:	Control and measurement of superconducting qubits
Project instructor:	Dr. Jan Goetz, M.Sc. Joni Ikonen
Site of research:	Aalto University, QCD group, Otaniemi
Website	Click here!
Level of student:	applications from all students are welcome (also for people applying for a Mater's or PhD thesis project)

Introduction

Quantum computer is an emerging computational device that can potentially solve some problems of practical interest that are impossible for the classical computer due to the required computational resources. Quantum bits, qubits, are the key ingredient of the quantum computer. Qubits can be employed to store and process quantum information, and they can be measured to extract classical information out of the quantum world.

One of the greatest developments of quantum technologies in the recent years has been the rise of circuit quantum electrodynamics (cQED). Here, superconducting qubits are coupled to microwave resonators and waveguides working at microwave frequencies. This allows not only to reproduce quantum optics experiments carried out with optical photons but also for a spectrum new physics and applications. For the quantum computer, one of the outstanding problems is the implementation of fast and precise qubit operations and measurements.

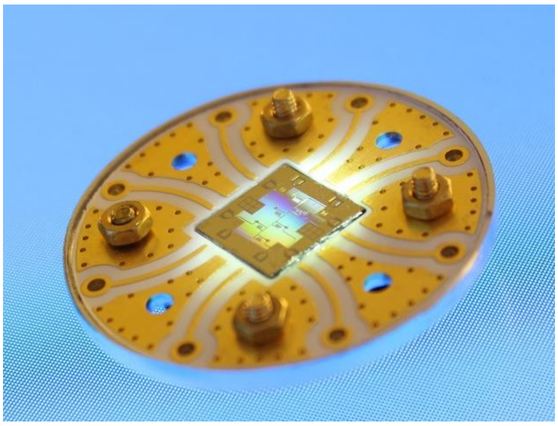

Figure 1. Sample holder together with a silicon chip in the center. There are six superconducting qubits on the chip made in QCD Labs. Figure credit: Jan Goetz/QCD

Project goals

Your aim in this project is to (i) characterize the thermal residual population in a superconducting qubit, (ii) implement a so-called random benchmark protocol to study and improve the fidelity of the quantum logic operations, and (iii) implement and develop qubit measurement techniques.

Research site

Your site of research will be the premises of Quantum Computing and Devices, the so-called QCD Labs, on the Otaniemi campus of Aalto University. There are both theorists and experimentalists working in the group. See the group website (http://physics.aalto.fi/en/groups/qcd/) for more information.

Instructors

Your main instructor will be Dr. Jan Goetz or MSc Joni Ikonen depending on whether the project is more experimental or theoretical.

Working methods

The main focus of the project can be adjusted according to your level and interests.

Most of the above-mentioned goals are experimental, i.e., implementation of know schemes for qubits which have already been fabricated before summer. This requires studying the theory and programming the measurement equipment. However, in the development of novel methods such as that of the quantum measurement, deep theoretical knowledge is to be obtained and analytical calculations and numerical simulations need to be carried out.

Thesis possibilities

Depending on your level, this project can be adjusted for a BSc thesis, special assignment, MSc thesis, or a PhD thesis project. Some knowledge of quantum mechanics and an excellent study record is preferred.

Summer trainee project 2018, Department of Applied Physics

Research group:	Quantum Computing and Devices (QCD)
Contact person:	Dr. Mikko Möttönen (mikko.mottonen@aalto.fi)
Field of research:	Dilute Bose-Einstein condensates, ultracold quantum gases
Project title:	Quantum knots
Project instructor:	M.Sc. Tuomas Ollikainen, Dr. Mikko Möttönen
Site of research:	Aalto University, QCD Labs, Otaniemi
Website	Click here!
Level of student:	applications from all students are welcome (also for people applying for a Mater's or PhD thesis project)

Introduction

Bose-Einstein condensation is basically a manifestation of macroscopic occupation of a single quantum state. The idea of such a macroscopic occupation dates back to 1924–1925, when Albert Einstein extended the statistical arguments presented by Satyendra Nath Bose to systems consisting of a conserved number of bosonic particles. Einstein recogniced that at sufficiently low temperatures the quantum statistical distribution of an ideal gas of bosons shows *condensation* of a macroscopic fraction of the material into the ground state of the system. This phenomenon, subsequently termed Bose–Einstein condensation (BEC), is a unique, purely quantum mechanical phase transition in the sense that it occurs in principle even in noninteracting bosonic systems. Nowadays BECs are routinely produced in research laboratories around the world and they provide a unique opportunity to study fundamental quantum phenomena.

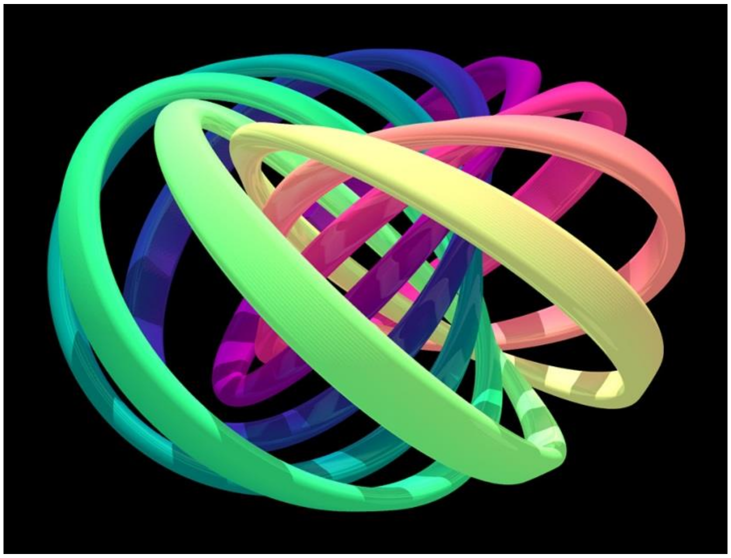

Figure 1. Visualization of the first quantum knot.
(Credit: David Hall)

Recently, we created and observe knot-like structures referred to as knot solitons in quantum-mechanical order parameter describing a BEC. See the attached manuscript that was published in Nature Physics. Although knots have been tied in the classical ropes for millennia and considered in classical fields for more than a century, no one had previously observed a single knot in the context of quantum dynamics.

Project goals

Currently, the knots are created in the polar order parameter of a ^{87}Rb condensate which tends to decay into the ferromagnetic phase. This decay will also destroy the knots. Your project is to study the dynamics of the created knots and find ways for their stabilization in BECs.

Research site

Your site of research will be the premises of Quantum Computing and Devices, the so-called QCD Labs, on the Otaniemi campus of Aalto University. There are both theorists and experimentalists working in the group. See the group website (http://physics.aalto.fi/groups/comp/qcd/) for more information.

Instructors

Your instructor will be M.Sc. Tuomas Ollikainen supported by Dr. Mikko Möttönen.

Working methods

Your work will involve building the theoretical understanding of BECs and monopoles. You will also carry out numerical modeling using CUDA.

Thesis possibilities

Depending on your level, this project can be adjusted for a BSc thesis, special assignment, MSc thesis, or a PhD thesis project. Prior knowledge of quantum mechanics and an excellent study record is a prerequisite.

Tying Quantum Knots*

D. S. Hall,[1] M. W. Ray,[1] K. Tiurev,[2] E. Ruokokoski,[2] A. H. Gheorghe,[1] and M. Möttönen[2]
[1] *Department of Physics and Astronomy, Amherst College, Amherst, Massachusetts 01002–5000, USA*
[2] *QCD Labs, COMP Centre of Excellence, Department of Applied Physics,*
Aalto University, P.O. Box 13500, FI–00076 Aalto, Finland
(Dated: December 31, 2015)

Knots are familiar entities that appear at a captivating nexus of art, technology, mathematics, and science [1]. As topologically stable objects within field theories, they have been speculatively proposed as explanations for diverse persistent phenomena, from atoms and molecules [2] to ball lightning [3] and cosmic textures in the universe [4]. Recent experiments have observed knots in a variety of classical contexts, including nematic liquid crystals [5–7], DNA [8], optical beams [9, 10], and water [11]. However, no experimental observations of knots have yet been reported in quantum matter. We demonstrate here the controlled creation [12] and detection of knot solitons [13, 14] in the order parameter of a spinor Bose–Einstein condensate. The experimentally obtained images of the superfluid directly reveal the circular shape of the soliton core and its accompanying linked rings. Importantly, the observed texture corresponds to a topologically non-trivial element of the third homotopy group [15] and demonstrates the celebrated Hopf fibration [16], which unites many seemingly unrelated physical contexts [17, 18]. Our observations of the knot soliton establish an experimental foundation for future studies of their stability and dynamics within quantum systems [19].

Knots are defined mathematically as closed curves in three-dimensional space [1]. A trivial example is a circle, which is also known as an unknot. More complicated knots have been extensively classified and tabulated by determining whether they can be continuously deformed, one into another, without permitting the curve to pass through itself. Although nontrivial knots are commonly associated with physical strings, they can also appear in line-like vortices, the cores of which trace the closed curves. A celebrated example is Kelvin's early atomic theory, which is linked to the existence and dynamics of knotted vortex rings in an ethereal fluid [2]. More recently, nontrivial vortex knots have been created and identified experimentally in water [11] and optical beams [9, 10], and discussed theoretically in the context of superfluid turbulence [20].

Knots can also appear as particle-like solitons in classical and quantum fields [21], the nature of which has been a subject of intense mathematical interest for more than eighty years [16]. In this case, the closed curve is a ring that describes the core of the soliton. This ring is surrounded by an infinite number of similar rings, each linked with all of the others to generate a knotted field structure [22]. For example, the classical Maxwell's equations admit solutions that involve knot solitons in which the rings are electric and magnetic field lines [23]. Quantum-mechanical examples have been theoretically proposed [13, 14] for the Faddeev–Skyrme model, in which each of the linked rings consists of the points in space sharing a particular direction of the field.

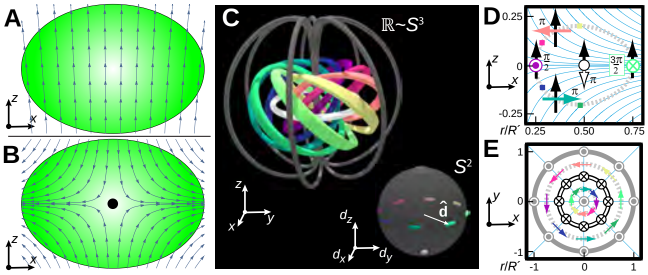

Figure 1 | Structure of the knot soliton and the method of its creation. a,**b**, Schematic magnetic field lines before (a) and during (b) the knot formation, with respect to the condensate (green ellipse). **c**, Knot soliton configuration in real space and its relation to the nematic vector $\hat{\mathbf{d}}$ in S^2 (inset). The inner white ring ($d_z = -1$, $m = 0$) is the core of the knot soliton. The surrounding coloured bands ($d_z = 0$, $m = \pm 1$) define the surface of a torus, with colours representing the azimuthal angle of $\hat{\mathbf{d}}$ which winds by 2π in both the toroidal and poloidal directions. The outer dark grey rings ($d_z = 1$, $m = 0$) indicate the boundary of the soliton. **d**,**e**, When tying the knot, the initially z-pointing nematic vector (black arrows) precesses about the direction of the local magnetic field (cyan lines) to achieve the final configuration (coloured arrows). The dashed grey line shows where $d_z = 0$, the white line indicates the soliton core ($d_z = -1$), and the dark grey line defines the boundary of the volume ($d_z = 1$).

In general, knot solitons are non-singular topological excitations [15] that change smoothly and non-trivially in all three spatial dimensions. They are therefore described by the third homotopy group, π_3, which classifies such textures according to whether or not they can be continuously transformed into one another. One-dimensional solitons and singular vortex lines, both belonging to the fundamental group π_1, have been identified experimentally in superfluids [24–26], as have two-dimensional skyrmions [27] and singular monopoles [28] belonging to the second homotopy group, π_2. Since singular defects within π_3 are unrealisable monopoles in four

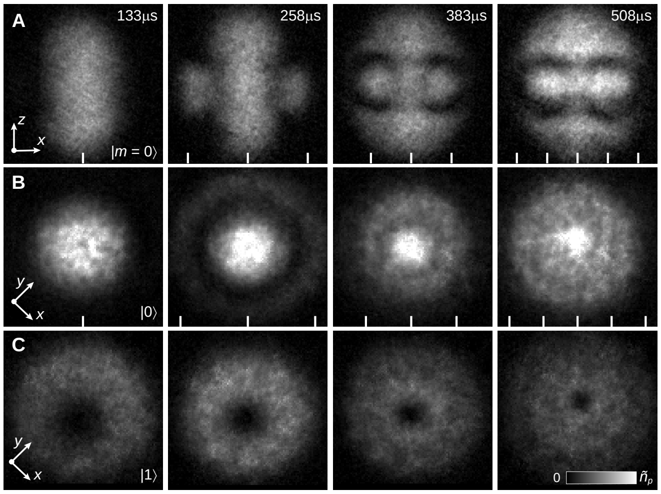

Figure 2 | Tying the knot soliton by winding the nematic vector. Experimental side (**a**) and top (**b,c**) images of the atomic column density of the $m = 0$ (**a,b**) and $m = -1$ (**c**) spinor components at the indicated evolution times. Continuous rotation of the nematic vector brings the knot soliton into the condensate through its boundary, where the directors rotate by 2π in ~ 440 μs. The intensity peaks inside the circular intensity dips (a) show the core of the knot soliton. The dips correspond to the colourful torus shown in Fig. 1c occupied by the $m = \pm 1$ components (see also Fig. 3). The analytical locations of the core and regions for which $d_z = 1$ [see equation (7)] are shown as ticks on the horizontal axes. For (**a**) the field of view is 246 μm × 246 μm and the maximum pixel intensity corresponds to column densities in excess of $\tilde{n}_p = 8.5 \times 10^8$ cm^{-2}; for (**b,c**) these quantities are respectively 219 μm × 219 μm and $\tilde{n}_p = 1.0 \times 10^9$ cm^{-2}.

spatial dimensions, the knot soliton is an instance of the only general texture type that has not yet been identified experimentally within a medium described by a quantum-mechanical order parameter.

In this Letter we demonstrate the creation and observation of knot solitons in the polar phase of a spinor Bose–Einstein condensate. We adopt the theoretical method proposed in ref. [12] and implement it using experimental techniques that have recently been used to create Dirac monopoles [29] and isolated monopoles [28]. An overview of the experiment is given in Fig. 1. The core of the knot soliton is first observed as a ring of enhanced particle density at the periphery of the condensate that shrinks inwards as time advances (Fig. 2). The presence of the soliton is confirmed by its excellent agreement with analytical theory and with numerical simulations (Fig. 3). Strikingly, we directly image the linked structure of the knot soliton, as shown in Fig. 4.

The order parameter describing a spin-1 Bose–Einstein condensate may be written as

$$\Psi(\mathbf{r},t) = \sqrt{n(\mathbf{r},t)}e^{i\phi(\mathbf{r},t)}\zeta(\mathbf{r},t) \tag{1}$$

where n is the atomic density, ϕ is a scalar phase, and $\zeta = (\zeta_{+1}, \zeta_0, \zeta_{-1})^{\mathrm{T}}$ is a three-component z-quantized spinor

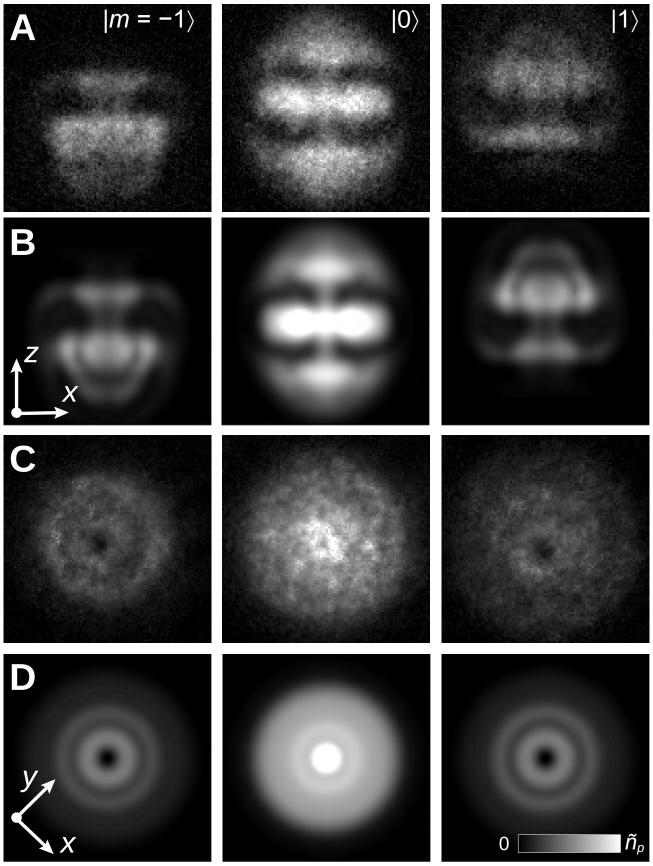

Figure 3 | Comparison of experiment with theory. Side (**a**,**b**) and top (**c**,**d**) images of the experimentally (**a**,**c**) and theoretically (**b**,**d**) obtained atomic column densities in all different spinor components as indicated. The number of particles is 2.4×10^5, and the knot is tied for $T_{\mathrm{evolve}} = 558$ μs. For (**a**,**b**) the field of view is 246 μm × 246 μm and the maximum pixel intensity corresponds to column densities in excess of $\tilde{n}_p = 8.5 \times 10^8$ cm^{-2}; for (**c**,**d**) these quantities are 219 μm × 219 μm and $\tilde{n}_p = 1.0 \times 10^9$ cm^{-2}, respectively.

with $\zeta_m = \langle m|\zeta\rangle$. We restrict our attention here to the polar phase of the condensate, which is obtained by spin rotations

$$\mathcal{D}(\alpha,\beta)\begin{pmatrix}0\\1\\0\end{pmatrix} = \frac{1}{\sqrt{2}}\begin{pmatrix}-e^{-i\alpha}\sin\beta\\ \sqrt{2}\cos\beta\\ e^{i\alpha}\sin\beta\end{pmatrix} = \frac{1}{\sqrt{2}}\begin{pmatrix}-d_x+id_y\\ \sqrt{2}d_z\\ d_x+id_y\end{pmatrix} \tag{2}$$

for angles β and α about the y and z axes, respectively. The polar order parameter may therefore be expressed as

$$\Psi(\mathbf{r},t) = \sqrt{n(\mathbf{r},t)}e^{i\phi(\mathbf{r},t)}\hat{\mathbf{d}}(\mathbf{r}) \tag{3}$$

in terms of the nematic vector, $\hat{\mathbf{d}}$, defined by equation (2).

The nematic vector field $\hat{\mathbf{d}}(\mathbf{r})$ maps points in real space $\mathbf{r} \in \mathbb{R}^3$ to points on the surface of the unit sphere $\hat{\mathbf{d}} \in S^2$. In our case, the nematic vector assumes a constant value,

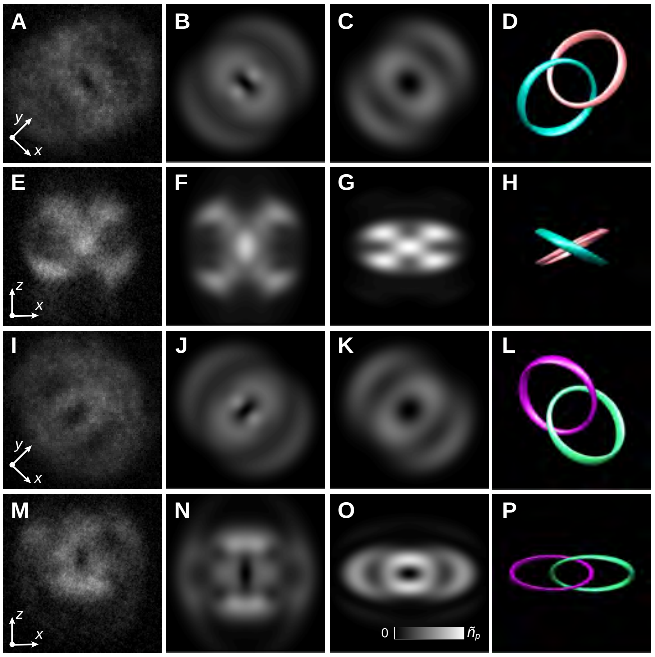

Figure 4 | Linked preimages. Experimental (**a**) and simulated (**b**) top images of the $m = 0$ spinor component for $T_{\mathrm{evolve}} = 508\ \mu$s and projections along $-x$, where the maximum pixel intensity corresponds to column densities in excess of $\tilde{n}_p = 1.0 \times 10^9$ cm^{-2} and the field of view 219 μm × 219 μm. **c**, Simulated top image of the condensate prior to expansion, with $\tilde{n}_p = 2.6 \times 10^{11}$ cm^{-2}. Projection along $\alpha \in \{\pm x, \pm y\}$ results in a column density with pronounced intensity along the preimages of $d_\alpha = 1$ and $d_\alpha = -1$. **d**, Preimages of $d_x = \pm 1$ from the simulation of panel (c), with colours corresponding to those of Fig. 1c. The field of view in (c,d) is 15 μm × 15 μm. **e–h**, Same as (a–d), but for images taken from the side. The field of view in (e,f) is 246 μm × 246 μm with $\tilde{n}_p = 8.5 \times 10^8$ cm^{-2}, and the field of view in (g,h) is the same as in (c,d). **i–l**, Same as (a–d), but for projection along y and preimages $d_y = \pm 1$. **m–p**, Same as (e–h), but for projection along y and preimages $d_y = \pm 1$.

$\hat{\mathbf{d}}_0$, at the boundary of a certain volume V. We restrict our studies to textures inside the volume V, which as a result can be identified with S^3, the surface of a four-dimensional ball. Nontrivial mappings $\hat{\mathbf{d}}(\mathbf{r})$ from S^3 to S^2 lead to knotted field configurations characterised by integer topological charges or Hopf invariants [21], Q, as determined by the third homotopy group $\pi_3(S^2) = \mathbb{Z}$. Field configurations with different Hopf invariants cannot be continuously deformed into one another and are therefore topologically distinct.

Taken together, the points in V at which $\hat{\mathbf{d}}$ assumes the same value, $\hat{\mathbf{d}}_{\mathrm{c}}$, define a closed curve known as the preimage of $\hat{\mathbf{d}}_{\mathrm{c}}$. Each of these preimages is linked with all of the others, which are associated with different $\hat{\mathbf{d}}$, exactly Q times. Thus the linking number is equivalent to the Hopf invariant [21], and provides an alternative perspective on its physical significance.

In this experiment we consider the Hopf map [16], which has $Q = 1$ and is generated physically in our system by spin rotations in an inhomogeneous magnetic field. We begin with an optically trapped ^{87}Rb condensate (see Methods) described by the spinor $\xi = (0, 1, 0)^T$, corresponding to $\hat{\mathbf{d}} = \hat{\mathbf{d}}_0 = \hat{\mathbf{z}}$. The inhomogeneous magnetic field is given by

$$\mathbf{B}(\mathbf{r}', t) = b_{\mathrm{q}}(x'\hat{\mathbf{x}} + y'\hat{\mathbf{y}} - z'\hat{\mathbf{z}}) + \mathbf{B}_{\mathrm{b}}(t) \tag{4}$$

where the condensate is taken to be at the origin of the rescaled coordinate system $x' = x$, $y' = y$, and $z' = 2z$. In the gradient $b_{\mathrm{q}} = 4.5$ G/cm and effective bias field $B_z \sim 30$ mG, the zero point of the magnetic field is initially 33 μm away from the centre of the condensate. The creation of the knot begins with a sudden change of $\mathbf{B}_{\mathrm{b}}(t)$ that places the field zero at the centre of the condensate, ideally leaving its state unchanged (see Fig. 1a,b and Extended Data Fig. 1). The nematic vectors then precess about the direction of the local magnetic field at their spatially-dependent Larmor frequencies

$$\omega_{\mathrm{L}}(\mathbf{r}') = \frac{g_{\mathrm{F}}\mu_{\mathrm{B}}|\mathbf{B}(\mathbf{r}', t)|}{\hbar} = \frac{g_{\mathrm{F}}\mu_{\mathrm{B}}b_{\mathrm{q}}r'}{\hbar} \tag{5}$$

where g_{F} is the atomic Landé g-factor, μ_{B} is the Bohr magneton, and $r' = \sqrt{x'^2 + y'^2 + z'^2}$. The optimal result is the time-dependent nematic vector field

$$\hat{\mathbf{d}}(\mathbf{r}') = \exp\left[-i\omega_{\mathrm{L}}(\mathbf{r}')t\,\hat{\mathbf{B}}(\mathbf{r}') \cdot \mathbf{F}\right]\hat{\mathbf{d}}_0 \tag{6}$$

where $\mathbf{F}$ is the vector of dimensionless spin-1 matrices in the Cartesian basis. Importantly, $\hat{\mathbf{d}}(\mathbf{r}') = \hat{\mathbf{d}}_0$ for all points satisfying $\omega_L(\mathbf{r}')t = 2\pi$, and hence we may choose the volume V to be a ball of radius

$$R' = \frac{2\pi\hbar}{g_F\mu_{\mathrm{B}}b_{\mathrm{q}}t}. \tag{7}$$

Figure 1d–e illustrates how the nematic vector assumes its knot soliton configuration as a result of the spatially dependent Larmor precession. The core of the soliton is identified with the preimage of the south pole of S^2, i.e., $\hat{\mathbf{d}}_{\mathrm{core}} = -\hat{\mathbf{d}}_0$, which lies in the $x'y'$-plane. This ring defines a circle (Fig. 1c–e) in which the condensate is entirely in the $m = 0$ spinor component [equation (2)]. The comparable preimage of the north pole, $\hat{\mathbf{d}} = \hat{\mathbf{d}}_0$, includes the z'-axis and all points on the boundary of V. Because antipodal points on S^2 correspond to the same spinor up to a sign [equation (3)], this preimage is also entirely in the $m = 0$ component. The preimages of the equatorial points on the two-sphere consist of linked rings that define a toroidal tube enclosing the core, as shown in Fig. 1c. Since $d_z = 0$ at the equator of S^2, this torus consists of overlapping $m = \pm 1$ components [equation (2)]. Elsewhere, $\hat{\mathbf{d}}$ smoothly interpolates between these values.

After an evolution time T_{evolve} we apply a projection ramp in which the bias field B_z is rapidly changed to move the field zero far from the centre of the condensate [28, 29]. The condensate is then released from the optical trap, whereupon it expands and falls under the influence of gravity. Subsequently, its spinor components are separated and imaged simultaneously along both the vertical (z) and horizontal (y) axes.

The temporal evolution of the particle column densities in the $m = 0$ component, $\int n d_z^2 \, dy$, is shown in Fig. 2a,b. The pictures show the combined preimages of the poles of S^2 ($d_z = \pm 1$), revealing in one picture both the core of the knot and the boundary of V. The preceding analytical result for the radius of the core, $R'/2$ from equation (7), agrees well with the experimental observations.

Figure 3 provides a detailed comparison of the experimentally obtained knot soliton with numerical simulations of the corresponding Gross–Pitaevskii equation (see Methods) with no free parameters. The very good correspondence between the experiment and the simulation, together with the qualitatively correct behaviour of the $m = \pm 1$ spinor components that jointly accumulate in the vicinity of the intensity minima of the $m = 0$ component, provide further evidence that the observed texture is that of a knot soliton. Note that the $m = \pm 1$ components do not overlap as a result of the time-of-flight imaging technique (see Extended Data Fig. 2 for simulated images of the spinor components prior to expansion).

By definition the nematic vector is aligned with the local spin quantization axis, along which the condensate is fully in the $m = 0$ component [see equation (2)]. Remarkably, a projection ramp taken along an arbitrary axis, η, populates the $m = 0$ component with the preimages of the antipodal points in S^2 corresponding to $d_\eta = \pm 1$. By performing the projection ramp along x and y, for example, we can observe the linked preimages of $d_x = \pm 1$ and $d_y = \pm 1$, respectively, in the $m = 0$ component (Fig. 4). These images explicitly demonstrate the linked rings of the Hopf fibration and provide conclusive evidence of the existence of the knot soliton.

Our observations suggest future experiments on the dynamics, stability, and interactions of knot solitons [19]. Experimental creation of multiply-charged and knotted-core solitons in quantum fields stands as another promising research direction. Furthermore, stabilising the knot soliton against dissipation, a feature associated with textures in the Faddeev–Skyrme model [13, 14], remains an important experimental milestone.

METHODS

Experiment. The condensate initialisation, trapping, and imaging techniques are essentially identical to those of ref. 28. The key technical difference in the present experiments is that we bring the magnetic field zero suddenly into the condensate centre, in contrast to the adiabatic creation ramp in ref. 28. Extended Data Fig. 1 shows the measured temporal evolution of the electric current controlling B_z during its excursion, expressed in units of the magnetic field. We define $t = 0$ to be the moment at which the field zero has traversed 90% of the distance towards its final location at the centre of the condensate. The strength of the quadrupole gradient field is estimated by repeating the knot creation experiment with a small bias field offset applied along the x-axis, which introduces a fringe pattern that winds at a rate proportional to the strength of the gradient.

The crossed-beam optical dipole trap operates at 1064 nm with frequencies $\omega_r \sim 2\pi \times 130$ Hz and $\omega_z \sim 2\pi \times 170$ Hz in the radial and axial directions, respectively. The total number of particles in the condensate at the moment of imaging is typically 2.5×10^5.

Data. The experimentally obtained images of knot solitons shown in this manuscript represent typical results selected from among several hundred successful realisations taken under similar conditions over the course of more than a year. Remarkably, almost identical knot solitons have been created with several minutes of time elapsed between the realisations while not changing the applied control sequences.

Simulation. We theoretically describe the low-temperature dynamics of the condensate using the full three-dimensional spin-1 Gross–Pitaevskii equation

$$i\hbar\partial_t \Psi(\mathbf{r}) = \{h(\mathbf{r}) + n(\mathbf{r})[c_0 + c_2 \mathbf{S}(\mathbf{r}) \cdot \mathbf{F}] - i\Gamma n^2(\mathbf{r})\}\Psi(\mathbf{r}) \tag{8}$$

where we denote the single-particle Hamiltonian by $h(\mathbf{r})$, the spin vector by $\mathbf{S}(\mathbf{r}) = \zeta(\mathbf{r})^\dagger \mathbf{F} \zeta(\mathbf{r})$, and the density–density and spin–spin coupling constants by $c_0 = 4\hbar^2(a_0 + 2a_2)/(3m)$ and $c_2 = 4\hbar^2(a_2 - a_0)/(3m)$, respectively. We employ the literature values for the three-body recombination rate $\Gamma = 2.9 \times \hbar \times 10^{-30}$ cm^6/s, the ^{87}Rb mass $m = 1.443 \times 10^{-25}$ kg, and the s-wave scattering lengths $a_0 = 5.387$ nm and $a_2 = 5.313$ nm. The single-particle Hamiltonian assumes the form $h(\mathbf{r}) = -\hbar^2\nabla^2/(2m) + V_{\rm opt}(\mathbf{r}) + g_{\rm F}\mu_{\rm B}\mathbf{B}(\mathbf{r}, t) \cdot \mathbf{F} + q[\mathbf{B}(\mathbf{r}, t) \cdot \mathbf{F}]^2$, where the strength of the quadratic Zeeman effect is given by $q = 2\pi\hbar \times 2.78$ MHz/T and the optical trapping potential is approximated by $V_{\rm opt}(\mathbf{r}) = m\omega_r^2(x^2 + y^2) + m\omega_z^2 z^2$. The Gross–Pitaevskii equation is integrated using a split-operator method and fast Fourier transforms on a discrete grid of size 8×10^6. The computations are carried out using state-of-the-art graphics processing units. The simulations reproduce the experimental results with no free parameters: Only literature values for constants and independently measured parameters, such as the temporal dependence of the magnetic field, are employed. The magnetic field gradient that is briefly applied to separate the different spinor components during the time-of-flight imaging is not included in the simulations.

[1] Adams, C. C. *The Knot Book* (W. H. Freeman and Co., New York, USA, 1994).

[2] Thomson, W. On vortex atoms. *Proc. Roy. Soc. Edinburgh* **VI**, 197–206 (1867).

[3] Rañada, A. F. & Trueba, J. L. Ball lightning an electromagnetic knot? *Nature* **383**, 32 (1996).

[4] Cruz, M., Turok, N., Vielva, P., Martínez-González, E. & Hobson, M. A cosmic microwave background feature consistent with a cosmic texture. *Science* **318**, 1612–1614 (2007).

[5] Smalyukh, I. I., Lansac, Y., Clark, N. A. & Trivedi, R. P. Three-dimensional structure and multistable optical switching of triple-twisted particle-like excitations in anisotropic fluids. *Nature Mater.* **9**, 139–145 (2009).

[6] Tkalec, U., Ravnik, M., Copar, S., Zumer, S. & Musevic, I. Reconfigurable knots and links in chiral nematic colloids. *Science* **333**, 62–65 (2011).

[7] Seč, D., Čopar, S. & Žumer, S. Topological zoo of free-standing knots in confined chiral nematic fluids. *Nat. Commun.* **5**, 1–7 (2014).

[8] Han, D., Pal, S., Liu, Y. & Yan, H. Folding and cutting DNA into reconfigurable topological nanostructures. *Nature Nanotech.* **5**, 712–717 (2010).

[9] Leach, J., Dennis, M. R., Courtial, J. & Padgett, M. J. Vortex knots in light. *New J. Phys.* **7**, 55 (2005).

[10] Dennis, M. R., King, R. P., Jack, B., O'Holleran, K. & Padgett, M. J. Isolated optical vortex knots. *Nature Phys.* **6**, 118–121 (2010).

[11] Kleckner, D. & Irvine, W. T. M. Creation and dynamics of knotted vortices. *Nature Phys.* **9**, 253–258 (2013).

[12] Kawaguchi, Y., Nitta, M. & Ueda, M. Knots in a spinor Bose-Einstein condensate. *Phys. Rev. Lett.* **100**, 180403 (2008).

[13] Faddeev, L. & Niemi, A. J. Stable knot-like structures in classical field theory. *Nature* **387**, 58–61 (1997).

[14] Battye, R. A. & Sutcliffe, P. M. Knots as stable soliton solutions in a three-dimensional classical field theory. *Phys. Rev. Lett.* **81**, 4798–4801 (1998).

[15] Nakahara, M. *Geometry, Topology and Physics* (Taylor & Francis Group, Boca Raton, 2003).

[16] Hopf, H. Über die Abbildungen der dreidimensionalen Sphäre auf die Kugelfläche. *Mathematische Annalen* **104**, 637–665 (1931).

[17] Urbantke, H. The Hopf fibration—seven times in physics. *J. Geom. Phys.* **46**, 125–150 (2003).

[18] Moore, J. E., Ran, Y. & Wen, X.-G. Topological surface states in three-dimensional magnetic insulators. *Phys. Rev. Lett.* **101**, 186805 (2008).

[19] Hietarinta, J., Jäykkä, J. & Salo, P. Relaxation of twisted vortices in the Faddeev-Skyrme model. *Phys. Lett. A* **321**, 324–329 (2004).

[20] Barenghi, C. F. Knots and unknots in superfluid turbulence. *Milan. J. Math.* **75**, 177–196 (2007).

[21] Manton, N. & Sutcliffe, P. *Topological Solitons* (Cambridge University Press, New York, 2004).

[22] Radu, E. & Volkov, M. S. Stationary ring solitons in field theory — knots and vortons. *Phys. Rep.* **468**, 101–151 (2008).

[23] Rañada, A. F. Knotted solutions of the Maxwell equations in vacuum. *J. Phys. A: Math. Gen.* **23**, L815–L820 (1990).

[24] Denschlag, J. *et al.* Generating solitons by phase engineering of a Bose-Einstein condensate. *Science* **287**, 97–101 (2000).

[25] Burger, S. *et al.* Dark solitons in Bose-Einstein condensates. *Phys. Rev. Lett.* **83**, 5198–5201 (1999).

[26] Vinen, W. F. The detection of single quanta of circulation in liquid helium II. *Proc. R. Soc. A* **260**, 218–236 (1961).

[27] Choi, J.-y. *et al.* Imprinting skyrmion spin textures in spinor Bose-Einstein condensates. *New J. Phys.* **14**, 053013 (2012).

[28] Ray, M. W., Ruokokoski, E., Tiurev, K., Möttönen, M. & Hall, D. S. Observation of isolated monopoles in a quantum field. *Science* **348**, 544–547 (2015).

[29] Ray, M. W., Ruokokoski, E., Kandel, S., Möttönen, M. & Hall, D. S. Observation of Dirac monopoles in a synthetic magnetic field. *Nature* **505**, 657–660 (2014).

Acknowledgements We acknowledge funding by the National Science Foundation (grant PHY–1205822), by the Academy of Finland through its Centres of Excellence Program (grant no. 251748) and grants (nos 135794 and 272806), Finnish Doctoral Programme in Computational Sciences, and the Magnus Ehrnrooth Foundation. CSC - IT Center for Science Ltd. (Project No. ay2090) and Aalto Science-IT project are acknowledged for computational resources. We thank N. Johnson for making public his Hopf fibration code, A. Li for assistance with figures, and W. Lee and S.J. Vickery for experimental assistance.

Author Contributions M.W.R., A.H.G, and D.S.H. developed and conducted the experiments and analysed the data. K.T. and E.R. performed the numerical simulations under the guidance of M.M. who provided the initial suggestions for the experiment. M.M. and D.S.H. developed the analytical interpretation of the $m = 0$ data as preimages. All authors discussed both experimental and theoretical results and commented on the manuscript.

Author Information The authors declare that they have no competing financial interests. Correspondence and requests for materials should be addressed to D.S.H. (dshall@amherst.edu).

***PLEASE NOTE** This is the version originally submitted to the journal and contains some minor typos and errors. The published and corrected version will be posted to arXiv six months after publication in the journal.

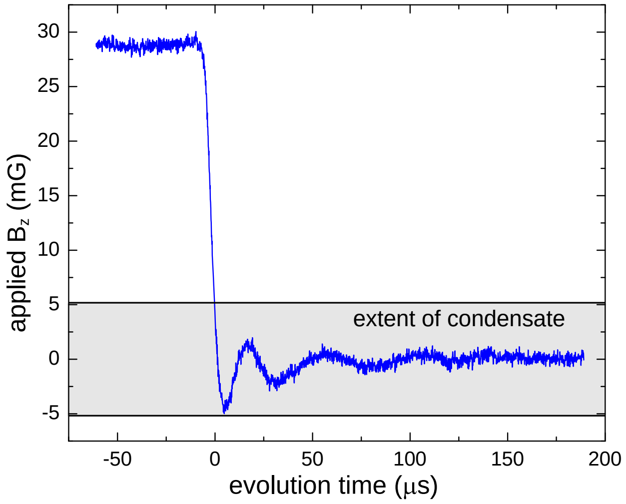

Extended Data Figure 1 | The rapid change to the applied magnetic field. Typical averaged trace of the change in the applied current to the magnetic field coils that initiates the knot creation process. The vertical axis is expressed in terms of B_z using coil calibration data obtained from microwave spectroscopy. Some field contributions from external sources, such as eddy currents, are not included. The grey region shows the effective extent of the condensate as determined by the value of the magnetic field gradient.

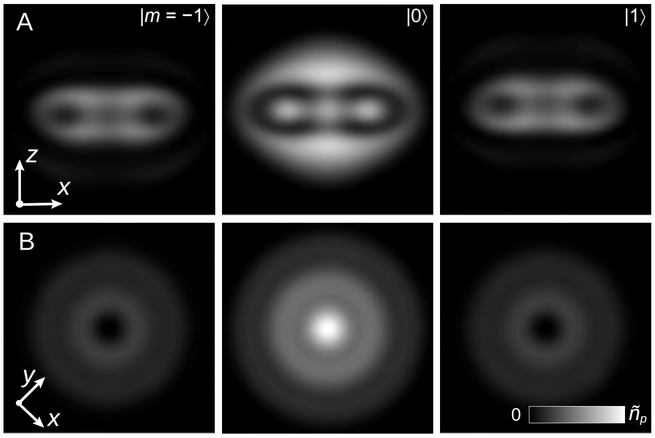

Extended Data Figure 2 | Numerical simulation of the knot creation before expansion. Horizontally (**a**) and vertically (**b**) integrated particle densities of a condensate just before the projection ramp after an evolution time of 557 μs, with matching parameters as in Fig. 3. The field of view is 15 μm × 15 μm in each frame, and the maximum pixel intensity corresponds to $\tilde{n}_p = 3.8 \times 10^{11}$ cm^{-2}.

Summer trainee project 2018, Department of Applied Physics

Research group:	Quantum Computing and Devices (QCD)
Contact person:	Dr. Mikko Möttönen (mikko.mottonen@aalto.fi)
Field of research:	Dilute Bose-Einstein condensates, ultracold quantum gases
Project title:	Magnetic-monopole analogues
Project instructor:	M.Sc. Tuomas Ollikainen, Dr. Mikko Möttönen
Site of research:	Aalto University, QCD Labs, Otaniemi
Website	Click here!
Level of student:	applications from all students are welcome (also for people applying for a Mater's or PhD thesis project)

Introduction

Bose-Einstein condensation is basically a manifestation of macroscopic occupation of a single quantum state. The idea of such a macroscopic occupation dates back to 1924–1925, when Albert Einstein extended the statistical arguments presented by Satyendra Nath Bose to systems consisting of a conserved number of bosonic particles. Einstein recogniced that at sufficiently low temperatures the quantum statistical distribution of an ideal gas of bosons shows *condensation* of a macroscopic fraction of the material into the ground state of the system. This phenomenon, subsequently termed Bose–Einstein condensation (BEC), is a unique, purely quantum mechanical phase transition in the sense that it occurs in principle even in noninteracting bosonic systems. Nowadays BECs are routinely produced in research laboratories around the world and they provide a unique opportunity to study fundamental quantum phenomena.

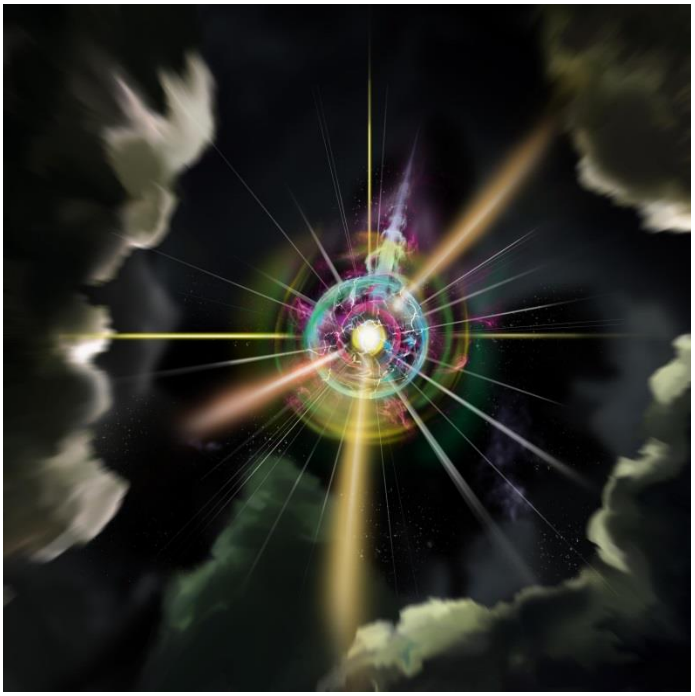

Figure 1. Artistic image of a Dirac monopole in a BEC. (Credit: Heikka Valja)

More than 80 years ago, Paul A. M. Dirac was the first scientist to find a feasible solution for an electron wavefunction in the magnetic field produced by a magnetic monopole. This celebrated result also reveals that electronic charge must be quantized provided that even a single magnetic monopole exists in nature. However, no magnetic monpoles have been convincingly found. Even the experimental observation of the quantum-mechanical structure acquired by the electron wavefunction found by Dirac has been lacking. In fact, there has been no confirmed experimental observations of monopoles in any quantum field prior to our work. In 2014, we published in Nature an article (preprint attached) reporting the first experimental observations of Dirac monopoles in the so-called synthetic magnetic field produced in our spinor BEC. In 2015, we published in Science (article) the first experimental observations of topological point defects, that is, isolated monopoles, in the quantum-mechanical order parameter describing the BEC.

Project goals

Your project is to study novel ways of creation of monopole-like topological defects in BECs.

Research site

Your site of research will be the premises of Quantum Computing and Devices, the so-called QCD Labs, on the Otaniemi campus of Aalto University. There are both theorists and experimentalists working in the group. See the group website (http://physics.aalto.fi/groups/comp/qcd/) for more information.

Instructors

Your main instructor be M.Sc. Tuomas Ollikainen supported by Dr. Mikko Möttönen.

Working methods

Your work will involve building the theoretical understanding of BECs and monopoles. You will also carry out numerical modeling using CUDA.

Thesis possibilities

Depending on your level, this project can be adjusted for a BSc thesis, special assignment, MSc thesis, or a PhD thesis project. Prior knowledge of quantum mechanics and an excellent study record is a prerequisite.

!!CLICK HERE FOR A FREE LINK TO OUR RECENT PAPER ON MONOPOLES IN BECS!!

M. W. Ray et al., Nature **505**, 657 (2014); doi:10.1038/nature12954

Observation of Dirac Monopoles in a Synthetic Magnetic Field

M. W. Ray,[1] E. Ruokokoski,[2] S. Kandel,[1,*] M. Möttönen,[2,3] and D. S. Hall[1]

[1] *Department of Physics, Amherst College,*
Amherst, Massachusetts 01002–5000, USA
[2] *QCD Labs, COMP Centre of Excellence,*
Department of Applied Physics, Aalto University,
P.O. Box 13500, FI–00076 Aalto, Finland
[3] *Low Temperature Laboratory (OVLL), Aalto University,*
P.O. Box 13500, FI-00076 Aalto, Finland

(Dated: 20 September 2013; accepted 4 December 2013)

Abstract

Magnetic monopoles — particles that behave as isolated north or south magnetic poles — have been the subject of speculation since the first detailed observations of magnetism several hundred years ago[1]. Numerous theoretical investigations and hitherto unsuccessful experimental searches[2] have followed Dirac's 1931 development of a theory of monopoles consistent with both quantum mechanics and the gauge invariance of the electromagnetic field[3]. The existence of even a single Dirac magnetic monopole would have far-reaching physical consequences, most famously explaining the quantization of electric charge[3,4]. Although analogues of magnetic monopoles have been found in exotic spin-ices[5,6] and other systems[7–9], there has been no direct experimental observation of Dirac monopoles within a medium described by a quantum field, such as superfluid helium-3 (refs 10–13). Here we demonstrate the controlled creation[14] of Dirac monopoles in the synthetic magnetic field produced by a spinor Bose-Einstein condensate. Monopoles are identified, in both experiments and matching numerical simulations, at the termini of vortex lines within the condensate. By directly imaging such a vortex line, the presence of a monopole may be discerned from the experimental data alone. These real-space images provide conclusive and long-awaited experimental evidence of the existence of Dirac monopoles. Our result provides an unprecedented opportunity to observe and manipulate these quantum-mechanical entities in a controlled environment.

---

[*] Present address: City of Hope, 1500 East Duarte Road, Duarte, California 91010, USA.

Maxwell's equations refer neither to magnetic monopoles nor to the magnetic currents that arise from their motion. Although a simple symmetrisation with respect to the electric and magnetic fields, respectively E and B, leads to equations that involve these magnetic charges, it also seemingly prevents their description in terms of the familiar scalar and vector potentials, respectively V and A, alone. Because the quantum-mechanical Hamiltonian is expressed in terms of potentials, rather than electromagnetic fields, this modification immediately leads to serious theoretical challenges.

In a celebrated paper that combined arguments from quantum mechanics and classical electrodynamics[3], Dirac identified electromagnetic potentials consistent with the existence of magnetic monopoles. His derivation relies upon the observation that in quantum mechanics the potentials V and A influence charged particle dynamics either through the Hamiltonian or, equivalently, through modifications of the complex phase of the particle wavefunction. Armed with these equivalent perspectives, Dirac then considered the phase properties of a wavefunction pierced by a semi-infinite nodal line with nonzero phase winding. He discovered that the corresponding electromagnetic potentials yield the magnetic field of a monopole located at the endpoint of the nodal line. The vector potential A in this case also exhibits a nonphysical line singularity, or 'Dirac string', that terminates at the monopole.

We experimentally create Dirac monopoles in the synthetic electromagnetic field that arises in the context of a ferromagnetic spin-1 ^{87}Rb Bose-Einstein condensate (BEC) in a tailored excited state[14]. The BEC is described by a quantum-mechanical order parameter that satisfies a nonlinear Schrödinger equation, and the synthetic gauge potentials describing a north magnetic pole (Fig. 1) are generated by the spin texture. This experiment builds on studies of synthetic electric and magnetic fields E^* and B^* in atomic BECs, which is an emerging topic of intense interest in the simulation of condensed-matter systems with ultracold atoms[15,16]. Unlike monopole experiments in spin ices[5,6], liquid crystals[7], skyrmion lattices[9], and metallic ferromagnets[8], our experiments demonstrate the essential quantum features of the monopole envisioned by Dirac[3].

Physically, the vector potential, A^*, and synthetic magnetic field, $B^* = \hbar\nabla \times A^*$, are related to the superfluid velocity, v_s, and vorticity, $\Omega = \nabla \times v_s$, respectively. (Here $\hbar$ denotes Planck's constant divided by 2π.) Our primary evidence for the existence of the monopole comes from images of the condensate density taken after the creation of these fields (Figs 2 and 3), which reveal a nodal vortex line with 4π phase winding terminating within the condensate. The images also display a three-dimensional spin structure that agrees well with the results of numerical simulations (Fig. 4). We analyse these findings and discuss their implications below.

The spinor order parameter corresponding to the Dirac monopole[14,17] is generated by an adiabatic spin rotation in response to a time-varying magnetic field, $B(r,t)$. Similar spin rotations have been used to create multiply-quantized vortices[18] and skyrmion spin textures[19]. The order parameter $\Psi(r,t) = \psi(r,t)\zeta(r,t)$ is the product of a scalar order parameter, ψ and a spinor, $\zeta = (\zeta_{+1}, \zeta_0, \zeta_{-1})^{\mathrm{T}} \mathrel{\widehat{=}} |\zeta\rangle$, where $\zeta_m = \langle m|\zeta\rangle$ represents the mth spinor component along z. The condensate is initially spin-polarised along the z axis, that is, $\zeta = (1,0,0)^{\mathrm{T}}$. Following the method introduced in ref. 14, a magnetic field $B(r,t) = b_{\mathrm{q}}(x\hat{x} + y\hat{y} - 2z\hat{z}) + B_z(t)\hat{z}$ is applied, where $b_{\mathrm{q}} > 0$ is the strength of a quadrupole field gradient and $B_z(t)$ is a uniform bias field. The magnetic field zero is initially located on the z axis at $z = B_z(0)/(2b_{\mathrm{q}}) \gg Z$, where Z is the axial Thomas-Fermi radius of the condensate. The spin rotation occurs as B_z is reduced, drawing the magnetic field zero into the region occupied by the superfluid.

Ideally, the condensate spin adiabatically follows the local direction of the field (Fig. 1a–c). Our numerical analysis indicates, and both simulations and experiment confirm, that the fraction of atoms undergoing nonadiabatic spin-flip transitions is of order 1% for our experimental parameters. The spin texture in the adiabatic case is conveniently expressed in a scaled and shifted coordinate system with $x' = x$, $y' = y$, $z' = 2z - B_z/b_{\mathrm{q}}$, corresponding derivatives ∇', and spherical coordinates (r', θ', φ'). This transformation scales the z axis by a factor of two and shifts the origin of coordinates to coincide with the magnetic field zero. The applied magnetic field is then $B = b_{\mathrm{q}}(x'\hat{x}' + y'\hat{y}' - z'\hat{z}')$. As B_z is reduced, each spin rotates by an angle $\pi - \theta'$ about an axis defined by the unit vector $\hat{n}(r', \theta', \varphi') = -\hat{x}' \sin\varphi' + \hat{y}' \cos\varphi'$. This spatially-dependent rotation leads to a superfluid velocity

$$v_s = \frac{\hbar}{Mr'} \frac{1 + \cos\theta'}{\sin\theta'} \hat{\varphi}' \tag{1}$$

and vorticity

$$\Omega = -\frac{\hbar}{Mr'^2}\hat{r'} + \frac{4\pi\hbar}{M}\delta(x')\delta(y')\Theta(z')\hat{r'} \tag{2}$$

where M is the atomic mass, δ is the Dirac delta function and Θ is the Heaviside step function. The vorticity is that of a monopole attached to a semi-infinite vortex line singularity, of phase winding 4π, extending along the positive z' axis.

The synthetic vector potential arising from the spin rotation can be written as $A^* = -Mv_s/\hbar$, with the line singularity in A^* coincident with the nodal line in $\mathit{\Psi}$. However, this singularity is nonphysical, as it depends on the choice of gauge and can even be made to vanish[20] (Supplementary Information). The synthetic magnetic field of the monopole is therefore simply

$$B^* = \frac{\hbar}{r'^2}\,\hat{r}' \tag{3}$$

The fields v_s and B^* are depicted in Fig. 1d.

The experimental setup[21] is shown schematically in Fig. 1**e**. The optically-trapped ^{87}Rb BEC consists of $N = 1.8(2) \times 10^5$ atoms in the $|F{=}1, m{=}1\rangle \equiv |1\rangle$ spin state, where the uncertainty reflects shot-to-shot variations and the calibration of the detection system. The calculated radial and axial Thomas-Fermi radii are $R = 6.5\,\mu$m and $Z = 4.6\,\mu$m, respectively, and the corresponding optical trap frequencies are respectively $\omega_4 \approx 2\pi \times 160$ Hz and $\omega_z \approx 2\pi \times 220$ Hz. Four sets of coils are used to produce b_q, B_z and the transverse magnetic field components B_x and B_y, which are used to guide the applied magnetic field zero into the condensate. At the beginning of the monopole creation process, the bias field is $B_z =$ 10 mG. The quadrupole field gradient is then linearly ramped from zero to $b_\mathrm{q} = 3.7$ G/cm, placing the magnetic field zero approximately 30 μm above the condensate. The field zero is then brought down into the condensate by decreasing B_z linearly to $B_{z,\mathrm{f}}$ at the rate $\dot{B}_z = -0.25$ G/s. We call this the creation ramp.

The atomic density of each spinor component $|m\rangle$ is imaged as established by the local spin rotation during the creation ramp (Methods). As the field zero passes through the condensate (Fig. 2a–f), the distribution of particles in the three spin states changes in a manner indicative of the expected spin rotation shown in Fig. 1. The nodal line appears in the images taken along the vertical axis as holes in the $|-1\rangle$ and $|0\rangle$ components, and in the side images as regions of reduced density extending vertically from the top of the condensate towards, but not through, the $|1\rangle$ component. This nodal line extends more deeply into the condensate as $B_{z,\mathrm{f}}$ is reduced. Ultimately it splits into two vortex lines (Fig. 2f; see also Extended Data Fig. 1) — the characteristic signature of the decay of a doubly-quantized vortex[22] — illustrating its 4π phase winding.

We compare the experimental images of the vertically (Fig. 3a) and horizontally (Fig. 3c) imaged density profiles to those given by numerical simulations (Fig. 3b,d) in which the monopole is near the centre of the condensate. The simulation data are obtained by solving the full three-dimensional dynamics of the spinor order parameter (Methods). The locations of the doubly-quantized and singly-quantized vortices in spinor components $|-1\rangle$ and $|0\rangle$ are clearly visible in the experimentally acquired density profiles, as are other structures discernible in the images obtained from the numerical simulations. The observed vertical spatial separation of the spinor components, (Fig. 3c) confirms that the vortex line terminates within the bulk of the condensate.

The quantitative agreement between experiment and simulation is apparent in Fig. 4, which shows cross-sections of the density profiles taken through the centre of the condensate. The differences observed in the peak densities (Fig. 4a) of experimental (solid lines) and simulated (dashed lines) data are due to effects not taken into account in the simulation, such as three body losses that were observed to be $\sim 10\%$ in the experiment. To show their effect we have scaled the simulated data accordingly (dotted lines). Noting the absence of free parameters, the experimental data are in very good agreement with the numerical simulation.

We also show the fraction of the condensate in each spinor component for different vertical monopole locations within the condensate (Fig. 4b), including data from images in which the nodal line of the order parameter does not necessarily coincide with the z axis. The physical observable is the position of the centre of mass of the $|0\rangle$ component, z_0, relative to the centre of mass of the whole condensate, z_c. Again, we find the experiments and simulations are in very good quantitative agreement without any free parameters.

An alternative description of the origins of the velocity and vorticity profiles (equations (1) and (2)) can be presented in terms of the motion of the monopole (Supplementary Information). As the monopole approaches the condensate, it is a source not only of the synthetic magnetic field B^* (equation (3)) but also of an azimuthal synthetic electric field, E^*, described by Faraday's law, $\nabla' \times E^* = -\partial B^*/\partial t$. Each mass element of the superfluid is given a corresponding azimuthal acceleration by E^*. The monopole motion thereby induces the appropriate superfluid velocity and vorticity profiles within the condensate, in a manner similar to the induction of electric current in a superconducting loop by the motion of a (natural) magnetic monopole[23]. In our case, the condensate itself is the monopole detector, analogous to the superconducting loop. Being three-dimensional, however, it is sensitive to the entire 4π solid angle surrounding the monopole.

The creation and manipulation of a Dirac monopole in a controlled environment opens up a wide range of experimental and theoretical investigations. The time evolution and decay[14] of the monopole are of particular interest because it is not created in the ground state[24]. Interactions between the monopole and other topological excitations, such as vortices, present another fundamental research avenue with a variety of unexplored phenomena. There exists also the possibility of identifying and studying condensate spin textures that correspond to other exotic synthetic electromagnetic fields, such as that of the non-Abelian monopole[25]. Finally, the experimental methods developed in this work can also be directly used in the realization of a vortex pump[26], which paves the way for the study of peculiar many-body quantum states, such as those related to the quantum Hall effect[27].

Note added. The effects of the Lorentz force arising from an inhomogeneous synthetic magnetic field have recently been observed in condensate dynamics[28].

METHODS SUMMARY

Imaging. After the creation ramp, we non-adiabatically change B_z from $B_{z,\mathrm{f}}$ to a large value (typically several hundred milligauss) in order to project the condensate spin components $\{|m\rangle\}$ into the approximate eigenstates of the Zeeman Hamiltonian while preserving the monopole spin texture. We call this the 'projection ramp'. The condensate is then released from the trap and allowed to expand for 22.9 ms. The three spin states are separated along the x axis during the expansion by a 3.5 ms pulse of the magnetic field gradient with the magnetic bias field pointing in the x direction. We take images simultaneously along the horizontal and vertical axes.

Data. The images shown in Figs 2 and 3 are selected from among several dozen similar images taken under identical conditions, and hundreds of similar images taken under similar conditions (see also Extended Data Fig. 2 for representative examples). Not every experimental run yields an image of a monopole, because drifts in the magnetic field and location of the optical trap cause the magnetic field zero to pass outside the BEC. Under optimal conditions, 5–10 consecutive images may be taken before drifts require adjustment of the bias fields.

Simulation. We solve the full three-dimensional Gross–Pitaevskii equation with simulation parameters chosen to match those of the experiment, excepting the effects of three-body losses and the magnetic forces arising from the gradient during the spin component separation just before imaging. To show the effects of the expansion, we present integrated particle densities of the condensate from the numerical simulation immediately after the creation ramp, and while the magnetic field zero is still in the condensate, in Extended Data Fig. 3. The volume considered varies from $20 \times 20 \times 20\, a_r^3$ to $320 \times 320 \times 320\, a_r^3$, where $a_r = \sqrt{\hbar/(M\omega_r)} \approx 0.9$ μm is the radial harmonic oscillator length. The size of the computational grid changes from $180 \times 180 \times 180$ to $1,024 \times 1,024 \times 1,024$ points.

---

[1] Goldhaber, A. S. & Trower, W. P. (eds.) *Magnetic Monopoles* (American Association of Physics Teachers, Berwyn Park, Maryland, 1990).

[2] Milton, K. A. Theoretical and experimental status of magnetic monopoles. *Rep. Prog. Phys.* **69**, 1637–1711 (2006).

[3] Dirac, P. A. M. Quantised singularities in the electromagnetic field. *Proc. R. Soc. Lond. A* **133**, 60–72 (1931).

[4] Vilenkin, A. & Shellard, E. P. S. (eds.) *Cosmic Strings and Other Topological Defects* (Cambridge University Press, Cambridge, England, 1994).

[5] Castelnovo, C., Moessner, R. & Sondhi, S. L. Magnetic monopoles in spin ice. *Nature* **451**, 42–45 (2008).

[6] Morris, D. J. P. *et al.* Dirac strings and magnetic monopoles in the spin ice $Dy_2Ti_2O_7$. *Science* **326**, 411–414 (2009).

[7] Chuang, I., Durrer, R., Turok, N. & Yurke, B. Cosmology in the laboratory: Defect dynamics in liquid crystals. *Science* **251**, 1336–1342 (1991).

[8] Fang, Z. *et al.* The anomalous Hall effect and magnetic monopoles in momentum space. *Science* **302**, 92–95 (2003).

[9] Milde, P. *et al.* Unwinding of a skyrmion lattice by magnetic monopoles. *Science* **340**, 1076–1080 (2013).

[10] Blaha, S. Quantization rules for point singularities in superfluid ^{3}He and liquid crystals. *Phys. Rev. Lett.* **36**, 874–876 (1976).

[11] Volovik, G. & Mineev, V. P. Vortices with free ends in superfluid He^3-a. *JETP Letters* **23**, 647–649 (1976).

[12] Salomaa, M. M. Monopoles in the rotating superfluid helium-3 A–B interface. *Nature* **326**, 367

(1987).

[13] Volovik, G. *The Universe in a Helium Droplet* (Oxford University Press, 2003).

[14] Pietilä, V. & Möttönen, M. Creation of Dirac monopoles in spinor Bose-Einstein condensates. *Phys. Rev. Lett.* **103**, 030401 (2009).

[15] Lin, Y.-J., Compton, R. L., Jiménez-Garcia, K., Porto, J. V. & Spielman, I. B. Synthetic magnetic fields for ultracold neutral atoms. *Nature* **462**, 628–631 (2009).

[16] Dalibard, J., Gerbier, F., Juzeliūnas, G. & Öhberg, P. *Colloquium* : Artificial gauge potentials for neutral atoms. *Rev. Mod. Phys.* **83**, 1523–1543 (2011).

[17] Savage, C. M. & Ruostekoski, J. Dirac monopoles and dipoles in ferromagnetic spinor Bose-Einstein condensates. *Phys. Rev. A* **68**, 043604 (2003).

[18] Leanhardt, A. E. *et al.* Imprinting vortices in a Bose-Einstein condensate using topological phases. *Phys. Rev. Lett.* **89**, 190403 (2002).

[19] Choi, J.-y., Kwon, W. J. & Shin, Y.-i. Observation of topologically stable 2D skyrmions in an antiferromagnetic spinor Bose-Einstein condensate. *Phys. Rev. Lett.* **108**, 035301 (2012).

[20] Wu, T. T. & Yang, C. N. Concept of nonintegrable phase factors and global formulation of gauge fields. *Phys. Rev. D* **12**, 3845–3857 (1975).

[21] Kaufman, A. M. *et al.* Radio-frequency dressing of multiple Feshbach resonances. *Phys. Rev. A* **80**, 050701 (2009).

[22] Shin, Y. *et al.* Dynamical instability of a doubly quantized vortex in a Bose-Einstein condensate. *Phys. Rev. Lett.* **93**, 160406 (2004).

[23] Cabrera, B. First results from a superconductive detector for moving magnetic monopoles. *Phys. Rev. Lett.* **48**, 1378–1381 (1982).

[24] Ruokokoski, E., Pietilä, V. & Möttönen, M. Ground-state Dirac monopole. *Phys. Rev. A* **84**, 063627 (2011).

[25] Pietilä, V. & Möttönen, M. Non-Abelian magnetic monopole in a Bose-Einstein condensate. *Phys. Rev. Lett.* **102**, 080403 (2009).

[26] Möttönen, M., Pietilä, V. & Virtanen, S. M. M. Vortex pump for dilute Bose-Einstein condensates. *Phys. Rev. Lett.* **99**, 250406 (2007).

[27] Roncaglia, M., Rizzi, M. & Dalibard, J. From rotating atomic rings to quantum Hall states. *Sci. Rep.* **1**, 43 (2011).

[28] Choi, J.-y., Kang, S., Seo, S. W., Kwon, W. J. & Shin, Y.-i. Observation of a geometric Hall

effect in a spinor Bose-Einstein condensate with a skyrmion spin texture. *Phys. Rev. Lett.* **111**, 245301 (2013).

[29] Carroll, G. E. & Hioe, F. T. Further generalization of Landau-Zener calculation. *J. Opt. Soc. Am. B* **2**, 1355–1360 (1985).

Supplementary Information is available online.

Acknowledgements We acknowledge funding by the National Science Foundation (grants PHY–0855475 and PHY–1205822), by the Academy of Finland through its Centres of Excellence Program (grant no. 251748) and grants (nos 135794, 272806, and 141015), and ny Finnish Doctoral Programme in Computational Sciences. CSC - IT Center for Science Ltd. is acknowledged for computational resources (Project No. ay2090). We thank G. Volovik, M. Krusius, R. H. Romer, M. Nakahara, and J. R. Friedman for their comments on the manuscript. We also thank Heikka Valja for his artistic input. M.W.R. and D.S.H. acknowledge discussions with R. P. Anderson, K. Jagannathan, and experimental assistance from N. B. Bern.

Author Contributions M.W.R., S.K., and D.S.H. developed and conducted the experiments, after which M.W.R. and D.S.H. analysed the data. E.R. performed the numerical simulations under the guidance of M.M., who also developed the gauge transformations presented in Supplementary Material. Interactive feedback between the experiments and simulations carried out by M.W.R., D.S.H., E.R., and M.M. was essential to achieving the reported results. All authors discussed both experimental and theoretical results and commented on the manuscript.

Author Information Reprints and permissions information is available at `www.nature.com/reprints`. The authors declare that they have no competing financial interests. Correspondence and requests for materials should be addressed to D.S.H. (dshall@amherst.edu).

METHODS

Condensate Production. Condensates are produced in the $|F{=}2, m{=}2\rangle$ spin state of ^{87}Rb by sequential steps of evaporative cooling, first in a time-averaged, orbiting potential (TOP) magnetic trap and subsequently in a $1,064$ nm crossed-beam optical dipole trap. The two evaporation stages are used to avoid the introduction of vortices that occasionally arise during the transfer of a condensate from the magnetic trap to the optical trap. The radial and axial optical trap frequencies at the end of the evaporative cooling process are ~ 110 Hz and ~ 130 Hz, respectively. A subsequent microwave Landau–Zener sweep drives the condensate into the $|F{=}1, m{=}1\rangle$ state.

After having established $B_z = 10$ mG, the trap frequencies are increased to $(\omega_r, \omega_z) \approx 2\pi \times (160, 220)$ Hz before the quadrupole field is turned on. The tighter trap better resists the magnetic forces exerted by the field gradient, but it also limits the condensate lifetime to approximately 500 ms as a result of three-body loss processes. At the end of the experiment $N \approx 1.6 \times 10^5$, indicating typical three-body losses of $\sim 10\%$.

Magnetic Field Control. The x, y, and z axes are defined by the orientation of the magnetic field coils BX, BY and BZ, as shown in Fig. 1e. The magnetic fields are calibrated to within ~ 1 mG using Majorana spectroscopy, in which the field component along the z axis is rapidly (15 G s^{-1}) reversed and the fraction of atoms thereby transferred non-adiabatically to the $|-1\rangle$ state is measured as a function of the currents applied to the BX and BY field coils. Maximum transfer occurs when the transverse field components are minimised. The field along the z axis is similarly calibrated by rapidly reversing the field component along the x axis.

Precise magnetic field control at the location of the condensate is one of the most challenging aspects of the experiment. The condensate presents a small target (≈ 7 μm) into which the field zero must be guided. The creation process is therefore quite sensitive to drifts in the relative position of the optical trap and the position of the field zero, limiting our ability to generate large sequential data sets without compensatory adjustments. Such drifts may be caused either by fluctuating background fields or by mechanical instabilities in the trapping beam optics. With $b_\mathrm{q} = 3.7$ G cm^{-1}, a 1-mG change in the radial field corresponds to a translation of the zero by 1.4 μm, or 25% of the condensate radius — enough to disturb the creation of the monopole. Similar shifts alter the vertical bias field required to bring the field zero into the condensate.

An additional complication is that the centre of the optical trap and the physical centre of the gradient coils do not in general coincide, and can drift with respect to one another. The condensate can be offset horizontally by as much as 14 μm, and vertically up to ≈ 25 μm below, the centre of the gradient coils.

Adiabatic Spin Rotation. As B_z changes during the monopole creation process, the condensate spin ideally remains in the strong-field seeking state (SFSS), that is, the minimum-energy eigenstate of the local Zeeman Hamiltonian. At the field zero, however, the local Zeeman term of the Hamiltonian vanishes and non-adiabatic spin transitions to the neutral and weak-field seeking states become inevitable. Neglecting the kinetic-energy related to spin rotations and the weak spin–spin interactions in the condensate, the spatially-dependent probability of successful adiabatic spin rotation when the homogeneous bias field is inverted from large positive values to large negative values, can be approximated within the three-level Landau–Zener model by[29]

$$\Pi_{\mathrm{ad}}(x,y) = \left\{ 1 - \exp\left[-\frac{\pi \mu_B b_{\mathrm{q}}^2 (x^2+y^2)}{4\hbar |\dot{B}_z|} \right] \right\}^2 \tag{4}$$

where μ_B is the Bohr magneton. The fraction of particles remaining in the SFSS can be approximated by an average of equation (4) weighted by a fixed particle density $\bar{n}(\mathbf{r})$ as

$$P_{\mathrm{ad}} = \frac{\int \bar{n}(\mathbf{r}) \Pi_{\mathrm{ad}}(\mathbf{r}) \mathrm{d}\mathbf{r}}{\int \bar{n}(\mathbf{r}) \mathrm{d}\mathbf{r}} \tag{5}$$

Applying equations (4) and (5) to the initial vortex-free density distribution determined by solving the Gross–Pitaevskii equation with the parameter values extracted from the experiments, we obtain $P_{\mathrm{ad}} = 98\%$. The doubly-quantized vortex generated during the field inversion reduces the number of atoms in precisely the region where the undesired spin flips are most probable. For a density distribution that includes the doubly quantized vortex along the z axis, equations (4) and (5) yield $P_{\mathrm{ad}} = 99\%$. Full numerical simulations of the creation of the doubly quantized vortex confirm that 99% of the particles remain in the SFSS.

Experimentally, P_{ad} is controlled by b_{q} and $\dot{B}_z$. Increasing b_{q} results in stronger magnetic forces on the condensate due to the gradient, which must remain small relative to those exerted by the optical trap so as not to perturb the condensate position extensively. The strength of the optical trap, however, cannot itself be increased without compromising both the size of the condensate and its lifetime. Choosing $b_{\mathrm{q}} = 3.7$ G cm^{-1} was found convenient in this respect.

Decreasing $\dot{B}_z$, on the other hand, results in lengthier exposures of the BEC to magnetic field noise that can possibly induce undesirable spin transitions. The noise associated with the power mains (at frequencies that are odd integer n multiples of 60 Hz) is the most serious, being resonant at a field of $n \times 85$ μG. The choice $\dot{B}_z = -0.25$ G/s ensures that the resonance condition is passed faster than a single oscillation period of the noise at least up to $n = 7$. The effect of this noise is merely to distort the path traced by the field zero slightly during the creation ramp.

With the experimental parameters described above, we find that a negligible number of atoms is excited out of the SFSS after the field zero is moved fully through the condensate. Only when we increase the ramp rates by an order of magnitude do we find a discernible fraction of the atoms in the weak-field seeking state. This is consistent with the simulations and the calculation of P_{ad}. We conclude that non-adiabatic spin flips are not important in the monopole creation process with the parameters employed in the experiments, and that the Landau–Zener model describes this phenomenon well.

Imaging. At the end of the creation ramp, B_z is rapidly decreased (in 0.040 ms) until $|B_z/B_{z,\mathrm{f}}| \gg 1$, a stage we call the 'projection ramp'. This non-adiabatic field ramp keeps the order parameter essentially unchanged but takes the spin states $\{|m\rangle\}$ to be the approximate eigenstates of the Zeeman Hamiltonian. As described below, we image the particle density in each of these new eigenstates, accessing the detailed structure of the monopole established by the creation ramp.

Immediately after the projection ramp, the magnetic field gradient is turned off in 0.350 ms. The optical trapping beams are then extinguished, releasing the condensate from the trap and permitting it to expand freely for 4 ms. The field is then increased adiabatically (in 1 ms) to 13.7 G in the x-direction as B_z is simultaneously reduced to zero. After a 1.5 ms delay, the magnetic gradient coils are pulsed on for 3.5 ms to 20.1 G cm^{-1} (radial) to separate the spin states horizontally.

The total time of flight of the atoms is 22.9 ms, counted from the moment of release from the optical trap. After expansion, the condensates are imaged absorptively along both the vertical (z) and horizontal (y) axes simultaneously (to within 14 μs) in the presence of a 0.1-G imaging field directed along z. In the absorption images we correct for neither the slightly different sensitivities of the different spin states to the probe beam nor the slightly different expansions that result from the applied magnetic field gradient.

Although we describe in this paper the creation of the monopole with the initial parameters $b_{\mathrm{q}} > 0$, $B_z(t = 0) > 0$ and $\dot{B}_z < 0$, the process yields essentially identical results experimentally when $b_{\mathrm{q}} > 0$, $B_z(t = 0) < 0$, and $\dot{B}_z > 0$ in the creation ramp, except that the field zero enters the condensate along the negative z axis and thereby changes the sense of the spin rotation. Similarly, B_z can be rapidly increased in either the $+z$ or $-z$ directions in the projection ramp with the same outcomes (Extended Data Fig. 2).

The images shown in Figs 2 and 3 are selected from among dozens of similar images taken under identical conditions, and hundreds of images taken under similar conditions (Extended Data Fig. 2). Not every image demonstrates the signature presence of a monopole, because drifts in the magnetic fields and the location of the optical trap eventually cause the magnetic field zero to miss the condensate. Under optimal conditions we find that we can take five to ten sequential images in which the field zero passes through the condensate, after which we must adjust the magnetic bias fields to re-centre the magnetic field zero on the condensate.

The first images of pairs of singly-quantized vortices that indicate the passage of the monopole through the condensate were taken on February 6, 2013. Consistent images of the condensate density distributions associated with the monopole were first obtained on March 1, 2013.

Numerical Simulation. The experimental setup is simulated by solving the full three-dimensional Gross–Pitaevskii equation. The simulation parameters are chosen to match those of the experiment, but we include neither the effects of three-body losses nor the magnetic forces arising from the gradient during the spin component separation just before imaging. The particle number is held fixed at $N = 1.8 \times 10^5$ corresponding to the initial number of atoms in the experiment. We can roughly account for the three-body losses by scaling the obtained particle density by the fraction of atoms that remain at the end of the experiment. Otherwise, the simulations are performed with the time-dependent parameters identical to those used in the experiment.

The volume considered varies from $20 \times 20 \times 20\, a_r^3$ to $320 \times 320 \times 320\, a_r^3$, where $a_r = \sqrt{\hbar/(M\omega_r)} \approx 0.9\ \mu$m is the radial harmonic oscillator length. The size of the computational grid changes from $180 \times 180 \times 180$ to $1,024 \times 1,024 \times 1,024$ points. The initial spin-polarised state is obtained with a relaxation method and the temporal evolution is computed using a split-operator technique employing Fourier transforms for the kinetic-energy part. The time required for the computation is reduced with the help of graphics processing units, coordinate transformations and an adaptive computational grid.

Effects of free expansion. The condensate must be allowed to expand freely in order to image its spin structure and determine the presence of the monopole. The condensate is therefore not imaged while the magnetic field zero is within the condensate. To demonstrate the effects of the free expansion on the spin structure, we show the simulated particle densities of the condensate just after the creation ramp in Extended Data Fig. 3. The images are created from an intermediate step in the complete simulation that is used to produce Fig. 2. The principal effects of the release of the condensate are to cause it to expand with different speeds in different directions, to increase the relative vortex core sizes, to partially fill the vortex cores with other spin components, and the slight separation of the different spinor components. The last three effects are due exclusively to the repulsive interactions between the atoms during the first few milliseconds of expansion. Because there is excellent agreement between the simulated and experimentally observed results in Fig. 3, we conclude that Extended Data Fig. 3 is a suitable representation of the condensate just after the creation ramp, while the field zero is still within the superfluid.

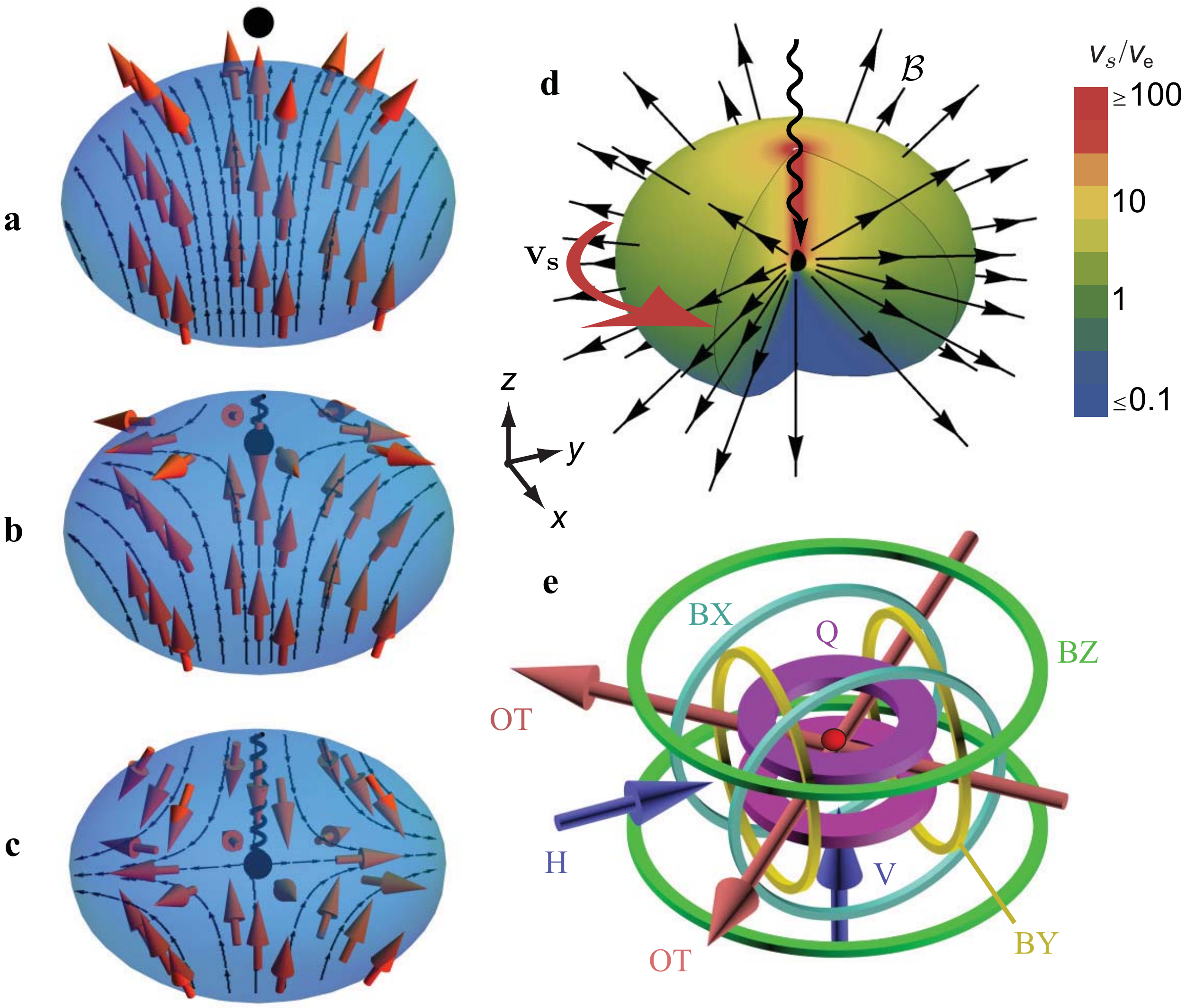

Figure 1 | Schematic representations of the monopole creation process and experimental apparatus. **a-c**, Theoretical spin orientation (red arrows) within the condensate when the magnetic field zero (black dot) is above (**a**), entering (**b**) and in the middle of (**c**) the condensate. The helix represents the singularity in the vorticity. **d**, Azimuthal superfluid velocity v_s (colour scale and red arrow), scaled by equatorial velocity v_e. Black arrows depict the synthetic magnetic field, B^*. **e**, Experimental setup showing magnetic quadrupole (Q) and bias field (BX, BY and BZ) coils. Red arrows (OT) show beam paths of the optical dipole trap, and blue arrows indicate horizontal (H) and vertical (V) imaging axes. Gravity points in the $-z$ direction.

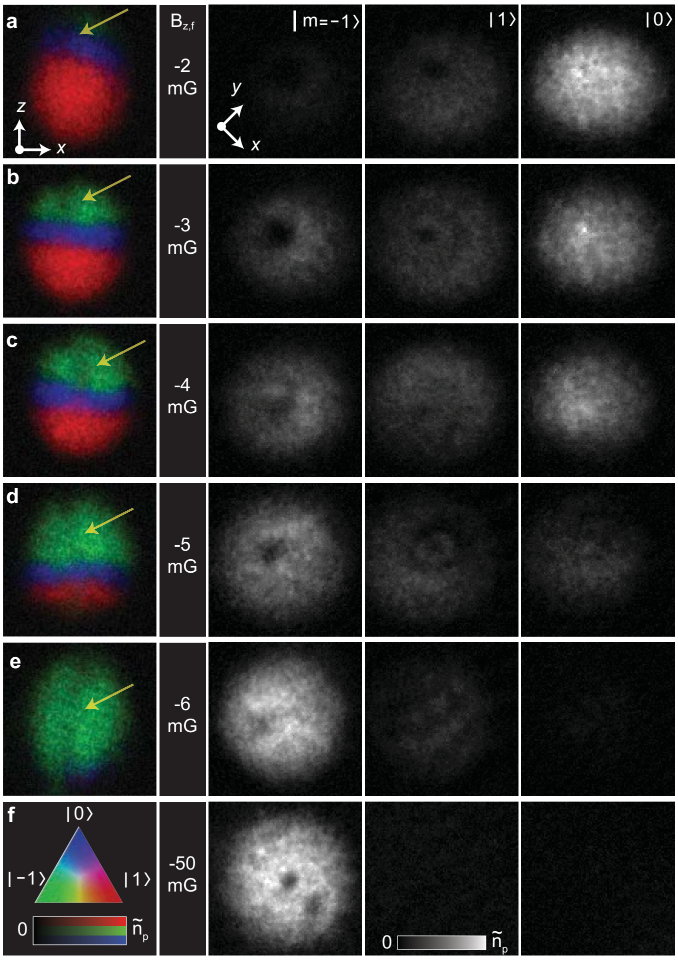

Figure 2 | Experimental creation of Dirac monopoles. Images of the condensate showing the integrated particle densities in different spin components as $B_{z,\mathrm{f}}$ is decreased. Each row contains images of an individual condensate. The leftmost column shows colour composite images of the column densities taken along the horizontal axis for the three spin states $\{|1\rangle, |0\rangle, |\quad 1\rangle\}$; the colour map is given in **f**. Yellow arrows indicate the location of the nodal lines. The right three columns show images taken along the vertical axis. The scale is 285 μm $\times$ 285 μm (horizontal) and 220 μm $\times$ 220 μm (vertical), and the peak column density is $\tilde{n}_p = 1.0 \times 10^9$ cm $^{\quad 2}$.

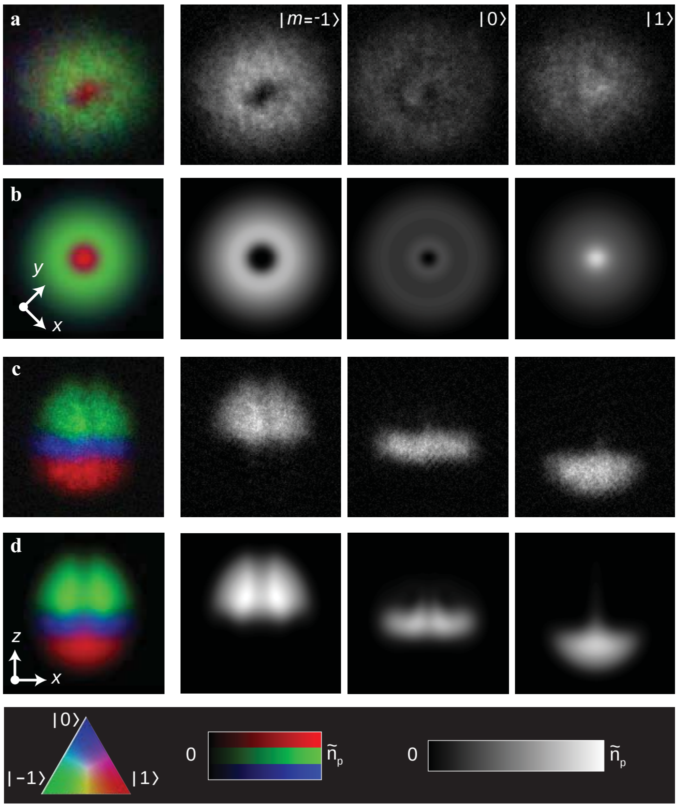

Figure 3 | Comparison between experiment and simulation. Experimental (**a,c**) and simulated (**b,d**) condensate particle densities with the monopole near the centre of the condensate. Comparisons along the vertical axis are shown in rows **a** and **b**, while those along the horizontal axis are shown in rows **c** and **d**. The hole observed in the $|-1\rangle$ component (row **a**) is discernible as a line of diminished density in row **c**. The field of view is 220 μm × 220 μm in **a** and **b** and 285 μm × 285 μm in **c** and **d**. The colour composite images and peak density n_p are as in Fig. 2.

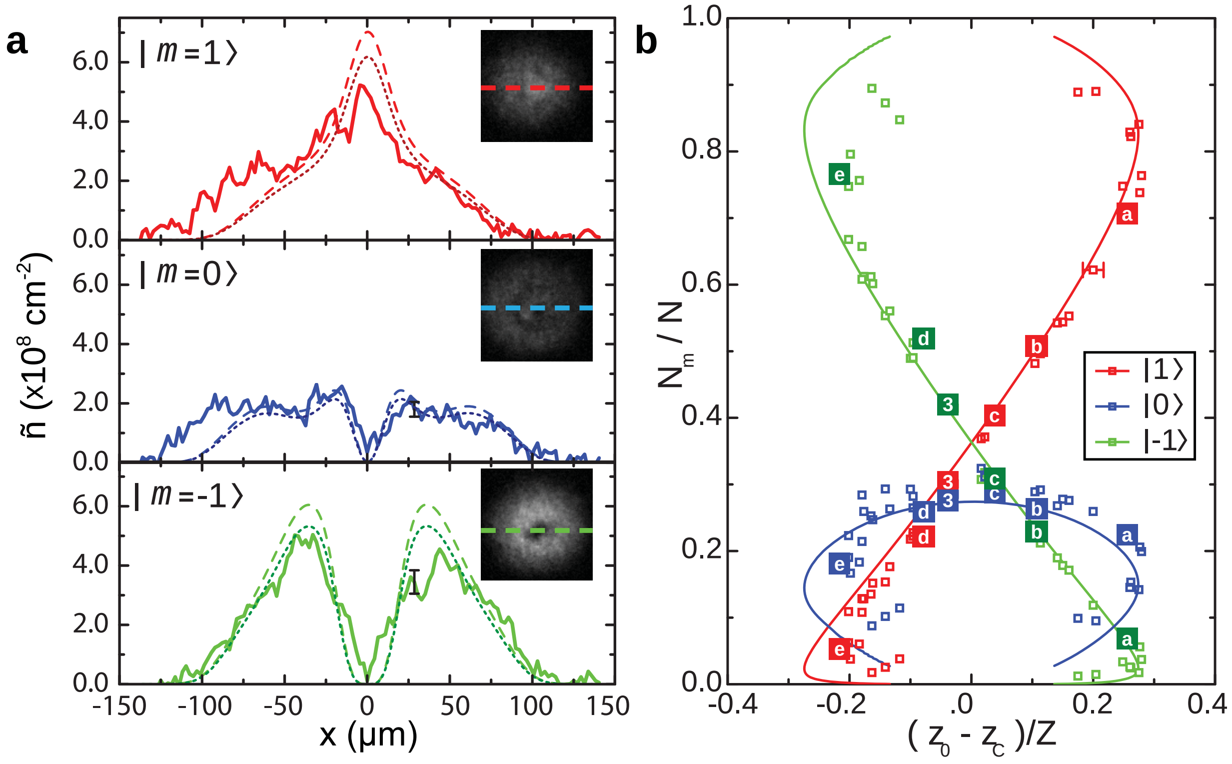

Figure 4 | Quantitative comparison between experiment and simulation. **a**, Experimental (solid lines) and simulated (dashed and dotted lines) column densities $\tilde{n}$ of the condensate from the vertical images in Fig. 3, with cross-sections taken as shown in the insets. Dotted lines show the approximate effect of three-body losses (see text). The origin $x = 0$ coincides with the hole in state $|0\rangle$. **b**, Fractions in each spin state for different positions of the centre of mass of the $|0\rangle$ state (z_0) relative to that of the condensate (z_c) in units of the axial Thomas-Fermi radius (Z). Solid lines are simulated values and points marked with letters and numbers correspond to panels **a-e** of Figs 2 and 3, respectively. Typical error bars that reflect uncertainties in the calibration of the imaging system are shown for several points.

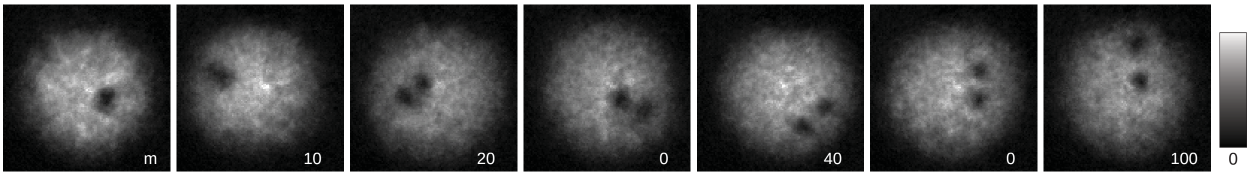

Extended Data Figure 1 | Decay of the doubly-quantized vortex. Images of the condensate time-evolution after moving the magnetic field zero completely through the condensate. The evolution time is shown at the bottom right of each panel. The maximum pixel intensity corresponds to a peak column density $\tilde{n}_p = 1.0 \times 10^9$ cm^{-2}, and the field of view is 246 μm × 246 μm. Each image represents a separate condensate, and $\dot{B}_z = 3$ G s^{-1}. After roughly 10 ms the vortex splits in two, demonstrating the initial 4π phase winding of the nodal line.

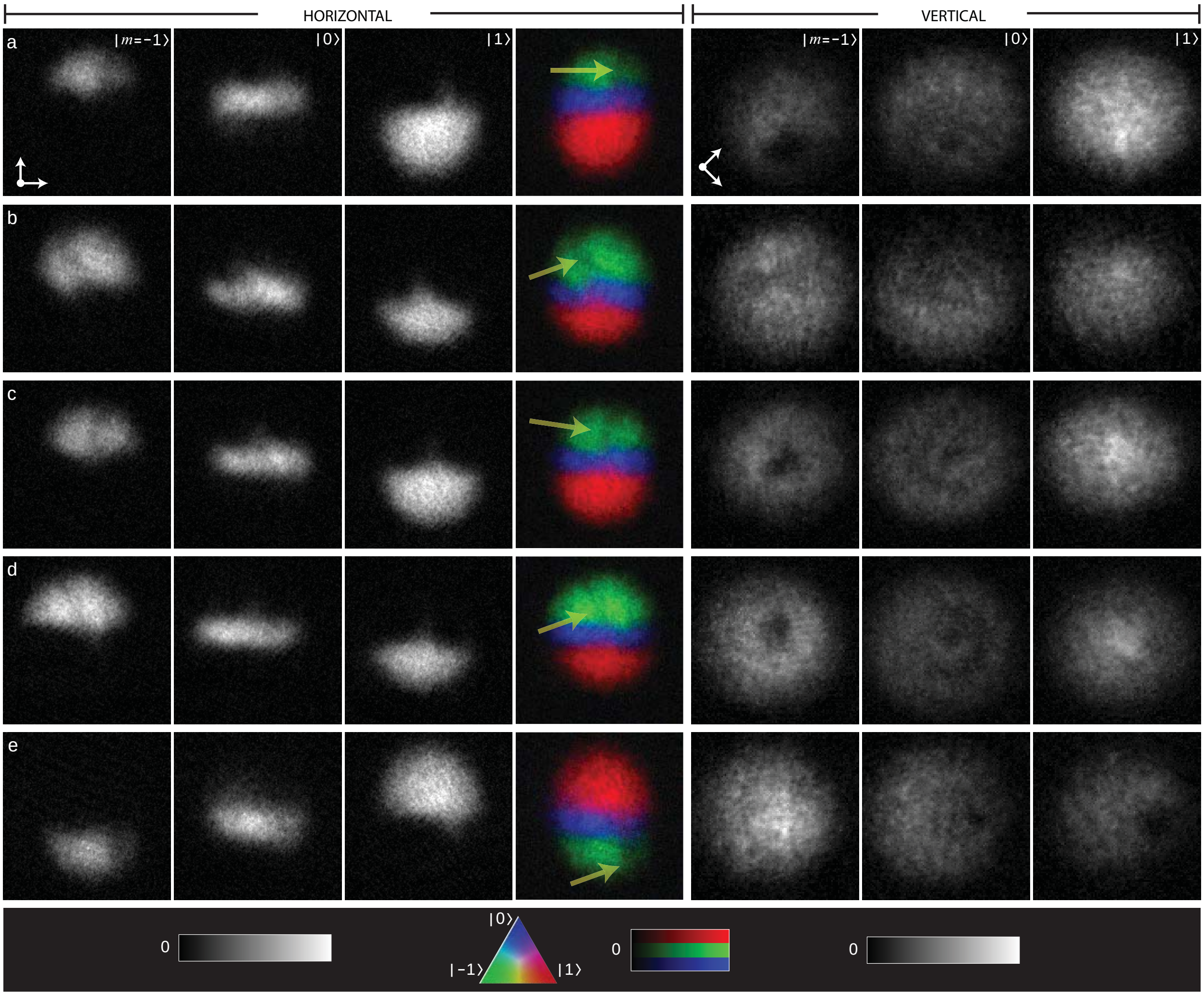

Extended Data Figure 2 | Additional representative images of Dirac monopoles. Each row contains images of the same condensate. The maximum pixel intensity corresponds to $\tilde{n}_p = 8.2\times10^8$ cm $^{\ 2}$, and the field of view is 220 μm × 220 μm in the vertical images, and 285 μm × 285 μm in the horizontal images. The arrow points to the density depletion that is identified as the nodal line. In **a**–**c** we use the same protocol outlined in the paper: an off-centre monopole (**a**); an angled nodal line that is visible in the side image, but not in the vertically directed image (**b**); and a nodal line that appears to be splitting into two vortices in the $|m=\ 1\rangle$ component (**c**). **d**, An example of a monopole spin structure in which the creation ramp is as described in the text but the projection ramp is reversed (that is, B_z is rapidly increased until $|B_z/B_{z,\mathrm{f}}| \gg 1$). **e**, Monopole spin structure created by moving the field zero into the condensate from below with $\dot{B}_z > 0$. The projection ramp is performed as described in **d**.

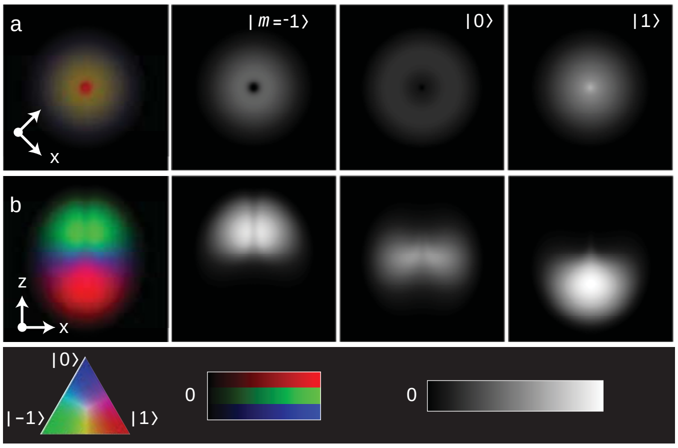

Extended Data Figure 3 | Numerical simulation of integrated particle densities before expansion. Vertically (**a**) and horizontally (**b**) integrated particle densities of a condensate just before the projection ramp, with $B_{z,\mathrm{f}}$ chosen such that the monopole is in the centre of the condensate. The fields of view are 17.2 μm × 17.2 μm (**a**) and 17.2 μm × 11.4 μm (**b**); in **b**, it is reduced in the z direction for a more convenient comparison to the simulations shown in Fig. 3. The maximum pixel intensity corresponds to $\tilde{n}_p = 2.98 \times 10^{11}$ cm^{-2}.

Observation of Dirac Monopoles in a Synthetic Magnetic Field

Supplementary Information

I. Spin Components — Our starting point is the spinor order parameter

$$\varPsi(r',t) = \psi(r',t)\zeta(r',t) = \sqrt{n(r',t)}e^{i\phi(r',t)}\zeta(r',t) \tag{6}$$

where ψ is a scalar order parameter expressed in terms of the condensate particle density $n = |\psi|^2$ and phase $\phi = \arg(\psi)$, and ζ is a normalised spinor with $\zeta^\dagger\zeta = 1$. The condensate spin is given by $S = \zeta^\dagger F \zeta$, where $F = F_x\hat{x}' + F_y\hat{y}' + F_z\hat{z}'$ and $\{F_k\}$ are the usual spin-1 matrices.

As B_z is decreased the spin rotates by an angle $\tilde{\theta} = \pi - \theta'$ about an axis $\hat{n} = -\hat{x}'\sin\varphi' + \hat{y}'\cos\varphi'$ as illustrated in Fig. 1. In the spinor basis $|F,m\rangle$ this spin rotation corresponds to a transformation matrix

$$\mathcal{R}(\tilde{\theta}) \equiv e^{-iF\cdot\hat{n}\,\tilde{\theta}/\hbar} = \begin{pmatrix} \frac{1}{2}(1+\cos\tilde{\theta}) & -\frac{1}{\sqrt{2}}e^{-i\varphi'}\sin\tilde{\theta} & \frac{1}{2}e^{-2i\varphi'}(1-\cos\tilde{\theta}) \\ \frac{1}{\sqrt{2}}e^{i\varphi'}\sin\tilde{\theta} & \cos\tilde{\theta} & -\frac{1}{\sqrt{2}}e^{-i\varphi'}\sin\tilde{\theta} \\ \frac{1}{2}e^{2i\varphi'}(1-\cos\tilde{\theta}) & \frac{1}{\sqrt{2}}e^{i\varphi'}\sin\tilde{\theta} & \frac{1}{2}(1+\cos\tilde{\theta}) \end{pmatrix} \tag{7}$$

The action of $\mathcal{R}$ on the initial spinor $(1,0,0)^{\mathrm{T}}$ is

$$\mathcal{R}(\tilde{\theta})\begin{pmatrix}1\\0\\0\end{pmatrix} = \begin{pmatrix} \frac{1}{2}(1+\cos\tilde{\theta}) \\ \frac{1}{\sqrt{2}}e^{i\varphi'}\sin\tilde{\theta} \\ \frac{1}{2}e^{2i\varphi'}(1-\cos\tilde{\theta}) \end{pmatrix} = \begin{pmatrix} \frac{1}{2}(1-\cos\theta') \\ \frac{1}{\sqrt{2}}e^{i\varphi'}\sin\theta' \\ \frac{1}{2}e^{2i\varphi'}(1+\cos\theta') \end{pmatrix} = \zeta \tag{8}$$

From the φ'-dependence of the resulting spinor, we observe that the $|-1\rangle$ component contains a doubly-quantized vortex, and the $|0\rangle$ component contains a singly-quantized vortex, and all three components vanish along a nodal line that lies along the $+z'$ axis.

II. Dirac Monopole in B^* — The gauge-field theory for spinor BECs has been published elsewhere[30,31]; we reproduce here only its essential elements, following ref. 31. We begin with the condensate order parameter as expressed in equation (6). The nonlinear Schrödinger equation governing the evolution of $\varPsi$ may be recast as a Schrödinger equation for a charged particle described by a scalar field ψ in the presence of synthetic electromagnetic scalar and vector potentials

$$\varPhi(r',t) = -i\zeta^\dagger\frac{\partial\zeta}{\partial t} \tag{9}$$

and

$$A^*(r', t) = i\zeta^\dagger \nabla' \zeta \tag{10}$$

where ∇' indicates differentiation with respect to the primed coordinate system. These potentials lead to the synthetic electromagnetic fields

$$E^* = \hbar\left(-\nabla' \Phi - \frac{\partial A^*}{\partial t}\right) \tag{11}$$

and

$$B^* = \hbar\left(\nabla' \times A^*\right) \tag{12}$$

which, together with the Lorentz force law

$$\frac{D}{Dt}(M v_s) = E^* + v_s \times B^* - \nabla' \mu \tag{13}$$

describe the superfluid dynamics. In equation (13), D/Dt is the material derivative, M is the atomic mass,

$$v_s = \frac{\hbar}{M}\left(\nabla' \phi - A^*\right) \tag{14}$$

is the superfluid velocity, and μ is a local chemical potential arising from kinetic, trap, and mean-field energies[31].

Applying equation (10) to the specific spin rotation in our experiment (equation (8)), we find

$$A^* = -\frac{1 + \cos\theta'}{r' \sin\theta'}\hat{\varphi}' \tag{15}$$

If $\nabla'\phi = 0$, a typical initial condition for the trapped condensate, then $v_s = -\hbar A^*/M$, establishing equation (1).

Equation (15) represents a vector potential with a singularity that lies along the nodal line in Ψ, that is, along the $+z'$ axis. Before calculating B^* from this A^*, consider the transformation

$$\psi \to \tilde{\psi} = \psi e^{-i\vartheta(r', t)} \qquad \text{and} \qquad \zeta \to \tilde{\zeta} = e^{i\vartheta(r', t)}\zeta \tag{16}$$

where ϑ parameterises the transformation. The condensate order parameter $\Psi = \psi\zeta = \tilde{\psi}\tilde{\zeta}$, as well as all of its associated observables (including E^* and B^* as implied by equation (13)), are invariant under this transformation. Using equations (9) and (10), the synthetic scalar and vector potentials transform as

$$\varPhi \to \tilde{\varPhi} = \varPhi + \frac{\partial \vartheta}{\partial t} \tag{17}$$

and

$$A^* \to \tilde{A}^* = A^* - \nabla' \vartheta \tag{18}$$

respectively. These equations are recognised as those of a gauge transformation in ordinary electrodynamics. The invariance of the physical observable v_s, and hence $\varOmega$, with respect to choice of gauge may be confirmed by evaluating equation (14).

One can use the choice of gauge to select the location of the singularity in A^*. For example, the gauge function $\vartheta = -2\varphi'$ gives

$$\tilde{A}^* = \frac{1 - \cos\theta'}{r' \sin\theta'} \hat{\varphi}' \tag{19}$$

which has a singularity along the negative z' axis. Similarly, choosing $\vartheta = -\varphi'$, yields

$$\tilde{A}^* = -\frac{\cot\theta'}{r'} \hat{\varphi}' \tag{20}$$

which contains two singularities that meet at the monopole, lying along the positive and negative z' axes. Finally, by choosing $\vartheta = -2\varphi' \varTheta(z')$, where $\varTheta(z')$ is the Heaviside step function, we obtain

$$\tilde{A}^* = \frac{1}{r' \sin\theta'} \left[(1 - \cos\theta') \varTheta(z') - (1 + \cos\theta') \varTheta(-z') \right] \hat{\varphi}' + 2\varphi' \delta(z') \hat{z}' \tag{21}$$

where $\delta(z')$ is the Dirac delta function. In this last case, the magnetic field is given directly by equation (3) without any singularities, i.e., the gauge transformation completely annihilates the Dirac string in B^*.

In the usual treatment of the Dirac monopole, the vector potential is expressed in terms of equation (21) without the last term[20]. Instead, two different gauges are employed for the first two terms, which can raise the question of how to connect, in practice, a solution extending across the gauge boundary. In contrast, we employ a single piecewise-defined gauge that answers this question and completely releases the Dirac monopole from its string in B^*. Thus a synthetic magnetic charge appears that is not strictly present in the gauge transformations involving the Dirac string in B^*.

We conclude that the singularity in B^* is not physical, as it is inferred from the gauge-dependent location of the singularity in $\tilde{A}^*$. Note that this is not true for the vortex line singularity in Ω, which depends on the location of the physical vortex line singularity in the gauge-invariant superfluid velocity v_s and must lie along the nodal line in Ψ.

III. Faraday's Law — In this section we use Faraday's law

$$\nabla' \times E^* = -\frac{\partial B^*}{\partial t} \tag{22}$$

to show explicitly that the motion of the monopole towards and through the condensate induces the superfluid velocity given by equation (1). This approach is complementary to the preceding method of computing the superfluid velocity from the quasi-static spinor that aligns with the instantaneous applied magnetic field.

We assume that the monopole begins infinitely far away from the condensate on the positive z' axis and moves towards it in the negative z' direction. The synthetic electric field E^* resulting from the motion of the monopole may be written[31]

$$E^* = \frac{\partial}{\partial t}(M v_s) + \nabla' \left[\mu + \frac{1}{2} M v_s^2\right] \tag{23}$$

The curl of this expression satisfies Faraday's law (equation (22)), which in its integral form is

$$\oint_{\mathcal{C}} E^* \cdot dl = -\frac{d}{dt} \int_{\mathcal{S}} B^* \cdot dS \tag{24}$$

where the flux of B^* is calculated through a capping surface $\mathcal{S}$ bounded by the directed curve $\mathcal{C}$.

We concentrate on the φ' component of E^*, which does not depend on the terms in the square brackets of equation (23) because those terms do not depend on φ'. On the other hand, the time-varying B^* induces an E^* which in our case, for reasons of symmetry, is entirely in the $(\pm)\varphi'$ direction.

Consider a superfluid mass element at $Q = (r', \theta', \varphi')$ with respect to the monopole (Supplementary Information Fig. 1). The curve $\mathcal{C}$ is a circular path of radius $\rho' = r' \sin\theta'$ passing through Q and centred upon the z' axis at a distance $z' = r' \cos\theta'$ from the monopole (N). Using equation (3) for the magnetic field of the monopole, equation (24) yields

$$\int_0^{2\pi} E^* \cdot \rho' \, d\varphi'' = \frac{d}{dt} \left\{ \frac{\hbar}{r'^2} \int_{\theta'}^{\pi} r'^2 \sin\theta'' \, d\theta'' \int_0^{2\pi} d\varphi'' \right\} \tag{25}$$

where the flux integral is calculated over a fraction of the spherical surface $\mathcal{S}$ of radius r' bounded by $\mathcal{C}$. Performing the integrals and simplifying, we find

$$E^* \cdot \hat{\varphi}' = \frac{d}{dt}\left\{\frac{\hbar}{r'}\left(\frac{z'+r'}{\rho'}\right)\right\} = \frac{d}{dt}\left\{\frac{\hbar}{r'}\left(\frac{\cos\theta'+1}{\sin\theta'}\right)\right\} \tag{26}$$

Equation (1) then follows directly by equating equation (26) with the φ' component of equation (23).

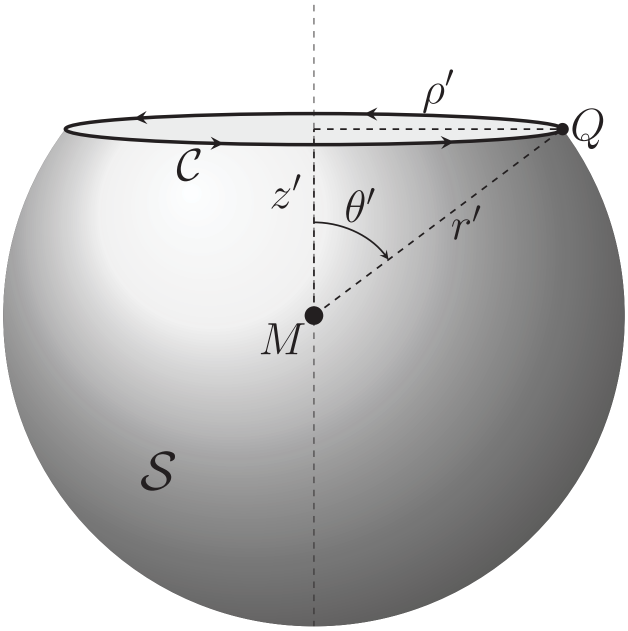

Supplementary Information Figure 1 | Calculation of the induced electric field due to the motion of the monopole. The monopole is at M, and a representative superfluid mass element is at Q. The synthetic magnetic flux is calculated through the open surface $\mathcal{S}$, which is bounded by the curve $\mathcal{C}$. Faraday's law yields the φ' component of E^* at Q as the monopole moves in the negative z' direction (downwards).

---

[30] Ho, T.-L. & Shenoy, V. B. Local spin-gauge symmetry of the Bose-Einstein condensates in atomic gases. *Phys. Rev. Lett.* **77**, 2595–2599 (1996).

[31] Kawaguchi, Y. & Ueda, M. Spinor Bose-Einstein condensates. *Physics Reports* **520**, 253–382 (2012).

Summer trainee project 2018, Department of Applied Physics

Research group: Quantum Computing and Devices (QCD)
Contact person: Dr. Mikko Möttönen (mikko.mottonen@aalto.fi)
Field of research: Nanoelectronics and Quantum Computing
Project title: Microwave detector
Project instructor: M.Sc. Roope Kokkoniemi, Dr. Dibyendu Hazra
Site of research: Aalto University, QCD group, Otaniemi
Website [Click here!]()
Level of student: applications from all students are welcome
(also for people applying for a Mater's or PhD thesis project)

Introduction

Quantum computer is an emerging computational device that can potentially solve some problems of practical interest that are impossible for the classical computer due to the required computational resources. Quantum bits, qubits, are the key ingredient of the quantum computer. Qubits can be employed to store and process quantum information, and they can be measured to obtain classical information out of the quantum world.

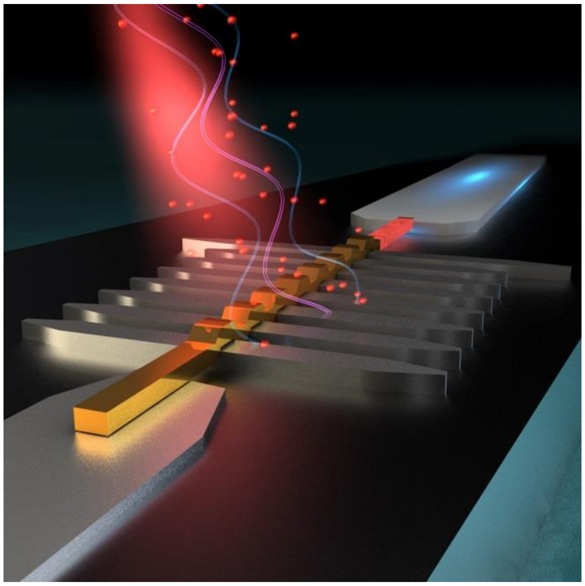

Figure 1. Artistic image of our microwave detector in operation. See the attached artciel for details. Credit: Ella Maru Studios.

Recently, there has been great development of different types of qubit architectures such as trapped ions, optical photons, nitrogen vacancies in diamond, superconducting qubits, and spin-based qubits. Although these technologies are not yet at the level of an actual large-scale quantum computer, they can be used, for example, as sensors of electric and magnetic noise.

One of the greatest developments in the recent years has been the rise of circuit quantum electrodynamics (cQED). Here, superconducting qubits are coupled to microwave cavities and waveguides working at microwave frequencies. This allows not only to reproduce quantum optics experiments carried out with optical photons but also for a spectrum new physics and applications. One of these applications is an already built on-demand high-fidelity single-photon source, a device that is lacking in the optical range. Furthermore, some superconducting devices have nonlinear character that can be used to couple the photons. Thus this opens up the avenue for a quantum computer based on single microwave photons.

Project goals

Your aim in this project is to use a detector for microwave photons to observe ultrasmall energy packets in a continuous mode. See the attached article on our detector design. This detector can ultimately be used as a measurement device for the single microwave photon qubits. Thus far we have the world record on the lowest energy of the microwave photon wave packets observed using a thermal detector. See our recent video on the subject: http://www.youtube.com/watch?v=dWcT_qrBN_w

Research site

Your site of research will be the premises of Quantum Computing and Devices, the so-called QCD Labs, on the Otaniemi campus of Aalto University. There are both theorists and experimentalists working in the group. See the group website (http://physics.aalto.fi/en/groups/qcd/) for more information.

Instructors

Your main instructor will be MSc Roope Kokkoniemi. Also our postdoc Dr. Dibyendu Hazra will assist. Help from other group members is also provided if required.

Working methods

Experiments on the topic will be carried out during your project using a sample already fabricated in the group. It is also possible to focus more on theoretical modelling of, for example, the detector noise properties arising from its coupling to the surrounding environment.

Thesis possibilities

Depending on your level, this project can be adjusted for a BSc thesis, special assignment, MSc thesis, or a PhD thesis project. Some knowledge of quantum mechanics and an excellent study record is preferred.

Detection of Zeptojoule Microwave Pulses Using Electrothermal Feedback in Proximity-Induced Josephson Junctions

J. Govenius,[*] R. E. Lake, K. Y. Tan, and M. Möttönen
QCD Labs, COMP Centre of Excellence, Department of Applied Physics, Aalto University,
P.O. Box 13500, FIN-00076 Aalto, Finland

(Received 22 December 2015; revised manuscript received 4 May 2016; published 15 July 2016)

We experimentally investigate and utilize electrothermal feedback in a microwave nanobolometer based on a normal-metal ($\mathrm{Au}_x\mathrm{Pd}_{1-x}$) nanowire with proximity-induced superconductivity. The feedback couples the temperature and the electrical degrees of freedom in the nanowire, which both absorbs the incoming microwave radiation, and transduces the temperature change into a radio-frequency electrical signal. We tune the feedback *in situ* and access both positive and negative feedback regimes with rich nonlinear dynamics. In particular, strong positive feedback leads to the emergence of two metastable electron temperature states in the millikelvin range. We use these states for efficient threshold detection of coherent 8.4 GHz microwave pulses containing approximately 200 photons on average, corresponding to 1.1×10^{-21} J ≈ 7.0 meV of energy.

DOI: 10.1103/PhysRevLett.117.030802

Superconducting qubits coupled to microwave transmission lines have developed into a versatile platform for solid-state quantum optics experiments [1,2], as well as a promising candidate for quantum computing [3,4]. However, compared to optical photodetectors [5–7], detectors for itinerant single-photon microwave pulses are still in their infancy. This prevents microwave implementations of optical protocols that require feedback conditioned on single-photon detection events. For example, linear optical quantum computing with single-photon pulses calls for such feedback [8]. Photodetection and feedback can also act as a quantum eraser [9] of the phase information available in a coherent signal, as we recently discussed in Ref. [10]. Note that, given sufficient averaging, linear amplifiers can substitute for photodetectors in ensemble-averaged experiments [11,12], but the uncertainty principle fundamentally limits the success probability in single-shot experiments.

We focus on thermal photodetectors, i.e., detectors that measure the temperature rise caused by absorbed photons. Thermal detectors have been developed for increasingly long wavelengths in the context of THz astronomy [13], the record being the detection of single 8 μm photons [14]. In the context of quantum thermodynamics [15], thermal detectors have recently been proposed [16] and developed [17–20] as monitorable heat baths.

The other main approach to detecting itinerant microwave photons is to use a qubit that is excited by an incoming photon and then measured [21–30]. Very recently, Ref. [29] reported reaching an efficiency of 0.66 and a bandwidth of roughly 20 MHz using such an approach. Use of qubit-based single-photon transistors as photodetectors has also been proposed [31,32]. If the pulse is carefully shaped, it is also possible to efficiently absorb a photon into a resonator [33–37]. There it could be detected with established techniques for intraresonator photon counting [38,39].

The main advantage of thermal detectors is that they typically present a suitable real input impedance for absorbing photons efficiently over a wide bandwidth and a large dynamic range, in contrast to qubit-based detectors. However, a central problem in the thermal approach is the small temperature rise caused by individual microwave photons. The resulting transient temperature spike is easily overwhelmed by noise added in the readout stage. One potential solution is to use a bistable system as a threshold detector that maps a weak transient input pulse to a long-lived metastable state of the detector. This is conceptually similar to, e.g., early experiments on superconducting qubits that used a current-biased superconducting quantum interference device (SQUID) [40]. Conditioned on the initial qubit state, the SQUID either remained in the superconducting state or switched to a long-lived nonzero voltage state.

In this Letter, we show that an electrothermal bistability emerges in the microwave nanobolometer we introduced in Ref. [41] and that it enables high-fidelity threshold detection of 8.4 GHz microwave pulses containing only $200 \times h \times 8.4$ GHz ≈ 1.1 zJ of energy. This threshold is more than an order of magnitude improvement over previous thermal detector results [14,42]. The bistability in our detector arises from the fact that the amount of power

---

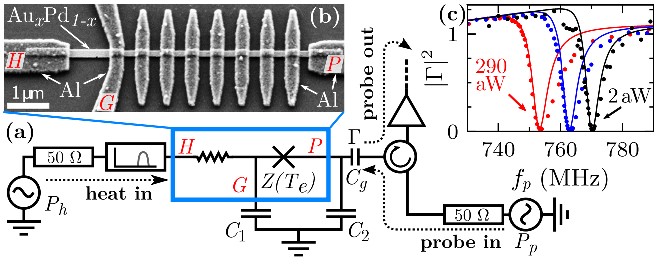

FIG. 1. (a) Simplified diagram of the detector, including (b) a micrograph of the *S*-*N*-*S* junctions formed by a Au$_x$Pd$_{1-x}$ nanowire contacted by Al islands and leads (*H*, *P*, and *G*). Here, Z^{-1} is an admittance, T_e is the temperature of the electrons in the nanowire, and Γ is the probe signal reflection coefficient. The micrograph is from a device nominally identical to the measured one. (c) Reflected fraction of probe power versus probe frequency f_p for steady-state heating power P_h of 1.9, 66, and 290 aW. They are measured at low probe power $P_p \ll P_h$. The solid curves are fits to the circuit model with a small phenomenological correction term [50]. The heater input is bandpass filtered (8.41 ± 0.02 GHz).

absorbed from the electrical probe signal used for readout depends on the measured electron temperature itself. Previously, such electrothermal feedback and the associated bifurcation has been studied in the context of kinetic inductance detectors [43–46]. Analogous thermal effects in optics are also known [47,48]. The main difference to our device is the relative strength of the electrothermal effect, which in our case leads to strongly nonlinear behavior at attowatt probe powers. Electrothermal feedback is also commonly used in transition edge sensors [13], but typically the feedback is chosen to be negative because that suppresses Johnson noise and leads to fast self-resetting behavior [49].

The central component of our detector (Fig. 1) is a metallic Au$_x$Pd$_{1-x}$ nanowire ($x \approx 0.6$) contacted by three Al leads (*H*, *P*, and *G*) and seven Al islands that are superconducting at millikelvin temperatures [50]. The longest superconductor–normal-metal–superconductor (*S*-*N*-*S*) junction (*H*-*G*) provides a resistive load (36 Ω) for the radiation to be detected [51], while the shorter junctions (*P*-*G*) function as a proximity Josephson sensor [52,53]. That is, the shorter junctions provide a temperature-dependent inductance in an effective *LC* resonator used for readout. Because the inductance increases with electron temperature T_e in the nanowire, the resonance frequency shifts down as the heating power P_h increases. Therefore the detector transduces changes in P_h into changes in the reflection coefficient Γ [Fig. 1(c)]. For simplicity, we limit the bandwidth of the heater line using a Lorentzian bandpass filter, but replacing it with a wider band filter should be straightforward.

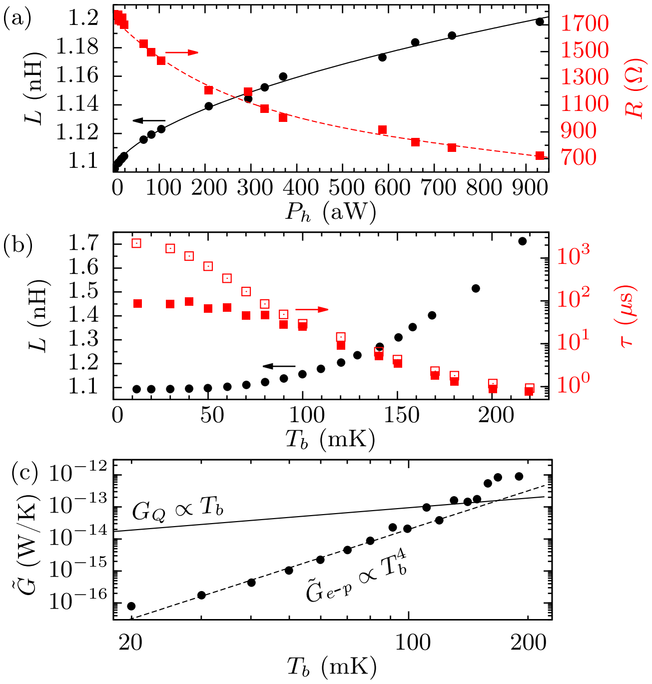

FIG. 2. Linear ($P_p \ll P_h$) response. (a) The effective inductance (circles) and resistance (squares) of the short *S*-*N*-*S* junctions as functions of external steady-state heating power P_h. The bath temperature T_b is 12 mK. The curves are phenomenological fits that allow mapping a measured reflection coefficient into an equivalent P_h. (b) The effective inductance (circles) and thermal relaxation time after a short (filled squares) or long (open squares) heating pulse. (c) Measured differential thermal conductance $\tilde{G}$, the expected electron-phonon contribution $\tilde{G}_{e\text{-}p}$ (dashed line), and the quantum of thermal conductance G_Q (solid line).

We first characterize the detector by measuring the P_h dependence of the admittance Z^{-1} between *P* and *G*. To do so, we fit the measured Γ to a circuit model in which we parametrize Z^{-1} as $R^{-1} + (i\omega L)^{-1}$, where $\omega/2\pi = f_p$ is the probe frequency. The circuit model shown in Fig. 1(a) predicts $\Gamma = (Z_L - Z_0)/(Z_L + Z_0)$, where

$$Z_L = (i\omega C_g)^{-1} + \{i\omega C_2 + [(i\omega C_1)^{-1} + Z(T_e)]^{-1}\}^{-1},$$

$Z_0 = 50\ \Omega$, $C_1 \approx 87$ pF, $C_2 \approx 70$ pF, and $C_g \approx 1.5$ pF. This fits reasonably well to the linear response data shown in Fig. 1(c). However, in order to reproduce the asymmetry in the measured line shape, we add a small frequency-dependent correction to the model [50]. Here, linear response refers to the use of a probe power P_p low enough to ignore both the electrical and electrothermal nonlinearities, i.e., the nonlinearity of the Josephson inductance as well as the variation of T_e as a function of the absorbed probe power $(1 - |\Gamma|^2)P_p$. We note that the uncertainty in P_h is roughly 1 dB [50], and that dissipation in the capacitors is negligible.

Figure 2(a) shows the extracted linear response *L* and *R* for heating powers up to a femtowatt. Figure 2 also shows the bath temperature dependence of *L*, the thermal relaxation time τ, and the differential thermal conductance $\tilde{G} = -\partial_{T_b} P_{e\text{-}b}(T_e, T_b)$ [50]. Here, $P_{e\text{-}b}(T_e, T_b)$ is the heat flow between the electrons in the nanowire and the cryostat phonon bath at temperature T_b. The measured $\tilde{G}$ is in rough agreement with the prediction for electron-phonon limited thermalization $\tilde{G}_{e\text{-}p} = 5\Sigma V_0 T_b^4$, where $\Sigma \approx 3\times 10^9\ \mathrm{W/m^3K^5}$ is a material parameter [54] and $V_0 \approx (240\ \mathrm{nm})^3$ is the volume of the part of the nanowire not covered by Al. We can use these results to estimate C_e above 100 mK, where $T_e \approx T_b$ and $C_e \approx \tau\tilde{G} \approx \gamma V_0 T_b$, with $\gamma V_0 = 8\ \mathrm{aJ/K^2}$ [50].

Below 100 mK, the relaxation toward the stationary state is faster after a short (1 μs) heating pulse than after a long ($\gg\tau$) heating pulse [50]. Therefore, the simplest thermal model of a single heat capacity C_e coupled directly to the bath is not accurate below 100 mK. Instead, the second time scale can be phenomenologically explained by an additional heat capacity $C' \gg C_e$ coupled strongly to C_e but weakly to the bath, as compared to $\tilde{G}$. Since $\tilde{G}$ falls far below the quantum of thermal conductance $G_Q = \pi^2 k_B^2 T_b/3h$ [55] at low temperatures [Fig. 2(c)], even weak residual electromagnetic coupling [56–58] between C_e and C' would suffice. However, we cannot uniquely determine the microscopic origin of C' or the coupling mechanism from the data. Also note that a similar second time scale was observed in Ref. [19].

At high probe powers, the linear-response behavior studied above may be drastically modified by the absorbed probe power. Below we focus on the stationary T_e solutions, so we choose to neglect the transient heat flows to C' that give rise to the shorter time scale in Fig. 2(b). Similarly, we neglect the contribution of electrical transients to Γ, as they decay even faster (in $\lesssim$100 ns). Under these approximations, T_e is the only dynamic variable and evolves according to

$$C_e(T_e)\dot{T}_e = -P_{e-b}(T_e, T_b) + P_x + P_h + (1 - |\Gamma(T_e, \omega)|^2)P_p, \qquad (1)$$

where P_x accounts for the average heat load from uncontrolled sources.

Determining T_e from Eq. (1) and the measured Γ would require additional assumptions about $P_{e\text{-}b}$ and P_x, as they are not directly measurable. However, we avoid making such assumptions by instead analyzing the increase in the heat flow from the electrons to the thermal bath, as compared to the case $P_h = P_p = 0$. That is, instead of T_e, we analyze

$$\Delta(T_e) = P_{e\text{-}b}(T_e, T_b) - P_x, \qquad (2)$$

which is monotonic in T_e. Given this definition, we can rewrite Eq. (1) as

$$\tau(\Delta)\dot{\Delta} = -\Delta + P_h + (1 - |\Gamma(\Delta, \omega)|^2)P_p, \qquad (3)$$

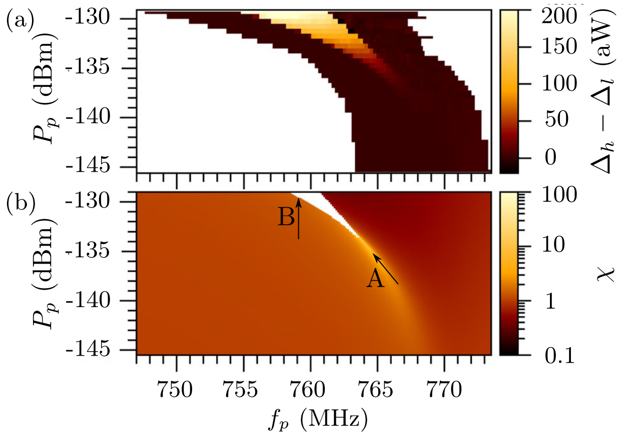

FIG. 3. (a) Bistable parameter regime, as indicated by a nonzero difference $\Delta_h - \Delta_l$ in the power absorbed from the probe signal in high and low-temperature stationary states. (b) Numerically simulated values of the dimensionless susceptibility to external heating χ in the single-valued regime. The bistable regime is indicated in white.

where $\tau(\Delta) = C(\Delta)/\partial_{T_e} P_{e\text{-}b}(T_e(\Delta), T_b)$. In contrast to the unknown parameters in Eq. (1), $\Gamma(\Delta, \omega)$ and $\tau(\Delta)$ are directly measurable in linear response. Specifically, we can determine $\Gamma(\Delta, \omega)$ from the data in Fig. 2(a) since $\Delta = P_h$ when $P_p, \dot{\Delta} \to 0$. By inverting $\Gamma(\Delta, \omega)$, we can then extract Δ from the measured Γ. Also note that, since all parameters in Eq. (3) are determined in linear response, no free parameters remain in the theoretical predictions for the nonlinear case discussed below.

The emergence of bistability is the most dramatic consequence of increasing the probe power. Experimentally, we map out the bistable parameter regime by measuring the difference $\Delta_h - \Delta_l$ as a function of f_p and P_p [Fig. 3(a)]. Here, Δ_h (Δ_l) corresponds to the ensemble-averaged Δ measured 5 ms after preparing the system in a high-Δ (low-Δ) initial state. We then identify the region of nonzero $\Delta_h - \Delta_l$ as the regime where Δ (and hence T_e) is bistable. This method is approximate mainly because the lifetimes of the metastable states may be short compared to 5 ms.

Figure 3(b) shows the theoretical prediction for the bistable region in white. We generate it by numerically finding the stationary solutions of Eq. (3), with $\Gamma(\Delta, \omega)$ determined from the fits shown in Fig. 2(a) [50]. The qualitative features of the prediction agree well with the experimental results. Quantitatively, the measured bistable regime broadens in frequency faster than the predicted one. This discrepancy is most likely due to imperfect impedance matching of the probe line and the imperfect correspondence between bistability and $\Delta_h - \Delta_l \neq 0$.

The nonwhite areas in Fig. 3(b) show the prediction for the susceptibility of the stationary-state Δ to external heating, i.e., $\chi = \partial\Delta/\partial P_h|_{\dot{\Delta}=0}$. It is a convenient dimensionless way to quantify the importance of the electrothermal nonlinearity. Besides characterizing susceptibility to heating, χ also gives the ratio of the effective thermal time constant to its linear response value. Figure 3(b) shows that both positive ($\chi \gg 1$) and negative ($\chi \ll 1$) feedback regimes are accessible by simply choosing different values of f_p and P_p.

There are two distinct ways to operate the device as a detector in the nonlinear regime. Approaching the bistable regime along line A in Fig. 3, the system undergoes a pitchfork bifurcation preceded by a diverging χ. Analogously to the linear amplification of coherent pulses by a Josephson parametric amplifier [59,60], our device could in principle detect heat pulses in a continuous and energy-resolving manner in this regime preceding the bifurcation. However, the focus of this Letter is threshold detection, which uses the imperfect pitchfork bifurcation encountered along line B in Fig. 3 and bears a closer resemblance to the Josephson bifurcation amplifier [61,62].

In the threshold detection mode, we modulate the probe signal amplitude as shown in Fig. 4(a) while keeping the probe frequency fixed at $f_p = 757$ MHz. The amplitude modulation pattern first initializes the system to a low-Δ state, then makes it sensitive to a transition to the high-Δ state for roughly $t_s \approx 4.5$ μs during which the heating pulse is sent, and finally keeps the system in a long-lifetime part of the bistable regime for another 7 ms in order to time average the output signal. During the last stage $P_p \approx -131$ dBm. This is similar to how Josephson bifurcation amplifiers operate [62]. Note, however, that the probe and heater signals do not interfere coherently due to the transduction through electron temperature. That is, at heater frequencies well above τ^{-1}, the output signal is independent of the phase of the heater signal.

The histograms in Figs. 4(b) and 4(c) show that the detector switches reliably to the high-temperature state with a heating pulse energy $E_{\text{pulse}} \gtrsim 1$ zJ, while it typically remains in the low-temperature state if no heating is applied. The histograms are plotted against $s = \text{Re}[e^{1.482\pi i} \int_{0.8\text{ ms}}^{6.4\text{ ms}} dt \Gamma(t)/(5.6\text{ ms})]$, i.e., a projection of the time-averaged reflection coefficient. Few switching events occur during the averaging time, as indicated by the scarcity of points between the two main peaks in the probability density $P(s)$. Instead, the errors arise from spurious early switching events and events where the detector does not switch despite a heating pulse. In particular, for a heat pulse of approximately 200 photons, the readout fidelity is $F = 0.56$ [Fig. 4(b)]. Here, $F = 1 - P(s > -0.25|\text{no heat pulse}) - P(s \leq -0.25|\text{heat pulse})$. For a heat pulse of 530 photons, $F = 0.94$ [Fig. 4(c)]. For 330 photons, $F = 0.75$ [50].

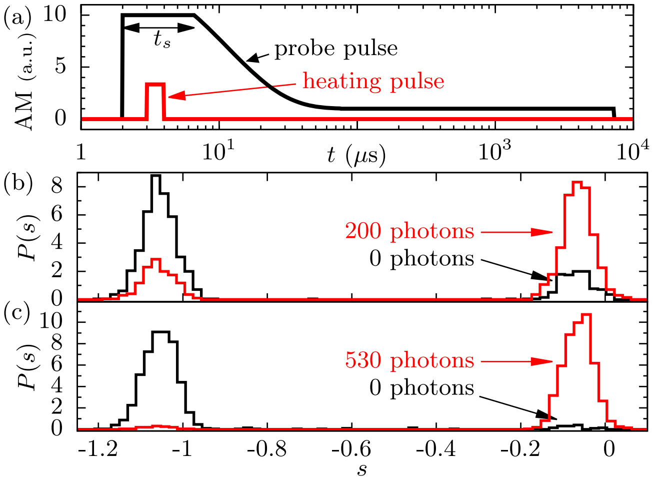

FIG. 4. (a) Amplitude modulation (AM) of the probe pulse used for detecting weak 1 μs heating pulses (also shown). The carrier frequencies are 757 MHz and 8.4 GHz for the probe and heating pulses, respectively. (b) Normalized histograms of the single-shot measurement outcome s with a heating pulse energy of zero or $200 \times h \times 8.4$ GHz ≈ 1.1 zJ. The pulses for the two histograms were interleaved in time. (c) Same as (b) but for 3.0 zJ and $t_s = 2.5$ μs.

The observed pulse energy dependence of F is in agreement with the errors arising mainly from Gaussian fluctuations in the energy of the nanowire electrons. Such fluctuations limit F to $\bar{F} = \text{erf}(2^{-3/2} E_{\text{pulse}}/\Delta E_{\text{rms}})$, even for ideal instantaneous threshold detection. For rms fluctuations $\Delta E_{\text{rms}} = 0.7$ zJ, $\bar{F}$ agrees well with the above mentioned values of F. This phenomenological ΔE_{rms} should be compared to the thermodynamic fluctuations $\Delta E'_{\text{rms}} = \sqrt{k_B T_e^2 C_e}$ in the absence of electrothermal feedback [63]. For $T_e = 50$ mK, we estimate $C_e \approx 400$ zJ/K, leading to $\Delta E'_{\text{rms}} \approx 0.12$ zJ $\approx C_e \times 0.29$ mK. This suggests that the thermodynamic fluctuations are a significant, even if not the dominant, fidelity-limiting factor. Note that, although the feedback during the pulse sequence in Fig. 4(a) is strong and positive, all signals are kept off for at least 400 ms before each probe pulse. Therefore, the fluctuations just before the brief period relevant for switching ($t_s \ll \tau$) are not affected by the electrothermal feedback.

In conclusion, we have experimentally investigated the electrothermal feedback effect in a microwave photodetector. The results are in agreement with a simple model which we used to highlight that both strong positive and strong negative feedback is available by adjusting the probe power and frequency. We demonstrated that bistability emerges in the limit of extreme positive feedback and that it can be used for efficient threshold detection of weak microwave pulses at the zeptojoule level. This is more than an order of magnitude improvement over previous thermal detector results, and therefore an important step toward thermal detection of individual itinerant microwave photons. To reach the single-photon level, we should further reduce the nanowire volume and possibly replace $\text{Au}_x\text{Pd}_{1-x}$ by a material with lower specific heat. This would reduce the time constant as well as the thermodynamic energy fluctuations, which contribute significantly to the achieved fidelities according to our estimate. Furthermore, there seems to be room for technical improvement in shielding and filtering, which would bring the observed ΔE_{rms} closer to the thermodynamic fluctuations and would, most likely, lead to a lower electron temperature. Finally, a state-of-the-art amplifier [64–66] on the probe output should reduce the required averaging time by at least two orders of magnitude [50].

We thank Leif Grönberg for depositing the Nb used in this work, Ari-Pekka Soikkeli for discussion on modeling the bistability, and Matti Partanen for technical assistance. We also acknowledge the financial support from the Emil Aaltonen Foundation, the European Research Council under Grant No. 278117 ("SINGLEOUT"), the Academy of Finland under Grants No. 265675, No. 251748, No. 284621, No. 135794, No. 272806, No. 286215, and No. 276528, and the European Metrology Research Programme ("EXL03 MICROPHOTON"). The EMRP is jointly funded by the EMRP participating countries within EURAMET and the European Union. In addition, we acknowledge the provision of facilities by Aalto University at OtaNano–Micronova Nanofabrication Centre.

---

[*] joonas.govenius@aalto.fi

[1] A. Blais, R.-S. Huang, A. Wallraff, S. M. Girvin, and R. J. Schoelkopf, Phys. Rev. A **69**, 062320 (2004).
[2] A. Wallraff, D. I. Schuster, A. Blais, L. Frunzio, R.-S. Huang, J. Majer, S. Kumar, S. M. Girvin, and R. J. Schoelkopf, Nature (London) **431**, 162 (2004).
[3] M. H. Devoret and R. J. Schoelkopf, Science **339**, 1169 (2013).
[4] J. Kelly, R. Barends, A. G. Fowler, A. Megrant, E. Jeffrey, T. C. White, D. Sank, J. Y. Mutus, B. Campbell, Y. Chen, Z. Chen, B. Chiaro, A. Dunsworth, I. C. Hoi, C. Neill, P. J. J. O'Malley, C. Quintana, P. Roushan, A. Vainsencher, J. Wenner, A. N. Cleland, and J. M. Martinis, Nature (London) **519**, 66 (2015).
[5] A. E. Lita, A. J. Miller, and S. W. Nam, Opt. Express **16**, 3032 (2008).
[6] F. Marsili, V. B. Verma, J. A. Stern, S. Harrington, A. E. Lita, T. Gerrits, I. Vayshenker, B. Baek, M. D. Shaw, R. P. Mirin, and S. W. Nam, Nat. Photonics **7**, 210 (2013).
[7] M. D. Eisaman, J. Fan, A. Migdall, and S. V. Polyakov, Rev. Sci. Instrum. **82**, 071101 (2011).
[8] P. Kok, K. Nemoto, T. C. Ralph, J. P. Dowling, and G. J. Milburn, Rev. Mod. Phys. **79**, 135 (2007).
[9] M. Hillery and M. O. Scully, in *Quantum Optics, Experimental Gravity, and Measurement Theory*, NATO Advanced Science Institutes Series Vol. 94, edited by P. Meystre and M. O. Scully (Plenum Press, New York, 1983) pp. 65–85.
[10] J. Govenius, Y. Matsuzaki, I. G. Savenko, and M. Möttönen, Phys. Rev. A **92**, 042305 (2015).
[11] M. P. da Silva, D. Bozyigit, A. Wallraff, and A. Blais, Phys. Rev. A **82**, 043804 (2010).
[12] D. Bozyigit, C. Lang, L. Steffen, J. M. Fink, C. Eichler, M. Baur, R. Bianchetti, P. J. Leek, S. Filipp, M. P. da Silva, A. Blais, and A. Wallraff, Nat. Phys. **7**, 154 (2011).
[13] B. S. Karasik, A. V. Sergeev, and D. E. Prober, IEEE Trans. Terahertz Sci. Technol. **1**, 97 (2011).
[14] B. S. Karasik, S. V. Pereverzev, A. Soibel, D. F. Santavicca, D. E. Prober, D. Olaya, and M. E. Gershenson, Appl. Phys. Lett. **101**, 052601 (2012).
[15] J. P. Pekola, Nat. Phys. **11**, 118 (2015).
[16] J. P. Pekola, P. Solinas, A. Shnirman, and D. V. Averin, New J. Phys. **15**, 115006 (2013).
[17] D. R. Schmidt, C. S. Yung, and A. N. Cleland, Appl. Phys. Lett. **83**, 1002 (2003).
[18] D. R. Schmidt, K. W. Lehnert, A. M. Clark, W. D. Duncan, K. D. Irwin, N. Miller, and J. N. Ullom, Appl. Phys. Lett. **86**, 053505 (2005).
[19] S. Gasparinetti, K. L. Viisanen, O.-P. Saira, T. Faivre, M. Arzeo, M. Meschke, and J. P. Pekola, Phys. Rev. Applied **3**, 014007 (2015).
[20] O. P. Saira, M. Zgirski, K. L. Viisanen, D. S. Golubev, and J. P. Pekola, arXiv:1604.05089.
[21] G. Romero, J. J. García-Ripoll, and E. Solano, Phys. Rev. Lett. **102**, 173602 (2009).
[22] Y.-F. Chen, D. Hover, S. Sendelbach, L. Maurer, S. T. Merkel, E. J. Pritchett, F. K. Wilhelm, and R. McDermott, Phys. Rev. Lett. **107**, 217401 (2011).
[23] B. Peropadre, G. Romero, G. Johansson, C. M. Wilson, E. Solano, and J. J. García-Ripoll, Phys. Rev. A **84**, 063834 (2011).
[24] B. Fan, A. F. Kockum, J. Combes, G. Johansson, I.-C. Hoi, C. M. Wilson, P. Delsing, G. J. Milburn, and T. M. Stace, Phys. Rev. Lett. **110**, 053601 (2013).
[25] I.-C. Hoi, A. F. Kockum, T. Palomaki, T. M. Stace, B. Fan, L. Tornberg, S. R. Sathyamoorthy, G. Johansson, P. Delsing, and C. M. Wilson, Phys. Rev. Lett. **111**, 053601 (2013).
[26] S. R. Sathyamoorthy, L. Tornberg, A. F. Kockum, B. Q. Baragiola, J. Combes, C. M. Wilson, T. M. Stace, and G. Johansson, Phys. Rev. Lett. **112**, 093601 (2014).
[27] B. Fan, G. Johansson, J. Combes, G. J. Milburn, and T. M. Stace, Phys. Rev. B **90**, 035132 (2014).
[28] K. Koshino, K. Inomata, Z. Lin, Y. Nakamura, and T. Yamamoto, Phys. Rev. A **91**, 043805 (2015).
[29] K. Inomata, Z. Lin, K. Koshino, W. D. Oliver, J.-S. Tsai, T. Yamamoto, and Y. Nakamura, arXiv:1601.05513.
[30] A. Narla, S. Shankar, M. Hatridge, Z. Leghtas, K. M. Sliwa, E. Zalys-Geller, S. O. Mundhada, W. Pfaff, L. Frunzio, R. J. Schoelkopf, and M. H. Devoret, arXiv:1603.03742.
[31] L. Neumeier, M. Leib, and M. J. Hartmann, Phys. Rev. Lett. **111**, 063601 (2013).
[32] M. T. Manzoni, F. Reiter, J. M. Taylor, and A. S. Sørensen, Phys. Rev. B **89**, 180502 (2014).
[33] J. I. Cirac, P. Zoller, H. J. Kimble, and H. Mabuchi, Phys. Rev. Lett. **78**, 3221 (1997).
[34] Y. Yin, Y. Chen, D. Sank, P. J. J. O'Malley, T. C. White, R. Barends, J. Kelly, E. Lucero, M. Mariantoni, A. Megrant, C. Neill, A. Vainsencher, J. Wenner, A. N. Korotkov, A. N. Cleland, and J. M. Martinis, Phys. Rev. Lett. **110**, 107001 (2013).
[35] S. J. Srinivasan, N. M. Sundaresan, D. Sadri, Y. Liu, J. M. Gambetta, T. Yu, S. M. Girvin, and A. A. Houck, Phys. Rev. A **89**, 033857 (2014).
[36] J. Wenner, Y. Yin, Y. Chen, R. Barends, B. Chiaro, E. Jeffrey, J. Kelly, A. Megrant, J. Y. Mutus, C. Neill,

P. J. J. O'Malley, P. Roushan, D. Sank, A. Vainsencher, T. C. White, A. N. Korotkov, A. N. Cleland, and J. M. Martinis, Phys. Rev. Lett. **112**, 210501 (2014).

[37] M. Pechal, L. Huthmacher, C. Eichler, S. Zeytinoğlu, A. A. Abdumalikov, S. Berger, A. Wallraff, and S. Filipp, Phys. Rev. X **4**, 041010 (2014).

[38] S. Gleyzes, S. Kuhr, C. Guerlin, J. Bernu, S. Deléglise, U. Busk Hoff, M. Brune, J.-M. Raimond, and S. Haroche, Nature (London) **446**, 297 (2007).

[39] L. Sun, A. Petrenko, Z. Leghtas, B. Vlastakis, G. Kirchmair, K. M. Sliwa, A. Narla, M. Hatridge, S. Shankar, J. Blumoff, L. Frunzio, M. Mirrahimi, M. H. Devoret, and R. J. Schoelkopf, Nature (London) **511**, 444 (2014).

[40] I. Chiorescu, Y. Nakamura, C. J. P. M. Harmans, and J. E. Mooij, Science **299**, 1869 (2003).

[41] J. Govenius, R. E. Lake, K. Y. Tan, V. Pietilä, J. K. Julin, I. J. Maasilta, P. Virtanen, and M. Möttönen, Phys. Rev. B **90**, 064505 (2014).

[42] D. F. Santavicca, B. Reulet, B. S. Karasik, S. V. Pereverzev, D. Olaya, M. E. Gershenson, L. Frunzio, and D. E. Prober, Appl. Phys. Lett. **96**, 083505 (2010).

[43] P. J. de Visser, S. Withington, and D. J. Goldie, J. Appl. Phys. **108**, 114504 (2010).

[44] S. E. Thompson, S. Withington, D. J. Goldie, and C. N. Thomas, Supercond. Sci. Technol. **26**, 095009 (2013).

[45] M. A. Lindeman, J. Appl. Phys. **116**, 024506 (2014).

[46] C. N. Thomas, S. Withington, and D. J. Goldie, Supercond. Sci. Technol. **28**, 045012 (2015).

[47] V. B. Braginsky, M. L. Gorodetsky, and V. S. Ilchenko, Phys. Lett. A **137**, 393 (1989).

[48] A. E. Fomin, M. L. Gorodetsky, I. S. Grudinin, and V. S. Ilchenko, J. Opt. Soc. Am. B **22**, 459 (2005).

[49] K. D. Irwin, Appl. Phys. Lett. **66**, 1998 (1995).

[50] See Supplemental Material at http://link.aps.org/supplemental/10.1103/PhysRevLett.117.030802 for additional single-shot histograms and for details of the experimental setup, the circuit model, the numerical model, and the measurements of $\tilde{G}$, τ, and C_e.

[51] M. Nahum and J. M. Martinis, Appl. Phys. Lett. **63**, 3075 (1993).

[52] F. Giazotto, T. T. Heikkilä, G. P. Pepe, P. Helistö, A. Luukanen, and J. P. Pekola, Appl. Phys. Lett. **92**, 162507 (2008).

[53] J. Voutilainen, M. A. Laakso, and T. T. Heikkilä, J. Appl. Phys. **107**, 064508 (2010).

[54] A. V. Timofeev, M. Helle, M. Meschke, M. Möttönen, and J. P. Pekola, Phys. Rev. Lett. **102**, 200801 (2009).

[55] J. B. Pendry, J. Phys. A **16**, 2161 (1983).

[56] D. R. Schmidt, R. J. Schoelkopf, and A. N. Cleland, Phys. Rev. Lett. **93**, 045901 (2004).

[57] M. Meschke, W. Guichard, and J. P. Pekola, Nature (London) **444**, 187 (2006).

[58] M. Partanen, K. Y. Tan, J. Govenius, R. E. Lake, M. K. Mäkelä, T. Tanttu, and M. Möttönen, Nat. Phys. **12**, 460 (2016).

[59] H. Zimmer, Appl. Phys. Lett. **10**, 193 (1967).

[60] M. A. Castellanos-Beltran and K. W. Lehnert, Appl. Phys. Lett. **91**, 083509 (2007).

[61] I. Siddiqi, R. Vijay, F. Pierre, C. M. Wilson, M. Metcalfe, C. Rigetti, L. Frunzio, and M. H. Devoret, Phys. Rev. Lett. **93**, 207002 (2004).

[62] R. Vijay, M. H. Devoret, and I. Siddiqi, Rev. Sci. Instrum. **80**, 111101 (2009).

[63] S. H. Moseley, J. C. Mather, and D. McCammon, J. Appl. Phys. **56**, 1257 (1984).

[64] R. Vijay, D. H. Slichter, and I. Siddiqi, Phys. Rev. Lett. **106**, 110502 (2011).

[65] M.-O. André, M. Mück, J. Clarke, J. Gail, and C. Heiden, Appl. Phys. Lett. **75**, 698 (1999).

[66] C. Macklin, K. O'Brien, D. Hover, M. E. Schwartz, V. Bolkhovsky, X. Zhang, W. D. Oliver, and I. Siddiqi, Science **350**, 307 (2015).

Summer trainee project 2018, Department of Applied Physics

Research group: Quantum Computing and Devices (QCD)
Contact person: Dr. Mikko Möttönen (mikko.mottonen@aalto.fi)
Field of research: Nanoelectronics
Project title: Single-electron pump based on a quantum dot
Project instructor: M.Sc. Maté Jenei and Dr. Vasilii Sevriuk
Site of research: Aalto University
Website Click here!
Level of student: applications from all students are welcome
(also for people applying for a Mater's or PhD thesis project)

Introduction

Quantum dots are nanometer scale potential wells, where electrons can be controllably trapped. Quantum mechanics plays a crucial role here since it determines, for example, the energy level spacing and transport properties of the device. Quantum dots have been employed to date, for example, to study fundamental quantum phenomena in solid state, as sensitive charge sensors (single-electron transistors), and as quantum bits, the building blocks of a quantum computer.

Project goals

Your aim in this project is to study how silicon quantum dots can be employed to pump single electrons in an electric circuit, thus realizing an accurate current source. To date, nobody has been able to demonstrate a more accurate high-yield single-electron pump based on silicon than us. This source can potentially be used to redefine the SI unit ampere which is now based on classical definition of force induced between two current carrying conductors. Please, see the attached recent article that accesses this problem. In the attached article, we were able for the first time to confirm that a pumped direct current matches to that obtained from counting each individual electron. A new generation of improved quantum dot devices will be used for the purposes of this project.

Research site

Your site of research will be the premises of Quantum Computing and Devices, the so-called QCD Labs, on the Otaniemi campus of Aalto University. There are both theorists and experimentalists working in the group. See the group website (http://physics.aalto.fi/en/groups/qcd/) for more information.

Instructors

Your main instructors will be M.Sc. Maté Jenei and Dr. Vasilii Sevriuk.

Working methods

The work will likely involve theory and modeling of silicon quantum dots and single-electron tunneling. Also experiments will be carried out on these devices and you are encouraged to be involved in them as well. One option is to focus completely on the experiments.

Thesis possibilities

Depending on your level, this project can be adjusted for a BSc thesis, special assignment, MSc thesis, or a PhD thesis project. An excellent study record is a preferred.

IOP Publishing New J. Phys. 17 (2015) 103030 doi:10.1088/1367-2630/17/10/103030

New Journal of Physics
The open access journal at the forefront of physics

Deutsche Physikalische Gesellschaft DPG
IOP Institute of Physics

Published in partnership with: Deutsche Physikalische Gesellschaft and the Institute of Physics

OPEN ACCESS

RECEIVED
16 July 2015

REVISED
7 September 2015

ACCEPTED FOR PUBLICATION
23 September 2015

PUBLISHED
16 October 2015

PAPER

Electron counting in a silicon single-electron pump

Tuomo Tanttu[1], **Alessandro Rossi**[2], **Kuan Yen Tan**[1], **Kukka-Emilia Huhtinen**[1], **Kok Wai Chan**[2,3], **Mikko Möttönen**[1] **and Andrew S Dzurak**[2]

[1] QCD Labs, COMP Centre of Excellence, Department of Applied Physics, Aalto University, PO Box 13500, 00076 Aalto, Finland
[2] School of Electrical Engineering & Telecommunications,The University of New South Wales, Sydney 2052, Australia
[3] Present address: Centre for Advanced 2D Materials and Graphene Research Centre, National University of Singapore, Singapore

E-mail: tuomo.tanttu@aalto.fi

Keywords: quantum dots, charge pumping, electron counting, single-electron pump

Abstract

We report electron counting experiments in a silicon metal-oxide-semiconductor quantum dot architecture which has been previously demonstrated to generate a quantized current in excess of 80 pA with uncertainty below 30 parts per million. Single-shot detection of electrons pumped into a reservoir dot is performed using a capacitively coupled single-electron transistor. We extract the full probability distribution of the transfer of n electrons per pumping cycle for $n = 0, 1, 2, 3,$ and 4. We find that the probabilities extracted from the counting experiment are in agreement with direct current measurements in a broad range of dc electrochemical potentials of the pump. The electron counting technique is also used to confirm the improving robustness of the pumping mechanism with increasing electrostatic confinement of the quantum dot.

1. Introduction

Recent development in the field of single-charge pumping has provided a basis for the emerging quantum standard of the ampere in the International System of Units (SI) [1]. This standard will be based on an agreed value for the elementary charge e and the frequency f, the product of which yields the ampere.

Single-charge pumps and turnstiles have been implemented in many different physical systems including normal-metal tunnel junction devices [2–4], superconducting devices [5–7], hybrid superconductor-normal-metal turnstiles [8, 9], semiconductor quantum dots [10–15], and single atom-sized impurities [16–19]. A satisfactory relative pumping accuracy at the 10^{-8} level has only been demonstrated in normal-metal devices in the picoampere range [3]. This current, however, falls significantly below 100 pA which is required for a practical realization of the quantum current standard [20]. The most accurate single-electron pumps that produce high enough current are thus far based on GaAs quantum dots [21]. Recently, an uncertainty 0.2 parts per million (ppm) levels has been reached at 87-pA current [22].

Silicon quantum dots [12, 14, 23–25] provide a promising alternative to the GaAs platform. Devices fully based on silicon have exhibited greatly suppressed $1/f$ noise and absence of large amplitude background charge jumps [26]. To date the most accurate silicon single-electron pumps produce a pumped current of 80 pA with uncertainty below 30 ppm [14].

The accuracy of the electron pump is essentially given by missed or excess electrons pumped per cycle. It is possible to arrange the electron pumps such that the pumping errors can be *in situ* observed with a nearby charge sensor, thus providing a self-referenced current source. Although several experiments [3, 18, 23, 27–35] provide observations on the pumping errors and the number of electrons transferred per cycle, a thorough comparison of the direct current provided by the electron pump and the results of the electron counting scheme is lacking. Only comparison between electron counting and the current flowing through a non-driven system has been reported [36].

In this paper, we demonstrate electron counting in a silicon electron pump utilizing the quantum dot architecture which has provided the most accurate results in silicon [14], thus providing a proof of concept for a self-referenced silicon charge pump. Furthermore, the average number of pumped electrons per cycle, n,

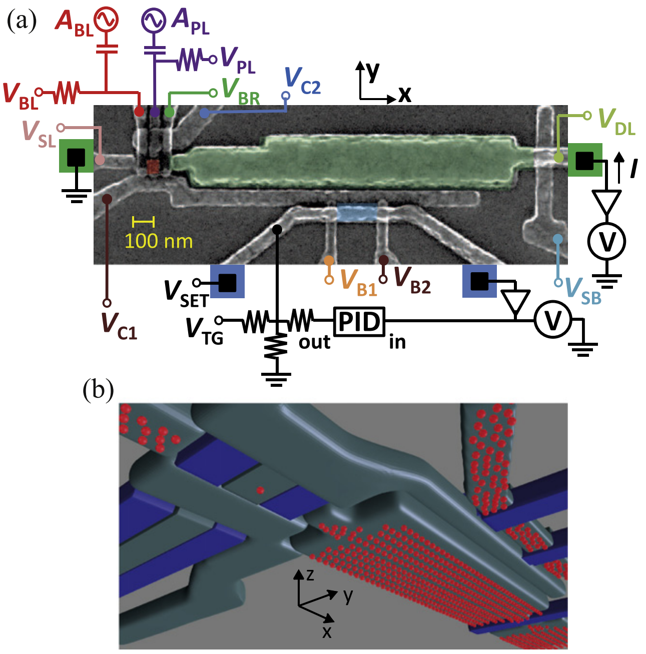

Figure 1. (a) False-color scanning electron micrograph of a device similar to the one used in the experiments together with a sketch of the measurement setup. The quantum dot (QD) used to pump electrons is highlighted in red. The reservoir dot (RES), into which the electrons are pumped, is green and the dot of the single-electron transistor sensor is highlighted in blue. The green (blue) squares represent the source and drain ohmic contacts of the pump (sensor). The gates are labelled according to their indicated dc voltages. (b) Schematic illustration of the device gate layout from below. Electric fields induced by the gate voltages are used to selectively accumulate electrons (red spheres) at the $\mathrm{Si/SiO_2}$ interface (not shown). Gates highlighted in blue are used to form tunnel barriers.

extracted from our electron counting scheme agrees with that obtained from the pumped direct current. This result verifies the consistency between these two schemes.

2. Experimental methods

Our device shown in figures 1(a), 1(b), and 2(a) is fabricated using metal-oxide-semiconductor (MOS) technology on a near-intrinsic silicon substrate with 8 nm thermally grown SiO_2 gate-oxide [14, 37]. The aluminum gates are defined with electron beam lithography in three layers isolated from each other by thermally grown Al_yO_x. The topmost layer of gates is used to accumulate a two-dimensional electron gas (2DEG) at the $\mathrm{Si/SiO_2}$ interface and the two bottom layers are used to control the electrostatic confinement of the dot in the planar directions by locally depleting the 2DEG and forming tunnel barriers. A schematic potential landscape of the device is presented in figure 2(b).

We employ two different measurement schemes: the *direct-current scheme* and the *electron counting scheme*. In the direct-current scheme, we induced a 2DEG below the source lead (SL), drain lead (DL), and switch barrier (SB) gates (see figure 1(a)). The pump dot is induced with the plunger gate (PL) such that the left barrier (BL) and right barrier (BR) gates are used to define tunable tunnel barriers between the leads and the dot. The confining gates (C1 and C2) are set to negative voltage to tighten the dot potential as first demonstrated in [14]. Experiments in both schemes are carried out in a cryostat with a bath temperature of 180 mK.

The gates PL and BL are also connected to an arbitrary-waveform generator providing the voltage drive for the dot to pump the electrons from the source to the drain. As shown in figure 2(c) the waveforms of the pulses consist of three consecutive parts: (i) voltage $s_1(t) = A_{\mathrm{PL/BL}}[1 - \cos(2\pi t/T)]/2$ for $0 \leqslant t < T$, (ii) voltage $s_2(t) = -s_1(2T - t)$ for $T \leqslant t < 2T$, and (iii) zero voltage for $2T \leqslant t \leqslant 2T + t_{\mathrm{w}}$. The period of the sinusoidal part is fixed at $T = 50$ ns and the pumping frequency $f = 1/(2\,T + t_{\mathrm{w}})$ is adjusted by changing the wait time $t_{\mathrm{w}} \gg T$. The temporal offset of the pulses in PL and BL is 13.6 ns and the voltage amplitudes at the sample are denoted by A_{PL} and A_{BL}, respectively. The induced current is measured from the drain side using a room-temperature transimpedance amplifier. In the direct-current scheme, we have $t_{\mathrm{w}} = 1.9\ \mu$s that yields $ef = 0.08$ pA. The waveform has to be adjusted such that the integral of the positive and negative area vanishes. Otherwise we need to adjust the dc bias of the gates for each t_{w} to achieve the desired potential due to the loss of the dc component of the waveform in the capacitor of the bias tee.

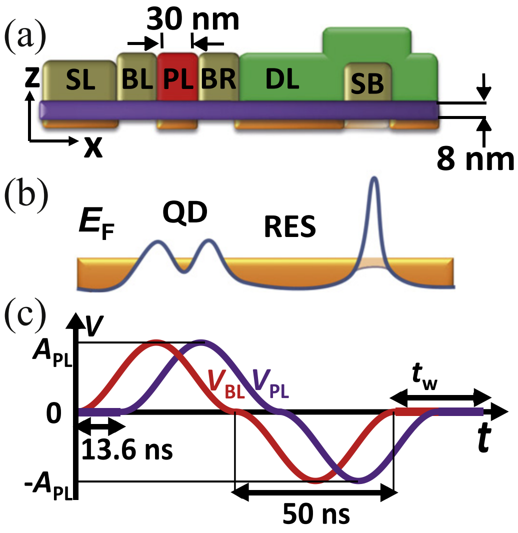

Figure 2. (a) Schematic cross section and (b) potential landscape of the device along x. By changing V_{SB} we can vary the reservoir to be either a large dot (electron counting scheme) or a current lead (direct-current scheme). The 2DEG is indicated with orange. The shaded area indicates 2DEG which can be induced or depleted by varying V_{SB}. (c) The repeated waveforms for the voltage drives on BL (red) and PL (purple) used in the experiment.

The electron counting scheme has the following differences from the scheme described above: We use a much lower V_{SB} to define a reservoir dot below the DL gate bounded by SB, C1, and BR gates. The charge state of the reservoir is monitored with a capacitively coupled single-electron transistor (SET). The SET is induced with the top gate (TG) and barrier gates (B1 and B2). The hold time of the charge state of the reservoir was measured at gate voltages similar to the one used for the counting experiments and showed stability of several hours. The current through the voltage biased SET is transimpedance amplified and channeled to a proportional-integral-derivative (PID) controller which keeps the operation point of the SET fixed by compensating V_{TG}. Electrons are pumped to the reservoir with an identical waveform as in the direct-current scheme but with relatively long wait time $t_w = 750$ ms. After a fixed number of subsequent pumping pulses, the reservoir is initialized by inducing a 2DEG below BL, PL, and BR so that the excess electrons flow from the reservoir back to the source.

3. Results

Figure 3(a) shows a representative trace of the SET current signal as a function of time when electrons are pumped into the reservoir. At each pumping event, there is a clear peak in the signal which subsequently saturates back to the set point of the PID controller. The PID controller is employed to enhance the signal to noise ratio compared with the current threshold method used in other electron counting experiments [18, 33, 34]. The advantages of this method [3] are that the low-frequency noise is filtered out and the sensor works at its most sensitive operation point at all times. We characterize the electron transfers by evaluating the area between the SET current trace and the set point, as indicated in figure 3(a). The tunable parameters of the PID controller define the observed decay time.

In figure 3(b), we show histograms of the SET signal area at plunger voltages corresponding to the maximum probability of achieving $n = 0, 1, 2,$ or 3 electrons transferred per cycle. In order to evaluate the transfer probabilities P_n at different V_{PL}, we fit the histograms with a function $f(x) = \sum_n A_n g(x, b_n, \sigma_n)$, where $g(x, b_n, \sigma_n)$ is a Gaussian distribution with mean b_n and standard deviation σ_n. Since the mean and standard deviation of each distribution are essentially independent of the plunger gate voltage, we determine their values using the whole data set acquired for all different voltage ranges. For the mean values we obtain $b_n = n \times 1.15$ pC and for the standard deviations $\sigma_n = 0.37$ pC for $n \neq 2$ and $\sigma_2 = 0.33$ pC. The probabilities P_n for n transferred electrons are extracted using the amplitudes A_n as fitting parameters for each V_{PL} and computing $P_n = A_n / \sum_{j=0}^{4} A_j$. In figure 3(c), a representative fit at $V_{PL} = 0.62$ V is presented.

Figure 3(d) shows the probability of a single-electron transition as a function of the number of consecutively applied pumping pulses since the initialization of the reservoir. The error bars indicate 95% confidence interval obtained by taking into account two error sources independently: uncertainty related to the fit of the amplitude A_n and the one obtained from the Wilson score interval method. Each data point is derived from combined statistics of 2000 pulses and 200 reset events. The data show that we may inject up to 50 electrons into the

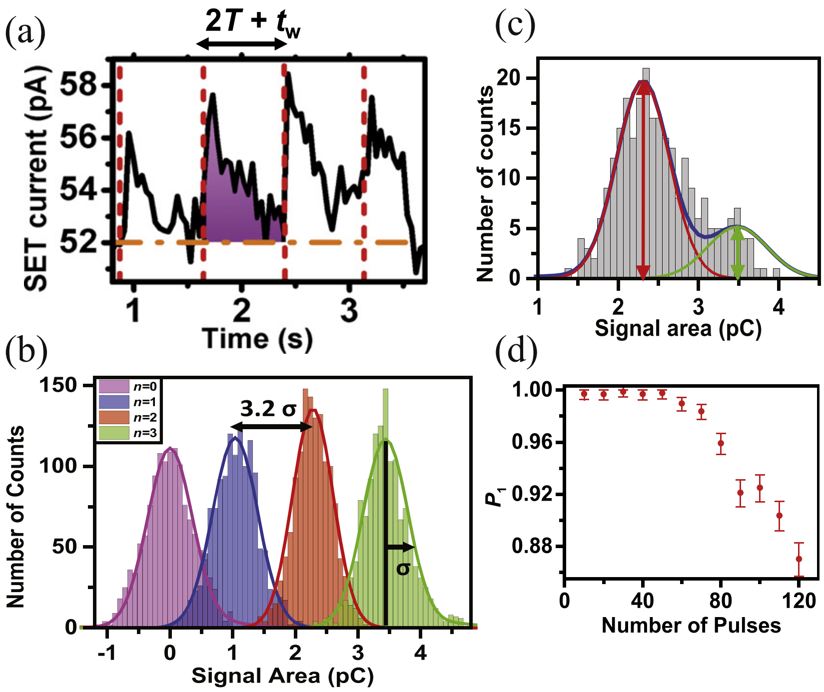

Figure 3. (a) Representative trace of the SET signal in the electron counting experiments. The red vertical dashed lines indicate the time instants of the pumping events. The orange horizontal dashed line is the set point of the PID controller. The number of electrons transferred during the pumping cycle is estimated from the shaded area enclosed between the set point and the SET signal. (b) Histograms of signal areas at V_{PL} values for which the transport is quantized at $n = 0, 1, 2,$ and 3 in the direct-current experiment. Gaussian fits are shown for each data set. (c) Histogram of SET signal areas at $V_{PL} = 0.62$ V with 264 pumping pulses in total. The amplitudes of fitted Gaussian distributions (red and green arrows) yield the probabilities, P_n, as described in the text. (d) Probability of a single electron transition as a function of the number of consecutive pumping pulses with error bars indicating 95% confidence interval. Each point is statistically evaluated as an aggregate of 2000 counts. Gate voltages are set to the values corresponding to one transferred electron per cycle in the direct-current scheme.

reservoir without changing the probability more than 1%. This probability decreases with increasing number of pumped electrons into the reservoir due to its increasing electrochemical potential [28]. We estimate the capacitance between DL and the reservoir by assuming them to be parallel plate capacitors: $C_{RES-DL} = \epsilon A/d \approx 1.8 \times 10^{-15}$ F, where ϵ is the permittivity of SiO_2, A is the area of the reservoir dot, and d is the thickness of the SiO_2. Thus the charging energy of the reservoir is roughly $E_C = e^2/C_{RES-DL} \approx 87\ \mu$eV leading to a potential difference of the reservoir due to 50 excess electrons in the island of $\Delta_{RES} \approx 4.3$ mV.

In order to extract the probabilities P_n for $n = 0, 1, 2, 3,$ and 4 as a function of plunger voltage, we apply a reset event followed by 22 consecutive pumping pulses. We repeat this procedure 12 times for each voltage value. Based on the data presented in figure 3(d) where $P_1 > 99\%$ for up to 50 consecutive pumping pulses, we note that the choice of 22 pulses between each reset should not lead to observable underpumping for $n = 1$ within the uncertainty of the counting scheme. The average number of electrons pumped per cycle can be computed from the individual probabilities as $n_{count} = \sum_n nP_n$. In figure 4(a) the probabilities P_n are shown as well as n_{count}. The error bars are computed the same way as in figure 3(d). The data indicate that, by adjusting the potential of the dot, it is possible to transfer with a single pulse up to three electrons with over 99% probability. However, single electron transfers are clearly more robust than multiple electron transfers since P_1 is insensitive to variations of V_{PL} in a significantly larger range than that of P_2 and P_3.

Figure 4(a) also shows the average number of electrons transferred per cycle measured with the direct-current scheme $n_{dc} = I/ef$. Interestingly, these data are in good agreement with the counting method. Note that the curves for P_n are shifted by -7.00 mV in V_{PL} justified by the capacitive coupling between the SB gate and the pump dot and the fact that we need to use a different gate voltage in the direct-current scheme ($V_{SB} = 0.39$ V) compared with the electron counting scheme ($V_{SB} = 0.20$ V). We verified that the magnitude of the applied shift is in agreement with the observed shift of the current plateaux in the direct-current scheme (see figure 4(b)). The electron channel under the switch barrier turns off completely around $V_{SB} = 0.30$ V which prevented us from measuring the shift in this scheme at lower voltages. We neglect the shift of the plateaux due to different V_{TG} used in the two schemes since it is much smaller than the shift due to V_{SB}.

In the electron counting scheme, the rising edge to the first plateau shifts in V_{PL} as a function of number of excess electrons in the reservoir. Since we average over 22 pumped electrons this shift broadens the rise to the first plateau in figure 4(a). This effect is not clearly visible for the other, notably broad, steps.

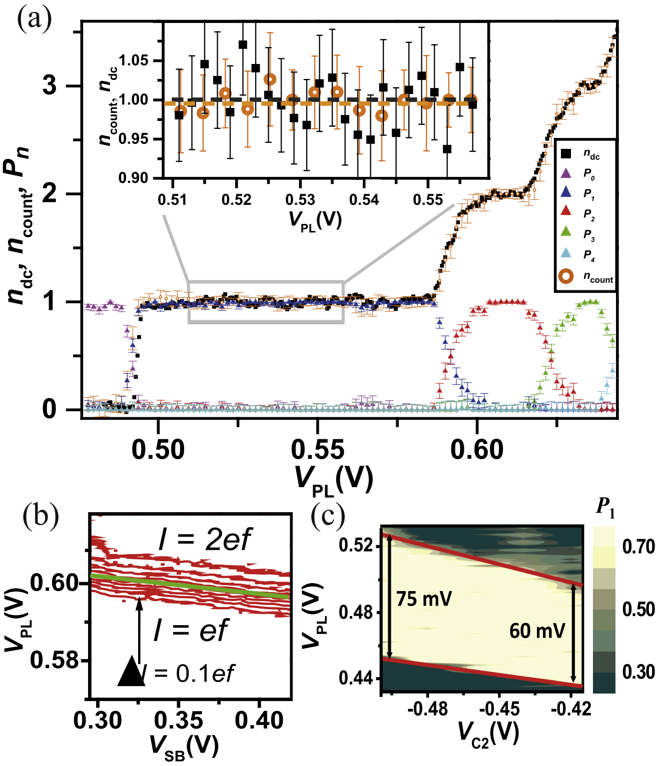

Figure 4. (a) Average number of electrons pumped per cycle $n_{\mathrm{dc}} = I/ef$ measured in the direct-current scheme with $ef \approx 80$ fA, and probabilities P_n of number of electrons pumped per cycle determined from the electron counting scheme as well as $n_{\mathrm{count}} = \sum_n nP_n$ as functions of V_{PL}. The error bars indicate 95% confidence interval. The gate voltages in the two experiments are the following: $V_{\mathrm{BL}} = 0.63$ V, $V_{\mathrm{BR}} = 0.48$ V, $V_{\mathrm{C2}} = -1.0$ V, $V_{\mathrm{C1}} = -0.25$ V, $V_{\mathrm{SL}} = 2.4$ V, $V_{\mathrm{DL}} = 1.9$ V, $V_{\mathrm{B1}} = 0.85$ V, and $V_{\mathrm{B2}} = 0.69$ V. In the direct-current scheme we employ $V_{\mathrm{SB}} = 0.20$ V and $V_{\mathrm{TG}} = 0.98$ V, and in the counting scheme $V_{\mathrm{SB}} = 0.39$ V and $V_{\mathrm{TG}} = 0.95$ V. The probability traces have been shifted by $\Delta V_{\mathrm{PL}} = -7.0$ mV to account for different values of V_{SB} in the two experiments. The peak amplitudes of the rf drives are $A_{\mathrm{PL}} = A_{\mathrm{BL}} = 0.15$ V in both cases. Inset: every second data point of n_{count} and every fourth data point of n_{dc} from the main panel in the voltage region highlighted by the grey rectangle. The error bars indicate 95% confidence interval. The dashed black and orange lines represent the mean of 100 data points for $\bar{n}_{\mathrm{dc}}$ and of 30 data points for $\bar{n}_{\mathrm{count}}$, respectively, measured within the shown V_{PL} range. (b) Pumped direct current as a function of V_{PL} and the switch barrier voltage. The other parameter values are identical to those in panel (a). The spacing in current between the red contours is 0.1*ef*. The green line is a guide for the eye to indicate the applied linear compensation in V_{PL} due to the different values of V_{SB}. (c) P_1 as a function of V_{PL} and the confining gate voltage V_{C2}. The other parameter values are as in (a) except for $V_{\mathrm{BL}} = 0.60$ V and $V_{\mathrm{TG}} = 1.2$ V.

In the inset of figure 4(a), the quantized electron pumping at the $n = 1$ plateau is compared in detail between the two measurement schemes. The positive and negative errorbars of n_{dc} each indicate two standard deviations of the shown data at the $n = 1$ plateau. The two data sets well agree within the experimental uncertainty. Averaging this data yields our best estimates for the average number of pumped electrons at the first plateau $n_{\mathrm{dc}} = 1.000 \pm 0.006$ and $n_{\mathrm{count}} = 0.998 \pm 0.004$ where we employ the 95% uncertainty level.

Finally, the probability P_1 as a function of V_{C2} and V_{PL} is presented in figure 4(c). We observe that the robustness of the single-electron transfer with respect to V_{PL} increases with decreasing V_{C2}. This phenomenon is due to an increase in the charging energy caused by a tightening of the electrostatic confinement of the pump dot. Here, we show this effect in the electron counting scheme as a consistency check of similar behaviour previously observed in the direct-current scheme [14, 38].

4. Discussion

In this work, we compare the direct current generated with a quantum dot pump with electron counting scheme at a relative uncertainty below a per cent. The main limiting factor of our experimental approach is the relatively low sensitivity of the charge detector. Typically, in order to confidently assess single-electron counting statistics, one has to trade between the size of the storage reservoir and the sensitivity of the sensor. Our device is designed to have a fairly large reservoir to minimize the back-action on the pumping mechanism.

The disadvantage of this choice is the reduced performance of the readout. We estimate that the sensitivity of our detector is about 90 m$e/\sqrt{\mathrm{Hz}}$. This indicates that it is possible to sense a single electron in about 8 ms of averaging time. However, we have chosen to integrate up to 750 ms between pumping pulses to reduce the uncertainty in the readout. In this context, the employed PID controller reduces the slow drifts in the SET current. Nevertheless, the limited reservoir-to-sensor capacitive coupling of about $0.005e$ is mainly responsible for the non-ideal readout fidelity. The observed distributions of the signals for different numbers of pumped electrons are separated only by 3.2σ. Hence, those counting events that fall further than 1.6σ from the centre of the distribution should be considered as misattributions in the most conservative scenario.

In the near future, we will integrate a metallic SET sensor next to the silicon reservoir. In this way, we estimate that the capacitive coupling and, hence, the sensitivity will be improved up to an order of magnitude. This will allow us to enhance the readout fidelity and reduce the counting uncertainty down to ppm levels, while keeping the back action on the pump insignificantly small.

Ultimately, a precise electron pump verified by error counting would, not only provide a supreme candidate for the realization of the quantum ampere [1], but could also be harnessed in the quantum metrological triangle experiment [39, 40] to test the fundamental constants of nature.

Acknowledgments

We thank F Hudson, C H Yang, Y Sun, G C Tettamanzi, I Iisakka, A Manninen, and A Kemppinen for useful discussions. We acknowledge financial support from the Australian Research Council (Grant No. DP120104710), the Academy of Finland (Grant No. 251748, 135794, 272806, 276528), Jenny and Antti Wihuri Foundation, The Finnish Cultural Foundation, and the Australian National Fabrication Facility. We acknowledge the provision of facilities and technical support by Aalto University at Micronova Nanofabrication Centre. AR acknowledges support from the University of New South Wales Early Career Research Grant scheme.

References

[1] Pekola J, Saira O P, Maisi V, Kemppinen A, Möttönen M, Pashkin Y and Averin D 2013 *Rev. Mod. Phys.* **86** 1421
[2] Pothier H, Lafarge P, Urbina C, Esteve D and Devoret M H 1992 *Europhys. Lett.* **17** 249
[3] Keller M W, Martinis J M, Zimmerman N M and Steinbach A H 1996 *Appl. Phys. Lett.* **69** 1804
[4] Keller M W, Eichenberger A L, Martinis J M and Zimmerman N M 1999 *Science* **285** 1706
[5] Geerligs L J, Verbrugh S M, Hadley P, Mooij J E, Pothier H, Lafarge P, Urbina C, Esteve D and Devoret M H 1991 *Z. Phys.* B **85** 349
[6] Vartiainen J J, Möttönen M, Pekola J P and Kemppinen A 2007 *Appl. Phys. Lett.* **90** 082102
[7] Möttönen M, Vartiainen J J and Pekola J P 2008 *Phys. Rev. Lett.* **100** 177201
[8] Pekola J P, Vartiainen J J, Möttönen M, Saira O P, Meschke M and Averin D V 2008 *Nat. Phys.* **4** 120
[9] Maisi V F, Saira O P, Pashkin Y A, Tsai J S, Averin D V and Pekola J P 2011 *Phys. Rev. Lett.* **106** 217003
[10] Kouwenhoven L P, Johnson A T, van der Vaart N C, Harmans C J P M and Foxon C T 1991 *Phys. Rev. Lett.* **67** 1626
[11] Blumenthal M D, Kaestner B, Li L, Giblin S, Janssen T J B M, Pepper M, Anderson D, Jones G and Ritchie D A 2007 *Nat. Phys.* **3** 343
[12] Chan K W, Möttönen M, Kemppinen A, Lai N S, Tan K Y, Lim W H and Dzurak A S 2011 *Appl. Phys. Lett.* **98** 212103
[13] Jehl X *et al* 2013 *Phys. Rev.* X **3** 021012
[14] Rossi A, Tanttu T, Tan K Y, Iisakka I, Zhao R, Chan K W, Tettamanzi G C, Rogge S, Dzurak A S and Möttönen M 2014 *Nano Lett.* **14** 3405
[15] Connolly M R *et al* 2013 *Nat. Nanotechnology* **8** 417
[16] Lansbergen G P, Ono Y and Fujiwara A 2012 *Nano Lett.* **12** 763
[17] Roche B, Riwar R P, Voisin B, Dupont-Ferrier E, Wacquez R, Vinet M, Sanquer M, Splettstoesser J and Jehl X 2013 *Nat. Commun.* **4** 1581
[18] Yamahata G, Nishiguchi K and Fujiwara A 2014 *Nat. Commun.* **5** 5038
[19] Tettamanzi G C, Wacquez R and Rogge S 2014 *New J. Phys.* **16** 063036
[20] Feltin N and Piquemal F 2009 *Eur. Phys. J. Spec. Top.* **172** 267
[21] Giblin S P, Kataoka M, Fletcher J D, See P, Janssen T J B M, Griffiths J P, Jones G A C, Farrer I and Ritchie D A 2012 *Nat. Commun.* **3** 930
[22] Stein F *et al* 2015 *Appl. Phys. Lett.* **107** 103501
[23] Fujiwara A and Takahashi Y 2001 *Nature* **410** 560
[24] Fujiwara A, Zimmerman N M, Ono Y and Takahashi Y 2004 *Appl. Phys. Lett.* **84** 1323
[25] Fujiwara A, Nishiguchi K and Ono Y 2008 *Appl. Phys. Lett.* **92** 042102
[26] Koppinen P J, Stewart M D J and Zimmerman N M 2013 *IEEE Trans. Electron Devices* **60** 78
[27] Keller M W, Martinis J M and Kautz R L 1998 *Phys. Rev. Lett.* **80** 4530–3
[28] Jehl X, Keller M W, Kautz R L, Aumentado J and Martinis J M 2003 *Phys. Rev.* B **67** 165331
[29] Kautz R L, Keller M W and Martinis J M 2000 *Phys. Rev.* B **62** 15888
[30] Kautz R L, Keller M W and Martinis J M 1999 *Phys. Rev.* B **60** 8199
[31] Nishiguchi K, Fujiwara A, Ono Y, Inokawa H and Takahashi Y 2006 *Appl. Phys. Lett.* **88** 183101
[32] Yamahata G, Nishiguchi K and Fujiwara A 2011 *Appl. Phys. Lett.* **98** 222104
[33] Fricke L *et al* 2013 *Phys. Rev. Lett.* **110** 126803
[34] Fricke L *et al* 2014 *Phys. Rev. Lett.* **112** 226803
[35] Yamahata G, Nishiguchi K and Fujiwara A 2014 *Phys. Rev.* B **89** 165302
[36] Bylander J, Duty T and Delsing P 2005 *Nature* **434** 361
[37] Rossi A, Tanttu T, Hudson F E, Sun Y, Möttönen M and Dzurak A S 2015 *J. Vis. Exp.* **100** e52852
[38] Seo M, Ahn Y H, Oh Y, Chung Y, Ryu S, Sim H S, Lee I H, Bae M H and Kim N 2014 *Phys. Rev.* B **90** 085307
[39] Likharev K K and Zorin A B 1985 *J. Low Temp. Phys.* **59** 347
[40] Milton M J T, Williams J M and Forbes A B 2010 *Metrologia* **47** 279